Manipulating frequency-entangled photons

Laurent Olislager

Université libre de Bruxelles
École polytechnique de Bruxelles
Service OPÉRA

Université de Franche-Comté
Institut FEMTO-ST
Laboratoire d'Optique

Thèse de Doctorat présentée par

Laurent OLISLAGER

pour obtenir le

Grade de Docteur de l'Université de Franche-Comté

Spécialité : optique et photonique

Manipulating frequency-entangled photons

Manipulation de photons intriqués en fréquence

Soutenue le 19 décembre 2014 devant le jury composé de :

- *Matthieu Bloch, Pr., Georgia Tech Lorraine, Metz, France (Rapporteur)*
- *Edouard Brainis, Pr., Universiteit Gent, Ghent, Belgium (Membre)*
- *Nicolas Cerf, Pr., Université libre de Bruxelles, Brussels, Belgium (Président)*
- *Philippe Emplit, Pr., Université libre de Bruxelles, Brussels, Belgium (Membre)*
- *Serge Massar, Pr., Université libre de Bruxelles, Brussels, Belgium (Membre)*
- *Jean-Marc Merolla, Pr., Université de Franche-Comté, Besançon, France (Membre)*
- *Kien Phan Huy, Pr., Université de Franche-Comté, Besançon, France (Membre)*
- *Robert Thew, Dr., Université de Genève, Geneva, Switzerland (Rapporteur)*

À Simone et Michèle

Acknowledgements

I would like to express (in French) my gratitude to all the people who have made the six years of my PhD thesis both passionating and fun. Let's go for all the "merci".

Serge, un immense merci pour m'avoir guidé tout au long de ces années, avec un équilibre parfait entre encadrement et liberté. Merci pour tes conseils avisés, ton éclectisme, ton enthousiasme. Merci pour les agréables moments en ta compagnie. Je ne comprends toujours pas comment tu peux annoncer 90% du temps "poker" tout en en faisant une stratégie gagnante.

Philippe, un tout grand merci de m'avoir "ouvert les portes du laboratoire" et pour la confiance que tu m'as témoignée. Merci de faire régner la bonne ambiance au sein d'OPÉRA et pour ta gestion des dossiers kilométriques que ma thèse en co-tutelle a notamment imposés.

Jean-Marc, merci pour ton expertise dans la manipulation de photons en fréquence. Tes connaissances au laboratoire, tes ressources et ta disponibilité ont grandement facilité les débuts de ma thèse. Rien n'aurait été possible sans toi.

Kien, merci pour ton incroyable taux de génération de nouvelles idées (en particulier celle qui a initié ma thèse) et pour ton aide au jour le jour. Grâce à toi, je sais (presque correctement) faire des soudures électriques.

Jean-Marc et Kien, je me souviendrai longtemps de notre première semaine de manipulations à Bruxelles. Merci aussi Johann pour cette chouette expérience d'insomnies scientifiques.

Les mois passés à Besançon furent passionnants scientifiquement et agréables humainement. Qui a dit qu'il ne faisait jamais beau dans cette ville? Ismaël, merci pour tout le temps partagé autour d'une table d'optique, et pour les plats sénégalais. Merci aux personnes qui m'ont accueilli au laboratoire, en particulier Hervé, Valérie, Birgit, Thibaut, Batiste.

Revenons en Belgique. Merci Erik pour l'excellent travail réalisé lors de ton mémoire et de la préparation des articles, tu as grandement contribué à cette thèse. Merci aux étudiants que j'ai eu la chance d'encadrer, Bruno, Sébastien et Igor dans le contexte de ces travaux, ainsi que Romain, Olivier et Jorge. Merci aussi à Anthony et Nam. Merci aux scientifiques plus expérimentés avec qui j'ai eu la chance de collaborer, en particulier Stefano, Manas et Branko.

À OPÉRA, merci Anh Tuan d'avoir inauguré les travaux menant à cette thèse. Stéphane, un immense merci d'avoir partagé ton bureau et ta table de manipulation avec le petit nouveau que j'étais, et pour m'avoir patiemment expliqué comment ne pas brûler des connecteurs optiques. Eddy, ce fut très enrichissant de te côtoyer, toi le maître des explications physiques et questions judicieuses; tes "c'est pas mal" résonnent en moi avec la valeur d'un "formidable". Jassem, merci beaucoup pour ta dextérité au laboratoire et ta bonne humeur au bureau (sauf quand Cricri perdait). François D., merci d'avoir installé 10^{23} fois Matlab, et de savoir reconnaître n'importe quel connecteur RF à un mètre de distance. François L., merci de m'avoir enseigné la science du PID, et bien entendu pour les soirées débat, "fieu". Merci aussi à Adrien pour ces débats, et pour notre séjour bisontin. Merci Pascal et Simpi pour vos explications à tout sujet.

Merci aux autres membres passés et présents d'OPÉRA pour la formidable ambiance de travail (ou parfois ambiance tout court). Merci François B. l'as de la fléchette (et pas seulement). Merci Thomas pour ta culture générale, parfois très spécifique. Merci Anh Dung pour ton inlassable organisation de chouettes activités. Quarante-deux fois "grazie" Serena, au moins par écrit on ne perçoit pas la mauvaise position de l'accent tonique. Merci Akram de vivre à fond chaque match de PlayStation. Merci Antoine de ne pas insister sur le fait que je chante tout haut dans le bureau. Merci Maïté pour nos montagnes russes. Merci Lory, Mika, Olivier, Yvan, Han, Anteo, Quentin, Piotr, Ali, Evdokia... Ibtissame et Alexandra, merci à vous pour le travail immense que vous accomplissez avec efficacité et sourire.

Merci aux personnes impliquées avec moi dans des activités d'enseignement, à commencer bien entendu par Marc, mais aussi, parmi ceux que je ne n'ai pas encore cités, Yves, Pierre, Stéphane, Jonathan, Bertrand... Merci aussi chers étudiants, en particulier les "grands" de la Saphybru, vous m'avez beaucoup apporté. De l'autre côté, merci à tous les professeurs ayant éveillé mon goût pour les sciences. En particulier, merci à Nicolas Cerf d'avoir encadré mon mémoire de fin d'études qui reste un excellent souvenir. Au QuIC, merci aussi à Evgueni pour sa gentillesse et Anaëlle pour être devenue plus qu'une lointaine collègue.

Merci aux membres du jury d'avoir accepté d'examiner cette thèse. Merci à celles et ceux croisés au hasard d'un laboratoire ou d'une conférence, et qui m'ont inspiré. Merci à toutes les institutions ayant financé mes travaux et voyages, et aux personnes qui permettent à des gens comme moi de s'amuser à faire de la recherche.

Enfin, je voudrais remercier les personnes extérieures qui ont néanmoins certainement eu un impact sur cette thèse: mes coéquipiers basketteurs, les anciens de l'école, en particulier Charlotte et sa famille, les anciens de l'université, en particulier Simon, Cédric, François, et Amélie, Marie, Céline, ainsi que Florie, Laura, Nathalie. Merci à tous mes oncles et tantes, cousins et cousines. Merci aux marraines Simone et Michèle, vous êtes une source d'inspiration chaque jour. Merci Benoît et Sarah, et la merveilleuse Manon et celles ou ceux qui restent à venir. À mes parents Ingrid et Roland, que puis-je dire? Ils m'ont soutenu de la première et à la dernière seconde, littéralement. Puis-je, en bon spécialiste de l'optique, absorber l'amour qu'ils me portent à sa juste valeur, pour mieux le transmettre et le réfléchir.

Publications

The present thesis is based on the following publications.

Publications in international peer-reviewed journals:

– L. Olislager, J. Cussey, A. T. Nguyen, P. Emplit, S. Massar, J.-M. Merolla, & K. Phan Huy, *Frequency-bin entangled photons*, Physical Review A **82**, 013804 (2010).
– L. Olislager, I. Mbodji, E. Woodhead, J. Cussey, L. Furfaro, P. Emplit, S. Massar, K. Phan Huy, & J.-M. Merolla, *Implementing two-photon interference in the frequency domain with electro-optic phase modulators*, New Journal of Physics **14**, 043015 (2012).
– L. Olislager, J. Safioui, S. Clemmen, K. Phan Huy, W. Bogaerts, R. Baets, P. Emplit, & S. Massar, *Silicon-on-insulator integrated source of polarization-entangled photons*, Optics Letters **38**, 1960 (2013).
– M. K. Patra, L. Olislager, F. Duport, J. Safioui, S. Pironio, & S. Massar, *Experimental refutation of a class of ψ-epistemic models*, Physical Review A **88**, 032112 (2013).
– L. Olislager, E. Woodhead, K. Phan Huy, J.-M. Merolla, P. Emplit, & S. Massar, *Creating and manipulating entangled optical qubits in the frequency domain*, Physical Review A **89**, 052323 (2014).

Presentations in international conferences with proceedings:

– L. Olislager, J. Cussey, A. T. Nguyen, P. Emplit, S. Massar, J.-M. Merolla, & K. Phan Huy, *Manipulating frequency entanglement with phase modulators*, Th16, International Conference on Quantum Information Processing and Communication (QIPC 2009). Poster presented by L. Olislager, Roma, Italy, September 2009.
– L. Olislager, J. Cussey, A. T. Nguyen, P. Emplit, S. Massar, J.-M. Merolla, & K. Phan Huy, *Manipulating frequency entangled photons*, p. 58–65, Quantum Communication and Quantum Networking (QuantumComm 2009), Springer Berlin Heidelberg, 2010. Talk presented by L. Olislager, Vico Equense, Italy, October 2009.
– L. Olislager, J. Cussey, A. T. Nguyen, P. Emplit, S. Massar, J.-M. Merolla, & K. Phan Huy, *Manipulating frequency entangled photons*, 14th Annual Symposium of the IEEE Photonics Benelux Chapter. Talk presented by L. Olislager, Brussels, Belgium, November 2009.
– L. Olislager, I. Mbodji, J. Cussey, A. T. Nguyen, P. Emplit, K. Phan Huy, J.-M. Merolla, & S. Massar, *Enchevêtrement de paires de photons dans le domaine fréquentiel*, Journées Nationales d'Optique Guidée (JNOG 2010). Talk presented by S. Massar, Besançon, France, October 2010.
– L. Olislager, I. Mbodji, E. Woodhead, J. Cussey, A. T. Nguyen, P. Emplit, S. Massar, J.-M. Merolla, & K. Phan Huy, *Two-photon interference using frequency-bin entanglement*, 15th Annual Symposium of the IEEE Photonics Benelux Chapter. Talk presented by L. Olislager, Delft, The Netherlands, November 2010.
– J.-M. Merolla, I. Mbodji, L. Olislager, E. Woodhead, K. Phan Huy, L. Furfaro, & S. Massar, *Bell inequality violation in frequency domain using 25 GHz frequency sideband modulation architecture*, ED.P.3, European Quantum Electronics Conference, Optical Society of America, 2011. Poster presented by K. Phan Huy, Munich, Deutschland, May 2011.

– J.-M. Merolla, L. Fufaro, K. Phan Huy, I. Mbodji, S. Massar, E. Woodhead, L. Olislager, & R. Giust, *Reliable and efficient control of spectral qubits using optoelectronic devices: progress and perspectives*, 8272-26, SPIE Photonics West. Talk presented by J.-M. Merolla, San Francisco, United States of America, January 2012.
– I. Mbodji, L. Olislager, E. Woodhead, B. Galmes, J. Cussey, L. Furfaro, P. Emplit, S. Massar, K. Phan Huy, & J.-M. Merolla, *Two-photon experiments in the frequency domain*, 84400J, SPIE Photonics Europe, International Society for Optics and Photonics, 2012. Talk presented by L. Olislager, Brussels, Belgium, April 2012.
– L. Olislager, F. Duport, J. Safioui, M. K. Patra, S. Pironio, & S. Massar, *Experimental refutation of a class of quantum epistemic models*, paper 043, 18th Annual Symposium of the IEEE Photonics Benelux Chapter. Talk presented by L. Olislager, Eindhoven, The Netherlands, November 2013.
– L. Olislager, E. Woodhead, K. Phan Huy, J.-M. Merolla, P. Emplit, & S. Massar, *Manipulating optical qubits in the frequency domain*, paper 044, 18th Annual Symposium of the IEEE Photonics Benelux Chapter. Poster presented by L. Olislager, Eindhoven, The Netherlands, November 2013.
– L. Olislager, E. Woodhead, K. Phan Huy, J.-M. Merolla, P. Emplit, & S. Massar, *Creation and manipulation of two-dimensional photonic frequency entanglement*, FTh1A-1, CLEO: QELS Fundamental Science, Optical Society of America, 2014. Talk presented by L. Olislager, San Jose, United States of America, June 2014.
– L. Olislager, B. Kolaric, W. Kubo, T. Tanaka, R. A. L. Vallée, P. Emplit, & S. Massar, *Plasmon-assisted transmission of frequency-bin entangled photons*, C-35, 21st Central European Workshop on Quantum Optics (CEWQO 2014). Talk presented by L. Olislager, Brussels, Belgium, June 2014.

Other publications:

– L. Olislager, *Des photons jumeaux pour des communications quantiques en couleurs*, prix A'Doc de la jeune recherche en Franche-Comté, Presses Universitaires de Franche-Comté, 2014.
– L. Olislager, *Introduction à l'information quantique*, notes de cours d'initiation à la physique quantique, Université Inter-Âges de l'Université libre de Bruxelles, 2014.

Jury

The doctoral jury evaluating the validity of this PhD thesis is composed of:

– Matthieu Bloch, Pr., Georgia Tech Lorraine, Metz, France (referee)
– Edouard Brainis, Pr., Universiteit Gent, Ghent, Belgium
– Nicolas Cerf, Pr., Université libre de Bruxelles, Brussels, Belgium (president)
– Philippe Emplit, Pr., Université libre de Bruxelles, Brussels, Belgium (adviser)
– Serge Massar, Pr., Université libre de Bruxelles, Brussels, Belgium (co-adviser)
– Jean-Marc Merolla, Pr., Université de Franche-Comté, Besançon, France (adviser)
– Kien Phan Huy, Pr., Université de Franche-Comté, Besançon, France (co-adviser, secretary)
– Robert Thew, Dr., Université de Genève, Geneva, Switzerland (referee)

Contents

List of Figures

List of Tables

Introduction

In the twentieth century, the founding fathers of quantum mechanics explored the implications of their theory by designing *gedanken* experiments. In recent years, continuous improvement of the experimental manipulation of individual quantum systems has opened the way to exciting research, both on blackboards and in laboratories, and even towards field experiments.

From the fundamental point of view, this progress allows to test the intrinsic quantum nature of microscopic systems, and how this connects to other scientific fields, such as metrology [GLM06]. Many of the *gedanken* experiments have now been performed experimentally. This includes tests of wave-particle duality, wave-function collapse, quantum nonlocality, etc. [Zei99, BLS+13, Gis14]

In a more applied direction, the manipulation of individual quantum systems is the basis for *quantum information* processing: when an information content is associated with transformations and measurements of quantum systems, it offers a new paradigm, full of potentialities, to information theory. This leads to quantum random number generation, quantum computing, quantum communication, including quantum teleportation and quantum cryptography, etc. [NC10]

One of the promises of quantum information is the realization of a *quantum internet* [Kim08]: quantum communication links would allow to share quantum states between the nodes — quantum computers— of the network [GT07]. Quantum cryptography and quantum teleportation would open the way to absolutely secure transmission of secret messages and faithful transfer of unknown quantum states. To exploit the potentialities of such a network, one needs to be able to produce *quantum entanglement* [HHHH09], distribute it across the network, manipulate and detect it in an efficient way. In this case, several theoretical and experimental developments strengthen the confidence of the scientific community in a future full-scale realization; this includes quantum error correction [BDSW96], repeater architecture [BDCZ98], purification techniques [PSBZ01], and the ability to transfer the quantum state from a system to another [CZKM97, MK04, TTH+05].

This last possibility allows to exploit "the best of both worlds": for example, matter systems for quantum computation, and light particles for quantum communication. Indeed, photons are the preferred flying quantum bit: because they interact weakly with the environment, and thus suffer from little decoherence and loss, their quantum state can in principle be transmitted with high fidelity and efficiency through kilometers of free space or optical fiber. These two media constitute competing approaches for the realization of a long-range quantum network, respectively via satellites or terrestrial nodes. Quantum optics [MW95] thus provides a powerful way to implement long-distance quantum communication protocols. One key element to this end is the ability to produce, transmit, manipulate and detect quantum states of light, in particular photonic quantum entanglement.

Our work lies in the context of experimental quantum optics in optical fibers at telecommunication wavelengths, in view of quantum communication applications. Techniques for producing

single photons and entangled photons become standard; sources of photon pairs are mainly based on spontaneous parametric down-conversion in nonlinear waveguides [KR97]. Optical fibers profit from the investments of the telecommunication industry [Agr97], offering losses as low as 0.2 dB/km. Single-photon detectors still suffer from lower efficiency and higher noise than their visible-wavelength counterparts, but avalanche photodiodes [RGZG98] and superconducting single-photon detectors [GOC$^+$01] both offer promising characteristics. In this work, we focus mainly on the way quantum states can be manipulated. In principle, quantum information can be encoded in various photonic degrees of freedom, such as polarization [ADR82, KMW$^+$95], position and momentum [RT90a], angular momentum [MVWZ01], and energy-time [Fra89]. Since there are competing architectures and physical implementations of quantum protocols, flexibility in the way quantum information is encoded is most welcome.

The photon polarization provides a natural two-dimensional system and is easily manipulated with phase plates, polarizers and polarizing beam splitters. It has thus been extensively used in quantum optics. However it is not very well suited for fiber-optic implementations: because of fiber polarization-dependent loss and birefringence implying polarization-mode dispersion, it requires complex compensation methods and limitations to avoid depolarization and thus decoherence. Single-mode telecommunication optical fibers also impose the spatial wave-function of the photon, ruling out the possibility to use momentum and angular momentum. On the other hand, the energy-time degree of freedom is particularly interesting for long-distance quantum communication at telecommunication wavelengths. Easily produced and detected, it is robust against decoherence, as it propagates essentially undisturbed through optical fibers over large distances.

The traditional approach to manipulate energy-time entangled photons is based on the notion of time bin: quantum information is encoded in the relative phase between distinct spatio-temporal paths, which interfere via Mach–Zehnder interferometers. Time-bin encoding has become a powerful platform to investigate quantum entanglement, yielding seminal works such as long-distance violation of Bell inequalities [TBZG98, MDRT$^+$04], entanglement-based quantum key distribution [RBG$^+$00], and quantum teleportation [DRMT$^+$04], a fundamental building block of quantum networks.

The aim of our work is to demonstrate an alternative approach to manipulate energy-time entangled photons in optical fibers at telecommunication wavelengths. We investigate and implement an original method for their manipulation by building on proven techniques for their production, transmission and detection —namely nonlinear waveguides, optical fibers and single-photon detectors, respectively. The photon pairs produced by a parametric down-conversion source are sent through independent electro-optic phase modulators, which act as high-dimensional frequency beam splitters, transforming the photonic states in the frequency domain. We then use frequency filters to discriminate the photons' frequencies. Such experimental methods, whose classical origin can be traced back to coherent communication, have been previously used with attenuated coherent states as approximations of single photons [MMG$^+$99b, MMGR99, MMG$^+$99a, DMG$^+$01, MSM$^+$02, GMS$^+$03, BMMP07, CPPM08].

In the present work, we aim to show that *frequency-bin entanglement* provides an interesting alternative platform for quantum communication. Our main experimental results towards this goal are the obtaining of high-visibility two-photon interference patterns allowing Bell inequality violations [OCN$^+$10, OMW$^+$12, OWPH$^+$14]. Our method provides decisive advantages: high dimensionality, use of standard optical and optoelectronic components, inherent stability and robustness, no need for active stabilization in laboratory conditions, visibilities comparable to the highest obtained using other degrees of freedom, etc. It has however a few drawbacks, mainly high losses and the somewhat complexity of the radio-frequency system which is not standard in quantum optics. Exploiting the high dimensionality is also challenging.

Our work is the result of a collaboration between teams from *Université libre de Bruxelles* (*OPÉRA-Photonique* and *Laboratoire d'Information Quantique*) and *Université de Franche-Comté* (*Laboratoire d'Optique* of *Institut FEMTO-ST*).

This dissertation is organized as follows. The first chapter introduces the basics of quantum entanglement and quantum communication, briefly describing the useful tools and concepts. The second chapter develops the theory behind the notion of frequency-bin entanglement, and details its experimental implementation. The third chapter lists uses of the method, including Bell inequality violation, exploration of quantum plasmonics, quantum key distribution, and other potential applications. Finally, we present research in experimental quantum optics at telecommunication wavelengths not directly related to frequency-bin entanglement. Chapter 4 describes an integrated source of polarization-entangled photons, while chapter 5 describes an experimental investigation on the nature of the quantum state.

Chapter 1

Quantum preliminaries

The birth of quantum information is based on the fact that "information is physical", i.e. that "it is always tied to a physical representation": "this ties the handling of information to all the possibilities and restrictions of our real physical world", as highlighted by Rolf LANDAUER [Lan96]. Since a physical system is necessary to carry information, the latter is indeed subjected to the physical laws that govern the former. For microscopic systems, quantum rules apply.

1.1 Quantum rules

We start by enunciating the postulates of quantum mechanics, developed in the first part of the twentieth century. Interpretation of these axioms, dominated by the Copenhagen interpretation of quantum physics established in the years 1925–1927, is still an active research topic.

Postulate 1 At a given time t, the quantum state of a system is defined by a normalized state $|\psi(t)\rangle$ belonging to the state space $\mathcal{E}$.

Postulate 2 Every measurable physical quantity $\mathcal{A}$ is described by an operator A acting in $\mathcal{E}$; this operator is an observable.

Postulate 3 The result of a measurement of physical quantity $\mathcal{A}$ is necessarily an eigenstate of the corresponding observable.

Postulate 4 When the physical quantity $\mathcal{A}$ is measured on a system in state $|\psi\rangle$, the probability $P(a_n)$ to obtain as a result the non-degenerate eigenvalue a_n is given by $P(a_n) = \left|\langle u_n|\psi\rangle\right|^2 = \langle\psi|P_n|\psi\rangle$, where $|u_n\rangle$ is the corresponding eigenstate and $P_n = |u_n\rangle\langle u_n|$ is a projector. This can be generalized to degenerate eigenvalues and to continuous spectra.

Postulate 5 Immediately after a measurement of the physical quantity $\mathcal{A}$ on a system in state $|\psi\rangle$, the system is projected into the eigenstate corresponding to the measured eigenvalue (wave-function collapse).

Postulate 6 The time evolution of $|\psi(t)\rangle$ is governed by the Schrödinger equation $i\hbar\frac{\mathrm{d}}{\mathrm{d}t}|\psi(t)\rangle = H(t)|\psi(t)\rangle$, where $H(t)$ is the observable associated with the total energy of the system, i.e. its Hamiltonian.

Quantum information theory and applications are based on these postulates and their consequences.

Because of the linearity of quantum mechanics, if $|\psi_0\rangle$ and $|\psi_1\rangle$ are state vectors, then the linear combination $|\psi\rangle = c_0|\psi_0\rangle + c_1|\psi_1\rangle$, with $c_0, c_1 \in \mathbb{C}$, $|c_0|^2 + |c_1|^2 = 1$, is also a state vector: this is the *superposition principle*.

In quantum information, we usually work in discrete Hilbert spaces of finite dimension. For example, in dimension 2, we choose a *computational basis* $\{|0\rangle, |1\rangle\}$, with $\langle i|j\rangle = \delta_{ij}$, $i, j \in \{0, 1\}$. A state vector $|\psi\rangle = c_0|0\rangle + c_1|1\rangle$ is said to be a quantum bit, or *qubit*. Because an absolute phase has no physical meaning, it can always be put in the form $|\psi\rangle = \cos(\theta/2)|0\rangle + \mathrm{e}^{\mathrm{i}\varphi}\sin(\theta/2)|1\rangle$, $\theta, \varphi \in \mathbb{R}$, corresponding to its representation on the *Bloch sphere* with spherical coordinates $0 \leq \theta \leq \pi$, $0 \leq \varphi \leq 2\pi$. When a measurement is done in the computational basis, the probability to obtain the result "0" —respectively "1"— is $P_0 = |c_0|^2$ —respectively $P_1 = |c_1|^2$. We can associate to each result an information content, such as in quantum random number generation, in this context the most straightforward application of quantum theoretical concepts, in particular the probabilistic nature of quantum measurements.

Another consequence of the linearity of quantum mechanics is the *no-cloning theorem* [WZ82, Die82]. This no-go theorem states the impossibility to create identical copies of an arbitrary unknown quantum state: there exists no transformation U such that $U\big(|\varnothing\rangle \otimes |\psi\rangle\big) = |\psi\rangle \otimes |\psi\rangle$, for all $|\psi\rangle$, where $|\varnothing\rangle$ is some initial state, and $\otimes$ represents the tensor product —an explicit notation we will omit in this document, see appendix A. Suppose indeed that such a transformation can clone states $|0\rangle$ and $|1\rangle$, i.e. that we have $U\big(|\varnothing\rangle|0\rangle\big) = |0\rangle|0\rangle$ and $U\big(|\varnothing\rangle|1\rangle\big) = |1\rangle|1\rangle$. Then, by linearity, $U\big(|\varnothing\rangle\big[c_0|0\rangle + c_1|1\rangle\big]\big) = c_0|0\rangle|0\rangle + c_1|1\rangle|1\rangle \neq \big[c_0|0\rangle + c_1|1\rangle\big]\big[c_0|0\rangle + c_1|1\rangle\big]$ for arbitrary c_0 and c_1 with $|c_0|^2 + |c_1|^2 = 1$. Note that though we used pure states and unitary evolution, the demonstration is general. Thus, due to the existence of non-orthogonal states, there is a fundamental impossibility to clone arbitrary unknown quantum states. This has important consequences in quantum information; for example, this limitation is necessary in the field of quantum cryptography.

Quantum information is also constraint by the Heisenberg uncertainty relation, which states that $\Delta A\,\Delta B \geq \frac{1}{2}\big|\big\langle\big[A, B\big]\big\rangle\big|$, where $\big[A, B\big] = AB - BA$ is the commutator of observables A and B (operators $\hat{O}$ are noted O, see appendix A), $\Delta O = (\langle O^2\rangle - \langle O\rangle^2)^{1/2}$, with mean value $\big\langle O\big\rangle = \mathrm{Tr}\big(\rho O\big)$, Tr the trace operation and ρ the density matrix of the state. We distinguish between *pure states*, for which $\rho = |\psi\rangle\langle\psi|$, and *mixed states*, for which $\rho = \sum_n p_n|\psi_n\rangle\langle\psi_n|$, the system being in state $|\psi_n\rangle$ with probability p_n. No state can simultaneously be eigenstate of two non-commutable observables; there exist non-compatible properties, which cannot have a definite value simultaneously. Such a fundamental *quantum indeterminacy* —a term preferred to the historic term quantum uncertainty— has important consequences in the fields of quantum information and foundations of quantum physics.

1.2 Quantum entanglement

Quantum entanglement has been the subject of countless important theoretical and experimental studies, and this concept lies more than ever at the heart of ongoing research in quantum information and foundations of quantum physics. It is perhaps the most fascinating aspect of

quantum mechanics, and it is used both for fundamental tests of physical principles and for applications such as quantum cryptography.

A *multi-partite state* is said to be entangled if it cannot be decomposed in a tensor product of single-partite states, i.e. if it is *non-separable*. Here we consider the simplest, two-dimensional and bi-partite, case, for which the arbitrary state

$$|\Psi_{AB}\rangle = c_{00}|0\rangle|0\rangle + c_{01}|0\rangle|1\rangle + c_{10}|1\rangle|0\rangle + c_{11}|1\rangle|1\rangle\,, \tag{1.1}$$

with $|c_{00}|^2 + |c_{01}|^2 + |c_{10}|^2 + |c_{11}|^2 = 1$, cannot in general be written as

$$|\Psi_{AB}\rangle = |\psi_A\rangle|\phi_B\rangle\,, \tag{1.2}$$

where A and B refer to two spatially separated protagonists, commonly referred to as ALICE and BOB. *Bell states* are the four maximally-entangled two-dimensional bi-partite states:

$$|\Phi^{\pm}\rangle = \frac{1}{\sqrt{2}}\big(|0\rangle|0\rangle \pm |1\rangle|1\rangle\big)\,, \tag{1.3}$$

$$|\Psi^{\pm}\rangle = \frac{1}{\sqrt{2}}\big(|0\rangle|1\rangle \pm |1\rangle|0\rangle\big)\,. \tag{1.4}$$

In these cases each part of the global state is in a maximally mixed state, $\rho_A = \rho_B = \mathbb{1}/2$, where $\rho_A = \mathrm{Tr}_B\,\rho_{AB}$ and $\rho_B = \mathrm{Tr}_A\,\rho_{AB}$ are the reduced density matrices (obtained by partial tracing) of $\rho_{AB} = |\Psi_{AB}\rangle\langle\Psi_{AB}|$. It is worth noting that such an entangled state can be decomposed in arbitrary bases of the two-dimensional Hilbert space, e.g. $|\Psi^-\rangle = \frac{1}{\sqrt{2}}\big(|0\rangle|1\rangle - |1\rangle|0\rangle\big)$ no matter which basis $\{|0\rangle, |1\rangle\}$ is chosen.

In the following sections we analyze the profound implications of the existence of such states in quantum mechanics, starting from the well-known *EPR paradox*, dating back to 1935.

1.2.1 The Einstein–Podolsky–Rosen paradox

In 1935, Albert EINSTEIN, Boris PODOLSKY and Nathan ROSEN (EPR) argued that quantum mechanics is an incomplete theory [EPR35]. Their argument is based on two "reasonable" concepts that, in their opinion, a physical theory must verify.

– First, the *physical reality* hypothesis. If, without perturbing in any way the state of a system (localized in space-time), we can predict with certainty (with unit probability) the value of a physical quantity of this system, then there exists an *element of reality* associated to this physical quantity. Measurement results on the system are entirely determined by elements of reality, the properties carried on by the system. A complete theory must include all these values.
– Second, the *local relativistic causality* assumption. An action cannot instantaneously influence distant systems, i.e. it cannot have consequences in systems separated by a spacelike interval of spacetime.

Using these concepts —and the notion of entanglement— EPR enunciate a paradox, to which we give a version due to David BOHM and Yakir AHARONOV [BA57].

– Particles A and B, localized in spatially separated regions, are in a Bell state, e.g. $|\Psi_{AB}\rangle = |\Psi^-\rangle$, defined by (1.4).
– Alice measures particle A in basis $\{|0_{b0}\rangle, |1_{b0}\rangle\}$. If she gets result "0", the system collapses to the state $|\Psi_{AB}\rangle = |0_{b0}\rangle|1_{b0}\rangle$ (and similarly if she gets result "1").
– Alice can thus predict with certainty the result that Bob would obtain when measuring his particle in basis $\{|0_{b0}\rangle, |1_{b0}\rangle\}$, without doing anything that could perturb it. Thus particle B possesses the following element of reality: the property 1_{b0}.

– Due to the locality hypothesis, the action in A cannot have created the element of reality of particle B. Thus particle B must have possessed this property before, and independently to, measurement in A.
– However Alice could have chosen to measure her particle in another, non-orthogonal, basis, $\{|0_{b1}\rangle, |1_{b1}\rangle\}$, and get a result, e.g. "0". In that case, she could have concluded that the second particle is in the state $|1_{b1}\rangle$.
– It follows that, before Alice's measurement, particle B should possess both property 1_{b0} and property 1_{b1}. Since these properties are incompatible, this conclusion is in contradiction with quantum formalism.

EPR thus conclude that quantum theory is an incomplete theory, which should be supplemented or replaced by another theory. An alternative way to deal with the paradox is to deny one —or both— of its hypotheses, i.e. deny —against intuition— the notion of *reality* and/or the notion of *locality*. For almost three decades, it seemed to be a philosophical question without a unique possible answer, and most scientists just proceeded with the new theory and its fruitful applications. An important theoretical discovery changed that fact in 1964.

1.2.2 Bell inequalities

The powerful contribution of John Stewart BELL was to show that the predictions of any (hypothetical) local realist model (in the sense of EPR) are inconsistent with those of quantum mechanics [Bel64].

In order to demonstrate this, we consider measurements on entangled states $|\Psi_{AB}\rangle$. In such a case, the joint probability $P(a\,b|x\,y)$ of Alice obtaining result a and Bob obtaining result b given respective measurement parameters x and y cannot be written as a product of individual probabilities, i.e. $P(a\,b|x\,y) \neq P(a|x)\,P(b|y)$. If Nature is intrinsically local realist, then correlations $P(a\,b|x\,y)$ must be an average of more fundamental expressions. We therefore introduce *hidden variables* λ (a set of parameters "hidden" to presently known physics and giving a more complete description of the physical state of the system), such that

$$P(a\,b|x\,y) = \int \mathrm{d}\lambda\,\rho(\lambda)\,P(a\,b|x\,y,\lambda) \tag{1.5}$$

$$= \int \mathrm{d}\lambda\,\rho(\lambda)\,P(a|x,\lambda)\,P(b|y,\lambda)\,, \tag{1.6}$$

for a given probability distribution $\rho(\lambda)$ corresponding to the state $|\Psi_{AB}\rangle$: $\int \mathrm{d}\lambda\,\rho(\lambda) = 1$. The second line is obtained if we consider *local* parameters, i.e. if we make the hypothesis

$$P(a\,b|x\,y,\lambda) = P(a|b\,x\,y,\lambda)\,P(b|x\,y,\lambda) \tag{1.7}$$

$$= P(a|x,\lambda)\,P(b|y,\lambda)\,. \tag{1.8}$$

The first equality corresponds to the definition of conditional probabilities, while the second equality is obtained with the locality hypothesis: the choice and result of Bob's measurement (respectively Alice) cannot influence the result of Alice (respectively Bob).

Here we prove a version of the Bell theorem directly applicable to two-dimensional bi-partite states, the *CHSH inequality*, due to John CLAUSER, Michael HORNE, Abner SHIMONY and Richard HOLT (CHSH) in 1969 [CHSH69]. In the two-dimensional case, results a and b can take two distinct values, $+$ and $-$. We define the *correlator*

$$C(x\,y) = P(++|x\,y) + P(--|x\,y) - P(+-|x\,y) - P(-+|x\,y)\,, \tag{1.9}$$

with $-1 \leq C(x\,y) \leq 1$. Using local parameters λ, we get

$$\begin{aligned} C(x\,y) &= \int \mathrm{d}\lambda\, \rho(\lambda)\, [\, P(+|x,\lambda)\, P(+|y,\lambda) + P(-|x,\lambda)\, P(-|y,\lambda) \\ &\quad -P(+|x,\lambda)\, P(-|y,\lambda) - P(-|x,\lambda)\, P(+|y,\lambda)\,] \qquad (1.10) \\ &= \int \mathrm{d}\lambda\, \rho(\lambda)\, C(x,\lambda)\, C(y,\lambda)\,. \qquad (1.11) \end{aligned}$$

The last expression uses the following definitions:

$$C(x,\lambda) = P(+|x,\lambda) - P(-|x,\lambda)\,, \qquad C(y,\lambda) = P(+|y,\lambda) - P(-|y,\lambda)\,, \qquad (1.12)$$

with $-1 \leq C(x,\lambda) \leq 1$ and $-1 \leq C(y,\lambda) \leq 1$.

We suppose that both Alice and Bob have the choice between two measurements, x_0, x_1 and y_0, y_1. Under the assumption that these choices are not correlated with the parameters λ, we can write:

$$\begin{aligned} \big|C(x_0\,y) \pm C(x_1\,y)\big| &\leq \int \mathrm{d}\lambda\, \rho(\lambda)\, \big|C(x_0,\lambda) \pm C(x_1,\lambda)\big| \times \big|C(y,\lambda)\big| \\ &\leq \int \mathrm{d}\lambda\, \rho(\lambda)\, \big|C(x_0,\lambda) \pm C(x_1,\lambda)\big|\,. \qquad (1.13) \end{aligned}$$

Thus,

$$\begin{aligned} &\big|C(x_0\,y_0) + C(x_1\,y_0)\big| + \big|C(x_0\,y_1) - C(x_1\,y_1)\big| \\ &\leq \int \mathrm{d}\lambda\, \rho(\lambda)\, \big|C(x_0,\lambda) + C(x_1,\lambda)\big| + \int \mathrm{d}\lambda\, \rho(\lambda)\, \big|C(x_0,\lambda) - C(x_1,\lambda)\big|\,. \qquad (1.14) \end{aligned}$$

Because of definitions (1.12), the following inequality is verified:

$$\big|C(x_0,\lambda) + C(x_1,\lambda)\big| + \big|C(x_0,\lambda) - C(x_1,\lambda)\big| \leq 2\,. \qquad (1.15)$$

Combining (1.14) and (1.15), we obtain the CHSH inequality

$$|S| \leq 2\,, \quad \text{with} \quad S = C(x_0\,y_0) + C(x_0\,y_1) + C(x_1\,y_0) - C(x_1\,y_1)\,. \qquad (1.16)$$

It is worth emphasizing that the CHSH inequality should be verified by *any* local realist model, even if it includes some local randomness. On the other hand, quantum mechanics does allow the violation of the inequality. To show this, let us use a Bell state, e.g. $|\Psi^-\rangle$. We consider local measurements projecting onto the states

$$|\theta\rangle = \cos\theta\,|0\rangle + \sin\theta\,|1\rangle\,, \qquad (1.17)$$

such that

$$P(+\,+\,|\alpha\,\beta) = \big|\langle\alpha|\langle\beta|\Psi^-\rangle\big|^2\,. \qquad (1.18)$$

We obtain

$$\begin{aligned} P(+\,+\,|\alpha\,\beta) = P(-\,-\,|\alpha\,\beta) &= \frac{1}{2}\sin^2\big(\alpha-\beta\big)\,, \qquad (1.19) \\ P(+\,-\,|\alpha\,\beta) = P(-\,+\,|\alpha\,\beta) &= \frac{1}{2}\cos^2\big(\alpha-\beta\big)\,. \qquad (1.20) \end{aligned}$$

With (1.9), this implies that

$$C(\alpha\,\beta) = -\cos\big[2(\alpha-\beta)\big]\,. \qquad (1.21)$$

Selecting $\alpha_1 = 0$, $\beta_0 = \pi/8$, $\alpha_0 = \pi/4$, $\beta_1 = 3\pi/8$, we get

$$|S| = 2\sqrt{2} \approx 2.8284 > 2\,. \qquad (1.22)$$

The value $2\sqrt{2}$, obtained with any Bell state, is the maximum allowed by quantum mechanics and is known as the *Tsirelson's bound* [Cir80].

Another inequality, due to John CLAUSER and Michael HORNE in 1974 [CH74], quoted here as the *CH74 inequality*, can be derived from the CHSH inequality. Using $P(+|x) = P(++|x\,y) + P(+-|x\,y)$, $P(+|y) = P(++|x\,y) + P(-+|x\,y)$, and $P(++|x\,y) + P(--|x\,y) + P(+-|x\,y) + P(-+|x\,y) = 1$, (1.9) can be rewritten

$$C(x\,y) = 4P(++|x\,y) - 2P(+|x) - 2P(+|y) + 1\,, \tag{1.23}$$

leading, with (1.16), to

$$P(++|x_0\,y_0) + P(++|x_0\,y_1) + P(++|x_1\,y_0) - P(++|x_1\,y_1) \leq P(+|x_0) + P(+|y_0)\,. \tag{1.24}$$

As will be seen in section 3.1, this inequality can be used in imperfect experimental tests of Bell inequalities.

1.2.3 Bell tests

The Bell theorem opens the way to experimental tests of local realism, leading to results known as *violations of Bell inequalities*. Figure 1.1 shows a typical configuration for a CHSH-type Bell test.

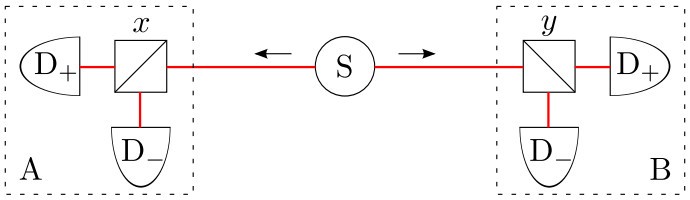

Figure 1.1: Clauser–Horne–Shimony–Holt Bell test. A source S produces a bipartite entangled state, a part being directed to Alice (A) and the other to Bob (B). A and B locally analyze their particle: they perform a measurement with respective binary choice x_0, x_1 and y_0, y_1, registering a "click" in detector D_+ or D_-. A and B events are then compared to evaluate the quantities $C(x_i\,y_j)$, $i, j \in \{0, 1\}$, and therefore the Bell parameter S.

The practical goal of a Bell test is to obtain an experimental estimate of the Bell parameter S (1.16):

$$S_{\text{expt}} = E(x_0\,y_0) + E(x_0\,y_1) + E(x_1\,y_0) - E(x_1\,y_1)\,, \tag{1.25}$$

where estimates $E(x_i\,y_j)$, with $i, j \in \{0, 1\}$, of the correlators (1.9) are

$$E(x_i\,y_j) = \frac{N_{++} + N_{--} - N_{+-} - N_{-+}}{N_{++} + N_{--} + N_{+-} + N_{-+}}\,, \tag{1.26}$$

omitting mentions of $x_i\,y_j$ for clarity of notation. Quantities N_{ab}, $a, b \in \{+, -\}$, are the number of coincident events —detections common to both Alice in a and Bob in b— registered in a given time. The running time of the experiment has to be large enough for the estimation of all $P(a\,b|x\,y)$ be statistically accurate, allowing the violation of Bell inequalities by a given number of standard deviations.

Acquiring enough statistics is not the only concern in a Bell test: one must avoid *loopholes*, and be careful in the analysis of the experiment.

Because of inefficiencies, an experimenter does not collect all the possible outcomes: his measurement apparatus does not produce a result for each particle fired from the source. If the detection probability of each channel falls below a given threshold (equal to $\eta = 2\sqrt{2} - 2 \approx 82.8\%$ for the CHSH inequality [GM87]), then a *fair sampling assumption* —an assumption that some local realist models could break— is needed for the violation of the Bell inequality to be preserved: this is the *detection loophole*.

In order to avoid another important loophole, the *locality loophole*, one must ensure that Alice and Bob's measurements are separated by a spacelike interval of spacetime, so that special relativity forbids any information transfer between Alice and Bob during the measurement process. If this is not the case, one could imagine a local realist explanation involving such an information transfer.

In the derivation of the Bell inequality, although the parameters λ can include the whole past of the whole universe, the choices x and y must be independent of λ. Choices of measurement settings must thus be made —randomly— after the emission and separation of the particles, "just before" the measurement. This opens the so-called —almost provocatively— *free will loophole*. In a kind of desperate solution, one could abandon the notion of free will to preserve local realism in a "super-deterministic" theory.

Bell tests have been gradually refined since the first one, performed by Stuart J. FREEDMAN and John F. CLAUSER in 1972 [FC72]. The experiment of Alain ASPECT and his collaborators is famous for closing the locality loophole while testing the CHSH inequality with pseudo-random measurement parameters [ADR82]. Since then, several experiments have closed the locality loophole, enhancing randomness and independence of Alice and Bob [WJS$^+$98], or even performing a "before–before" experiment, where the two protagonists, traveling fast in opposite directions, make their own measurement before the other in their particular frame [SZGS02, SZGS03]. Most of the experimental demonstrations make use of photons, which are easily transferred. On the other hand, they are not easily detected, as single-photon detectors' efficiencies remain relatively poor; for photons, the detection loophole has been closed only recently by using a particular Bell inequality involving non-maximally entangled states [GMR$^+$13]. Bell tests have also been performed with quantum states of material systems —see e.g. [RKM$^+$01, AWB$^+$09]— easier to detect, but more difficult to transmit at high distances.

A decisive Bell test closing simultaneously all the main loopholes has yet to be conducted, although repeated experimental violations of Bell inequalities in various circumstances make it hard to believe that a natural "conspiracy" would be at work to make us believe that the world is not local realist. These violations seem to compel us to abandon the notion of physical reality or the idea of locality, or both. Because quantum correlations —"spooky actions at a distance" in Einstein's words— seem to appear outside space-time, without propagating from one point to the next in space, violations of Bell inequalities are often quoted as evidence of *quantum nonlocality* [Gis14].

As nonlocal correlations do exist, they could be used to communicate information. However, the *no-communication theorem* states that a local measurement —on one subsystem of an entangled state— cannot be used to directly communicate information to a separate observer. Indeed, the correlations $P(a\,b|x\,y)$ cannot be used to communicate because the marginal distributions do not depend on the input from the other protagonist:

$$\sum_b P(a\,b|x\,y) = P(a|x) \quad \text{and} \quad \sum_a P(a\,b|x\,y) = P(b|y)\,, \tag{1.27}$$

obtained by partial tracing in the quantum formalism. Due to the intrinsic random nature of quantum measurements, nonlocal correlations do not lead to instantaneous communication. These no-signaling conditions impose strong constraints but, as we shall see, they do not rule out entanglement as a powerful way to transmit quantum information.

1.3 Quantum optics and quantum communication

1.3.1 Photons

Photons are the preferred *flying qubit* because they can travel long distances without interacting with the environment, implying low loss and low decoherence. The field of quantum optics [MW95] is thus closely related to quantum information and communication [NC10]. The ability to create, manipulate, and transmit the quantum state of photons has enabled applications such as quantum cryptography as well as foundational experiments concerning, for instance, quantum nonlocality and quantum teleportation. Hereafter, we briefly introduce the basic notions of quantum optics needed to describe photonic implementations of interest for quantum communication.

A photon is an excitation of the quantized electromagnetic field. A *Fock state* $|n\rangle$ contains exactly n photons. We define creation and annihilation operators $a^\dagger$ and a by the relations

$$a^\dagger|n\rangle = \sqrt{n+1}|n+1\rangle\,, \qquad a|n\rangle = \sqrt{n}|n-1\rangle\,, \qquad a|0\rangle = 0\,, \tag{1.28}$$

where $|0\rangle$ is the vacuum state, for which $n = 0$. $N = a^\dagger a$ is the photon number observable. A Fock state can in principle be obtained from the vacuum by adding photons one by one: $|n\rangle = (a^\dagger)^n/\sqrt{n!}\,|0\rangle$. However, in practice, Fock states are very difficult to produce.

Fock states form a basis allowing to describe all the states of the electromagnetic field. The eigenstates of the annihilation operator, called *coherent states* and denoted $|\alpha\rangle$, can be written

$$|\alpha\rangle = \mathrm{e}^{-|\alpha|^2/2} \sum_{n=0}^{\infty} \frac{\alpha^n}{\sqrt{n!}}|n\rangle\,. \tag{1.29}$$

The mean number and the variance of photons are respectively $\langle n\rangle = |\alpha|^2$ and $(\Delta n)^2 = \langle n\rangle$. The probability to find n photons in the field is

$$p_n = \frac{\langle n\rangle^n}{n!}\mathrm{e}^{-\langle n\rangle}\,, \tag{1.30}$$

a Poisson distribution. The light emitted by a long-coherence laser operating largely above threshold is well approximated by a coherent state [GC08]. Lasers are often used as convenient sources of "single photons", with $\langle n\rangle < 1$, typically $n = 0.1$ or 0.2. This however presents important drawbacks, since $p_{n>0} < 1$ and $p_{n>1} > 0$, leading to inefficiencies and possible security loopholes in applications such as quantum cryptography. Several approaches towards more efficient sources of single photons (Fock states with $n = 1$) are undertaken. This includes nitrogen-vacancy centers in diamond [KMZW00, BHK$^+$10], semiconductor junctions [YKS$^+$02], quantum dots [MKB$^+$00, BLC$^+$11], etc. [EFMP11]

Photon-pair sources are mainly based on spontaneous parametric down-conversion in a second-order ($\chi^{(2)}$) nonlinear crystal or waveguide [MW95]. In this process, photons of a (pulsed or continuous-wave) long-coherence pump laser split into two daughter photons, traditionally called *signal* (s) and *idler* (i) photons. Momentum and total energy are conserved; because of energy conservation, photons are entangled in energy-time. In type I conversion, both photons have the same polarization; in type II, photons can be polarization-entangled [KMW$^+$95, MIH$^+$10]. Photon pairs can also be produced using processes related to the third-order ($\chi^{(3)}$) nonlinearity. Recent research focuses on integration of photon-pair sources, see chapter 4. Note that these processes are probabilistic, so that the produced state contains vacuum and multiple pairs; one has to work in a regime where multi-pair emission is negligible. Note finally that photon-pair sources can be used as heralded single-photon sources.

1.3.2 Quantum interference

Quantum states of light can be manipulated with standard optical components. Actions of linear optical components obey the *correspondence principle*: photon probability amplitudes propagate as complex optical fields in coherent optics. Let us consider a simple and very useful linear optical component, the *beam splitter* (BS) schematized in figure 1.2.

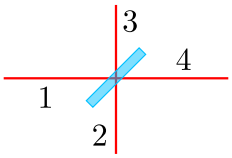

Figure 1.2: Beam splitter with two inputs (1 and 2) and two outputs (3 and 4).

An incident light beam is partially transmitted and partially reflected. In a quantized description, it corresponds to the following unitary transformation U_{BS} acting on the annihilation operators:

$$\begin{pmatrix} a_3 \\ a_4 \end{pmatrix} = U_{\mathrm{BS}} \begin{pmatrix} a_1 \\ a_2 \end{pmatrix}, \qquad U_{\mathrm{BS}} = \begin{pmatrix} c_{31} & c_{32} \\ c_{41} & c_{42} \end{pmatrix}, \tag{1.31}$$

where a_i is the annihilation operator of mode i. The complex coefficients c_{ij} obey amplitude and phase relations for the transformation to be unitary —implying conservation of energy, and thus of the number of photons in linear optics. Assuming spatial symmetry, we can note $c_{31} = c_{42} = r$ and $c_{32} = c_{41} = t$, with $|r|^2 + |t|^2 = 1$ and $\varphi_r = \varphi_t + \pi/2$.

A single photon incident on the beam splitter (e.g. in mode 1) ends up in a spatial superposition of modes 3 and 4:

$$|1\rangle_1|0\rangle_2 = a_1^\dagger|0\rangle_1|0\rangle_2|0\rangle_3|0\rangle_4 = \left(ra_3^\dagger + ta_4^\dagger\right)|0\rangle_1|0\rangle_2|0\rangle_3|0\rangle_4 = r|1\rangle_3|0\rangle_4 + t|0\rangle_3|1\rangle_4\,, \tag{1.32}$$

where $|n\rangle_i$ denotes the presence of n photons in mode i. If the beam splitter is "50/50", i.e. when $|r|^2 = |t|^2 = 0.5$, the photon is measured in output 3 or 4 with equal probability. Such a setup can be used for quantum random number generation.

When a single photon is incident on each input, we readily obtain

$$|1\rangle_1|1\rangle_2 = \sqrt{2}rt|2\rangle_3|0\rangle_4 + \left(r^2 + t^2\right)|1\rangle_3|1\rangle_4 + \sqrt{2}rt|0\rangle_3|2\rangle_4\,. \tag{1.33}$$

In the case of a 50/50 beam splitter, $r^2 + t^2 = 0$, and the photons always quit the beam splitter through the same output. This two-photon interference effect is known as a *Hong–Ou–Mandel dip* [HOM87]: experimentally it is detected as a drop in coincident detections in modes 3 and 4 for a delay between modes 1 and 2 corresponding to a simultaneous arrival of the photons at the beam splitter. The temporal width of the dip is linked to the photons' coherence time. When the photons arrive on the beam splitter at different times, they become distinguishable, and no interference occurs. This is also valid if the photons are distinguishable in other characteristics, such as wave profile, wavelength, or polarization. The visibility of the dip is related to the degree of indistinguishability of the two photons.

Because a beam splitter creates spatial coherent quantum superpositions, it can be used to produce *single-photon interferences*. The setup depicted in figure 1.3 is a Mach–Zehnder interferometer (MZI). It is made of two consecutive beam splitters, the paths being recombined on the second beam splitter with mirrors; optical-fiber and waveguide-integrated versions of MZIs also exist.

A photon can travel along paths A and B, acquiring phase φ_{A} or φ_{B}, respectively. Applying (1.31) two times, one obtains that the probabilities of registering the photon at detectors D_+

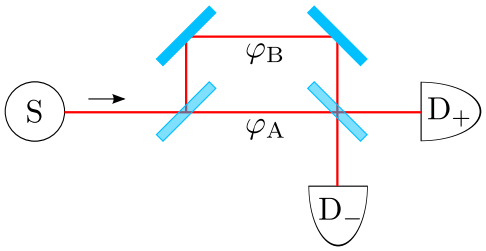

Figure 1.3: Mach–Zehnder interferometer. A source S produces a single photon, which is directed by beamsplitters and mirrors through two distinct paths A and B, with phase difference $\varphi = \varphi_A - \varphi_B$. The setup exhibits single-photon interference: the probability of registering the photon at detector D_+ or D_- depends on φ.

and D_- (given a photon is emitted by the source and considering no-loss components) are respectively

$$P_+ = 1 - 4|r|^2|t|^2\cos^2(\varphi/2) \quad \text{and} \quad P_- = 4|r|^2|t|^2\cos^2(\varphi/2)\,. \tag{1.34}$$

These probabilities depend on $\varphi = \varphi_A - \varphi_B$: this is the experimental signature of single-photon interference.

1.3.3 Time-bin encoding

The setup of figure 1.3 can be used to encode and transmit quantum information, if Alice controls the source and one arm of the interferometer, and Bob controls the detectors and the other arm of the interferometer. However, the large-scale implementation of the setup is impracticable. A sub-wavelength stabilization of the interferometer is needed for the phases φ_A and φ_B to be fixed with precision. This is impossible if Alice and Bob are separated by kilometers of free space or optical fiber: small changes in constraints applied to one or the other channel imply great variations of φ_A and φ_B, because wavelengths are of the order of the micrometer and length variations will typically be several millimeters.

To get rid of this problem, researchers have proposed to use MZIs to produce *time bins*, see e.g. [RGG+98]. A photon incident on a 50/50 MZI of time unbalance τ and phase difference φ ends up in the temporal superposition:

$$|\psi\rangle = \frac{1}{\sqrt{2}}\left(|0\rangle + e^{i\varphi}|1\rangle\right), \tag{1.35}$$

where the states $|0\rangle$ and $|1\rangle$ correspond to a photon localized at different positions in the output channel, i.e. which should be detected at respective times t and $t+\tau$. We consider here only one spatial output, leading to a 50% encoding efficiency with the basic setup of figure 1.3. Quantum information can be encoded in the relative phase φ. A quantum communication setup based on time bins is presented in figure 1.4.

In the present case, Alice controls the source and the first MZI, while Bob controls the detectors and the second MZI. The MZIs can be stabilized and controlled with precision in Alice's and Bob's labs. The two parts of the superposition (1.35) now travel along the same physical channel with a delay that can be made very small; they thus encounter approximately the same conditions —which significantly vary typically in nanoseconds— implying very low decoherence. We note that the spacing τ between the time bins is ultimately limited by the time resolution of the single-photon detectors; the photons whose arrival time cannot be distinguished by the detectors belong to the same time bin.

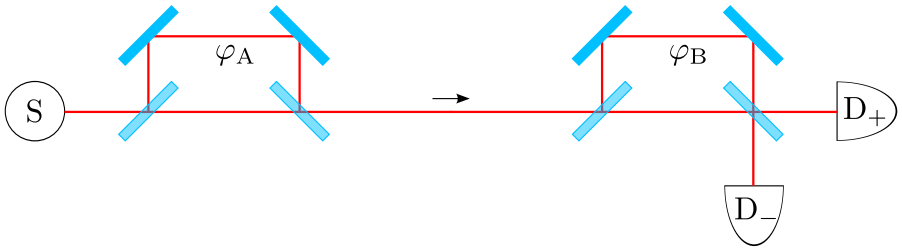

Figure 1.4: Single-photon interference in the spatio-temporal domain. A source S emits a single photon at time t_0. It propagates through consecutive MZIs, of same time unbalance τ and respective phase differences φ_A and φ_B. The photon is detected in detector D_+ or D_- at time t, $t+\tau$ or $t+2\tau$, with $t = t_0 + t_*$, t_* being the overall transmission time of the line for the short paths. The intermediate case exhibits single-photon interference.

A photon emitted at time t_0 by the source can reach detector D_+ or D_- by following the short path of each interferometer, or the long path of each interferometer, or one short path and one long path. In this last case, for same time unbalances τ, it is impossible to know if the combination was short–long or long–short. This indistinguishability permits single-photon interference. The probabilities of registering the photon in detectors D_+ or D_- at times t, $t+\tau$ and $t+2\tau$, with $t = t_0 + t_*$, where t_* is the overall transmission time of the line for the short paths, are then:

$$P_\pm(t) = P_\pm(t+2\tau) = \frac{1}{8}\,, \qquad P_\pm(t+\tau) = \frac{1}{4}\big[1 \pm \cos\big(\varphi_A - \varphi_B\big)\big]\,. \tag{1.36}$$

In half of the cases, i.e. for intermediate flight times, single-photon interference is observed.

Figure 1.5 represents a *Franson interferometer*, based on a 1989 proposal [Fra89]. Here we consider a source S of time-entangled photons: the emission time of each photon is uncertain but both photons are emitted simultaneously. In a time-bin (discretized) implementation, this would correspond to emission times t_0 and $t_0+\tau$. This can be done by using a long-coherence laser (coherence time τ_p) whose power is split by an unbalanced MZI before pumping a nonlinear waveguide. The photons are separated and sent to distinct MZIs of unbalance τ.

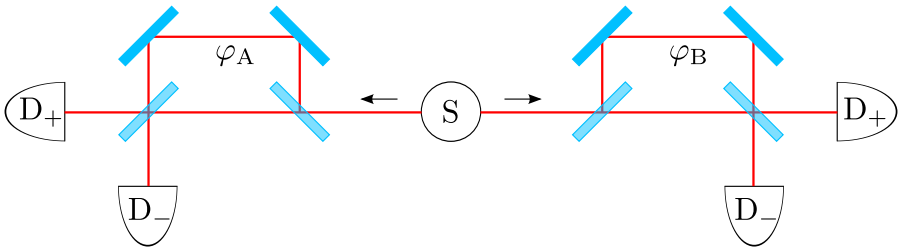

Figure 1.5: Two-photon interference in the spatio-temporal domain. In this Franson interferometer, a source S produces time-entangled photons, which are separated and sent through distinct unbalanced MZIs. When Alice's and Bob's photons are detected in coincidence, they exhibit two-photon interference: the joint probabilities P_{ab}, with $a, b \in \{+,-\}$, depend on $\varphi_A + \varphi_B$.

The signal and idler photons produced by the source have a coherence time τ_1, while the biphoton coherence time is τ_2. If the condition $\tau_1 \ll \tau \ll \tau_2$ is satisfied, no single-photon interference occurs, so that individual probabilities $P_\pm = 1/2$ for both Alice and Bob, but analysis of the *correlations* between Alice's and Bob's results reveals a phenomenon called *two-photon interference*. Indeed, if Alice's and Bob's photons are detected simultaneously, one cannot know

if they both took the short path of their interferometer, or if they both took the long path. Quantitatively, we obtain the joint probabilities P_{ab}, with $a, b \in \{+, -\}$, of Alice registering result a and Bob registering result b:

$$P_{++} = P_{--} = \frac{1}{4}\big[1 + \cos\big(\varphi_A + \varphi_B\big)\big] \quad \text{and} \quad P_{+-} = P_{-+} = \frac{1}{4}\big[1 - \cos\big(\varphi_A + \varphi_B\big)\big] \tag{1.37}$$

for detection times $\tau_B - \tau_A = t_\delta$, for some delay t_δ imposed by the channels' length difference. This requires time-resolved *coincidence* measurements. No interference occurs for satellite coincidence peaks at $\tau_B - \tau_A = t_\delta \pm \tau$.

1.3.4 Polarization encoding

Polarization has been a widely used degree of freedom in quantum optics. It indeed offers a natural two-dimensional Hilbert space, and is easily accessed experimentally with standard polarization-sensitive components. The correspondence principle applies in the polarization domain: elements will act on photon probability amplitudes as for complex fields in coherent optics. Typical optical components for manipulating the polarization state of photons are phase plates and polarizers. Their effect can be expressed in the form of transfer matrices known as *Jones matrices* J:

$$|\psi\rangle_{\text{out}} = J|\psi\rangle_{\text{in}} \quad \text{with} \quad J = J^{(n)} \dots J^{(1)}\,, \tag{1.38}$$

with $J^{(i)}$ the Jones matrix of element i. All the matrices are defined in the same arbitrary reference axes perpendicular to the propagation direction, e.g. (x, y). If the eigen-axes (u, v) of a component are rotated by an angle θ in regards of (x, y), we have:

$$J_{xy} = R(\theta)\, J_{uv}\, R(-\theta) \quad \text{with} \quad J_{uv} = \begin{pmatrix} 1 & 0 \\ 0 & \eta e^{i\epsilon} \end{pmatrix}\,, \tag{1.39}$$

where $R(\theta)$ is a rotation matrix of angle θ. For phase plates, $\eta = 1$, with $\epsilon = \pi$ for a half-wave plate and $\epsilon = \pi/2$ for a quarter-wave plate; their combination allows arbitrary manipulation of a photon polarization state. For a polarizer, $\eta = 0$: it will act as a projector on a given axis. Together with phase plates, it allows the projection on any axis: rotation of a polarization state followed by a fixed projection is equivalent to a projection on a different axis. *Polarizing beam splitters* (PBS) are very useful components that spatially separate two linear polarizations, i.e. they are polarizers with two outputs.

Single-photon interference is obtained by first polarizing a photon at angle θ_A. Viewed from any other axis, the photon is in a superposition of two different linear polarizations. Then, the probability of the photon passing through a second polarizer with passing axis at angle θ_B is equal to P_+:

$$P_+ = \cos^2\big(\theta_A - \theta_B\big) \quad \text{and} \quad P_- = \sin^2\big(\theta_A - \theta_B\big)\,, \tag{1.40}$$

with P_- the probability of detecting the photon at the complementary output when a PBS is used. This is the quantum analogue of *Malus law*. The experimental configuration is illustrated in figure 1.6.

In figure 1.7, we consider a source S emitting two photons in a polarization-entangled state $|\Psi\rangle$, for example the Bell state $|\Phi^+\rangle = \big(|HH\rangle + |VV\rangle\big)/\sqrt{2}$, where H, V denote horizontal and vertical linear polarizations. Applying quantum formalism, i.e. $P_{++} = \big|\langle\theta_A|\langle\theta_B|\Psi\rangle\big|^2$, we readily get the joint probabilities P_{ab}, $a, b \in \{+, -\}$. For the Bell state $|\Phi^+\rangle$,

$$P_{++} = P_{--} = \frac{1}{2}\cos^2\big(\theta_A - \theta_B\big) \quad \text{and} \quad P_{+-} = P_{-+} = \frac{1}{2}\sin^2\big(\theta_A - \theta_B\big) \tag{1.41}$$

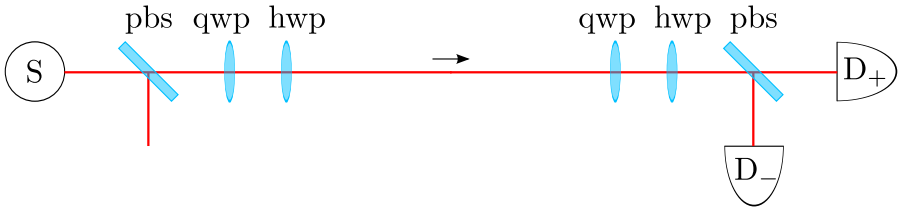

Figure 1.6: Single-photon interference in the polarization domain. A source S produces a single photon whose polarization state is fixed by a first polarizing beam splitter PBS at passing angle θ_A. The probability for the photon to be detected in detector D_+ or D_- behind a second PBS at angle θ_B depends on $\theta_A - \theta_B$. Half-wave plates (HWP) and quarter-wave plates (QWP) allow to implement θ_A and θ_B for fixed PBS, and possibly for polarization management, i.e. compensation of the polarization rotations imposed by the channel.

exhibit two-photon interference. For a Bell state, one can notice that individual probabilities all sum up to 1/2, because each individual photon is in a maximally mixed state, therefore producing no single-photon interference. For non-maximally entangled states, both one- and two-photon interferences are observed.

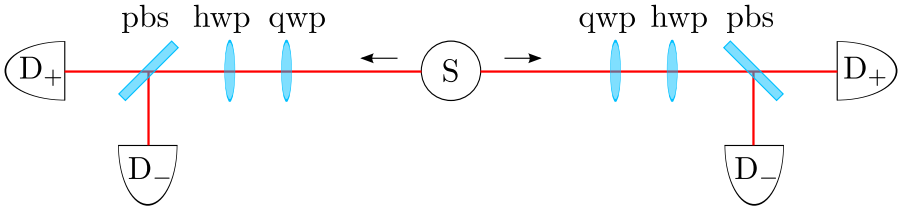

Figure 1.7: Two-photon interference in the polarization domain. A source S emits a polarization-entangled state. Each photon is manipulated by its own analyzer, composed of a quarter-wave plate (QWP), a half-wave plate (HWP) and a polarizing beam splitter (PBS) allowing to implement a projection at any angle $\theta_{A,B}$. Analysis of the correlations between Alice's and Bob's results reveals two-photon interference.

There exist fiber-optic versions of all the polarization components. Active polarization management is needed to compensate for the polarization drifts caused by the quantum channel. This has to be monitored against a fixed common reference.

Finally, we note that the association QWP–HWP–PBS constitutes a polarization analyzer which can be used to perform *polarization tomography*. Tables 1.1 and 1.2 list the measurements needed to characterize a single-photon state and a two-photon state, respectively. These measurements have to be carried on identically prepared photons and repeated enough for an accurate evaluation of individual or joint probabilities.

1.3.5 Quantum cryptography

We now illustrate how one- and two-photon interferences can be useful by considering the following situation: Alice wishes to transmit a confidential message M to Bob. She only has access to a public channel. If Alice wants to guarantee the secret of the transfer, she must share a *private key* K with Bob, and it has to be as long as her message. By sending the bitwise combination $C = M \oplus K$ to Bob, only him can recover the original message $M = C \oplus K$. The security of this protocol, known as the *Vernam cipher*, is mathematically demonstrated. This is the only known absolutely secure cryptographic scheme. The problem thus reduces to the

Table 1.1: Single-photon polarization tomography. The table lists the measurements allowing a complete characterization of a single-photon state. The angular positions of the phase plates (QWP and HWP) preceding the polarizer are indicated.

measure	mode	hwp(°)	qwp(°)
1	V	0	0
2	H	45	0
3	R	22.5	0
4	D	22.5	45

Table 1.2: Two-photon polarization tomography. The table lists the coincidence measurements that Alice and Bob must make for a complete characterization of a two-photon state. The angular positions of the phase plates (QWP and HWP) preceding the polarizers are indicated. Adapted from [JKMW01].

measure	mode_A	mode_B	$\text{hwp}_\text{A}(°)$	$\text{qwp}_\text{A}(°)$	$\text{hwp}_\text{B}(°)$	$\text{qwp}_\text{B}(°)$
1	H	H	45	0	45	0
2	H	V	45	0	0	0
3	V	V	0	0	0	0
4	V	H	0	0	45	0
5	R	H	22.5	0	45	0
6	R	V	22.5	0	0	0
7	D	V	22.5	45	0	0
8	D	H	22.5	45	45	0
9	D	R	22.5	45	22.5	0
10	D	D	22.5	45	22.5	45
11	R	D	22.5	0	22.5	45
12	H	D	45	0	22.5	45
13	V	D	0	0	22.5	45
14	V	L	0	0	22.5	90
15	H	L	45	0	22.5	90
16	R	L	22.5	0	22.5	90

need of sharing a private key on a public channel. The subject known as quantum cryptography provides a solution in the form of *quantum key distribution* (QKD) [GRTZ02].

The idea behind quantum key distribution is to exploit no-go theorems implied by the quantum formalism —the no-cloning theorem and the existence of incompatible properties— to guarantee that a potential eavesdropper EVE does not have information on the exchanged key. Here we present the most known quantum key distribution protocol, the *BB84 protocol*, named after the proposal of Charles BENNETT and Gilles BRASSARD in 1984 [BB84]. In this protocol, information is shared via non-orthogonal quantum states. It uses four states from *maximally conjugated* bases $b0$ and $b1$, for example

$$|0_{b0}\rangle \qquad \text{and} \qquad |1_{b0}\rangle\,, \tag{1.42}$$

$$|0_{b1}\rangle = \frac{1}{\sqrt{2}}\big(|0_{b0}\rangle + |1_{b0}\rangle\big) \qquad \text{and} \qquad |1_{b1}\rangle = \frac{1}{\sqrt{2}}\big(|0_{b0}\rangle - |1_{b0}\rangle\big)\,. \tag{1.43}$$

The measurement of a state of a given basis in the other basis gives a perfectly random result:

$$\big|\langle i_{b0}|j_{b1}\rangle\big|^2 = \frac{1}{2}\,, \tag{1.44}$$

with $i, j \in \{0, 1\}$. Such a measurement does not provide any information on the state. On the other hand, information can be accurately shared when a state is measured in the correct basis.

The protocol, schematized in table 1.3, goes as follows. Alice randomly prepares her photons in the four states $|i_{bj}\rangle$, $i, j \in \{0, 1\}$, with equal probability. She sends them on a quantum channel, e.g. an optical fiber. At the reception, Bob randomly selects a measurement basis. After the transmission of all photons is complete, Alice publicly announces her chosen bases (without telling which state was coded). She and Bob discard all the bits corresponding to states measured in the wrong basis, rejecting approximately half the bits of the raw key (containing approximately 25% errors) to obtain a sifted key in principle free of errors.

Table 1.3: BB84 protocol sequence. Alice randomly prepares her photons in the four states $|i_{bj}\rangle$, $i, j \in \{0, 1\}$, measured by Bob in one of two randomly chosen bases. After reconciliation of the bases, they share a list of secret classical bits, the sifted key.

states prepared by Alice	0_{b0}	0_{b0}	1_{b1}	0_{b1}	0_{b0}	0_{b1}
Bob's measurement bases	$b0$	$b1$	$b1$	$b1$	$b0$	$b0$
Bob's results	0	0 or 1	1	0	0	0 or 1
bits retained in the sifted key	0	–	1	0	0	–

Table 1.4 illustrates a possible strategy followed by an eavesdropper, known as the *intercept–resend* attack. Eve intercepts each photon produced by Alice, measures them, and resends to Bob photons in a state corresponding to the results of her measurements. The key point for the security of the protocol is that there is no possibility for Eve to know which basis Alice has used, so that the density matrix of the states corresponds to a maximally mixed state. Moreover, she cannot keep a copy of the states because of the no-cloning theorem. She must therefore choose at random —like Bob— her measurement. In half of the cases, her result will be random; in half of these cases she will introduce errors in the sifted key. By comparing a subset of their key, Alice and Bob can evaluate the *quantum bit error rate* (QBER) and detect her presence.

Table 1.4: BB84 protocol sequence with intercept–resend attack. Eve tries to measure the qubits sent by Alice, before sending to Bob a state corresponding to her measurement result. Her actions introduce errors in the sifted key (highlighted in the last line), which can be detected by Alice and Bob by comparing a subset of their bit string.

states prepared by Alice	0_{b0}	0_{b0}	1_{b1}	0_{b1}	0_{b0}	0_{b1}
Eve's measurements bases	$b1$	$b0$	$b1$	$b0$	$b0$	$b0$
Eve's results	0 or 1	0	1	0 or 1	0	0 or 1
states prepared by Eve	0_{b1} or 1_{b1}	0_{b0}	1_{b1}	0_{b0} or 1_{b0}	0_{b0}	0_{b0} or 1_{b0}
Bob's measurement bases	$b0$	$b1$	$b1$	$b1$	$b0$	$b0$
Bob's results	0 or 1	0 or 1	1	0 or 1	0	0 or 1
bits retained in the sifted key	**0 or 1**	–	1	**0 or 1**	0	–

To demonstrate the security of the protocol, all the errors have to be inputed to the action of an eavesdropper, who could have gain information through them. For a QBER below a given threshold, procedures of error correction and privacy amplification guarantee Alice and Bob to share a secret key. The BB84 protocol is secure against individual (photon per photon) attacks if

$$\text{QBER} < \frac{1 - 1/\sqrt{2}}{2} \approx 15\% \,. \tag{1.45}$$

This is precisely the maximal value allowed to obtain a violation of the CHSH inequality. Indeed, the value of the Bell parameter is $S = 2\sqrt{2}\,(1 - 2\,\mathrm{QBER})$, corresponding to a visibility of interferences of 70.7%. It is interesting to note the links between fundamental and practical experiments; the CHSH inequality is also the basis for some of the most important potential applications of nonlocality, such as device-independent key distribution [ABG+07] and randomness expansion [PAM+10].

Actually, there is a mathematical correspondence between correlation experiments on maximally entangled states and prepare-and-measure schemes, based on the identity

$$\langle i|\langle j|U_\mathrm{A}\otimes U_\mathrm{B}|\Phi^+\rangle = \frac{1}{\sqrt{d}}\langle i|U_\mathrm{A}U_\mathrm{B}^T|j\rangle\,, \tag{1.46}$$

where $|\Phi^+\rangle = \sum_{i=1}^{d}|i\rangle|i\rangle/\sqrt{d}$, and T is the transposition operation in basis $\{|i\rangle\}$. Indeed, the first term in the equality can be interpreted as a measurement on the entangled state $|\Phi^+\rangle$ in which Alice projects onto $\langle i|U_\mathrm{A}$ and Bob projects onto $\langle j|U_\mathrm{B}$, whereas the second term can be interpreted as the preparation by Bob of the state $U_\mathrm{B}^T|j\rangle$ and the subsequent projection by Alice onto the state $\langle i|U_\mathrm{A}$. This theoretical correspondence is well established in the context of quantum key distribution, where it is used to demonstrate the equivalence between prepare-and-measure schemes and entanglement-based schemes [SP00].

Entanglement-based schemes follow the 1991 proposal of Artur K. EKERT [Eke91], which constituted a revolution in the field of quantum communication. Such an EPR protocol uses correlation measurements on Bell states $|\Phi^+\rangle$. The security of the original protocol is guaranteed by the violation of a Bell inequality, though this is not needed to guarantee the security of a quantum cryptography protocol [BBM92].

Practical implementations thus make use of single- or two-photon interferences. Key distribution protocols over distances greater than a few hundreds of kilometers [WZY02, SBG+05, MFL07, TNZ+07, SUF+09, FUH+09, SST11] and security certification without *a priori* trust in the devices employed [ABG+07] have been demonstrated. Entanglement-based setups follow closely physical implementations of Bell tests, i.e. the preferred methods are polarization encoding [JSW+00, NPW+00] and time-bin encoding [ERTP92, TBZG00].

1.3.6 Quantum teleportation

Quantum teleportation is an important building block for most applications in quantum computing and quantum communication. It allows to transmit an arbitrary unknown quantum state $|\psi\rangle$ to a distant partner, given the two protagonists share an entangled state, e.g. $|\Phi^+\rangle$.

The protocol goes as follows [BBC+93]. Alice possesses a quantum system in the (supposedly pure in our description) state $|\psi\rangle = \alpha|0\rangle + \beta|1\rangle$, to be teleported, and one particle of the entangled state $|\Phi^+\rangle$. Bob possesses the other part of $|\Phi^+\rangle$. The global state of the three-particle system is thus

$$\begin{aligned}|\psi\rangle|\Phi^+\rangle &= \big(\alpha|0\rangle+\beta|1\rangle\big)\frac{1}{\sqrt{2}}\big(|00\rangle+|11\rangle\big)\\ &= \frac{1}{2}\big[|\Phi^+\rangle|\psi\rangle + |\Phi^-\rangle\sigma_z|\psi\rangle + |\Psi^+\rangle\sigma_x|\psi\rangle + |\Psi^-\rangle\sigma_x\sigma_z|\psi\rangle\big]\,,\end{aligned} \tag{1.47}$$

where in the second line we used the fact that

$$|00\rangle = \big(|\Phi^+\rangle+|\Phi^-\rangle\big)/\sqrt{2}\,, \qquad |01\rangle = \big(|\Psi^+\rangle+|\Psi^-\rangle\big)/\sqrt{2}\,, \tag{1.48}$$

$$|10\rangle = \big(|\Psi^+\rangle-|\Psi^-\rangle\big)/\sqrt{2}\,, \qquad |11\rangle = \big(|\Phi^+\rangle-|\Phi^-\rangle\big)/\sqrt{2}\,, \tag{1.49}$$

and the definitions

$$\sigma_z = \begin{pmatrix} 1 & 0 \\ 0 & -1 \end{pmatrix}, \quad \sigma_x = \begin{pmatrix} 0 & 1 \\ 1 & 0 \end{pmatrix}, \quad \sigma_x\sigma_z = -i\sigma_y = \begin{pmatrix} 0 & -1 \\ 1 & 0 \end{pmatrix}. \tag{1.50}$$

To teleport the state, Alice must perform a *Bell state measurement* —which can be (partially) realized using a beam splitter or a PBS. This projects Bob's qubit onto one of four possibilities. To recover ψ, Bob has to know the random result of Alice's measurement and rotate his qubit accordingly. The teleportation protocol can be viewed as a sort of "ultimate cryptography", because it implies the transmission of only a random classical bit.

The first experimental implementation used polarization entanglement [BPM$^+$97], but many implementations have followed. An important subclass of teleportation is the *entanglement swapping* protocol, i.e. the teleportation of entanglement [ZZHE93]. Two independent sources of photon pairs are used. Upon a coincident detection of a photon from each source behind a common beam splitter, the two remaining photons become entangled, though they never interacted. Such an experiment has been performed in the time domain by using narrow-band filters so that the coherence time of the photons exceeds the temporal resolution of the detectors [HBG$^+$07].

Chapter 2

Frequency-bin entangled photons

In the framework of quantum communication at telecommunication wavelengths —in the C-band around 1550 nm— the energy-time degree of freedom is particularly interesting, as it is transmitted essentially undisturbed through optical fibers. Energy-time entanglement can be produced, manipulated and detected by using various implementations. Our aim is to experimentally demonstrate a new method for the original manipulation of the frequency degree of freedom of energy-time entangled photons. This is done using standard telecommunication components.

Investigation of energy-time entanglement has been mainly inspired by two-photon bunching experiments [HOM87, OM88, RT90b, KKK03, FHA$^+$09], and by Franson's proposal for addressing the entanglement in the time domain [Fra89], see section 1.3. We briefly recall it here. First, a source produces time-entangled photons: photons are created simultaneously, but their emission time is uncertain. Second, one uses measurements that resolve the arrival time of the photons; photons whose arrival time cannot be discriminated by the detector are said to lie in the same *time bin*. Third, different time bins are made to interfere via unbalanced Mach–Zehnder interferometers The time-bin approach has become the most common platform for manipulating energy-time entangled photons at telecommunication wavelengths [BMM92, KSC93, TRT93, TRO94, TBZG98, TBG$^+$98, TBGZ99, BGTZ99, TBZG00, TTT$^+$02, MDRT$^+$02, MDRT$^+$04].

Energy-time entanglement can also be viewed as frequency entanglement. Here we show how to address energy-time entanglement directly in the frequency domain. There is an interesting conceptual parallel with Franson's approach. First, a monochromatic pump laser produces frequency-entangled photon pairs: the frequency of each photon is uncertain, but the sum of the frequencies is well defined. Second, our detectors are preceded by narrow-band frequency filters that resolve the frequency of the photons. This leads to the concept of *frequency bin*: two photons whose frequency is so close that they cannot be distinguished by the filters are said to lie in the same frequency bin. Third, different frequency bins are made to interfere by using electro-optic phase modulators (EOPMs) driven by radio-frequency (RF) signals.

Manipulation of energy-time entangled photons directly in the frequency domain remains a relatively unexplored area. Other works on frequency entanglement comprise: analysis of bunching experiments [FHA$^+$09], conversion from polarization to frequency entanglement [RRF$^+$09], demonstration of discrete frequency entanglement [LYM$^+$09], and study of hyper-entangled photons —photons entangled simultaneously in both energy-time and other degrees of freedom [SS94, BLPK05]. Phase modulation of quantum light has also been studied in, e.g., [Har08, SYH09, CFP10]. We note that the use of narrow-band filters together with a spectrally bright PPLN source of entangled photons has been reported previously in the context of four-photon experiments [HBT$^+$08, HBG$^+$07].

Our work is inspired by, or related to, earlier proposals for manipulating qubits in the frequency domain, e.g. [MMG+99b, MMGR99, MMG+99a, SZGS03, HR04, HMR+05, BMMP07]. Our experimental techniques follow closely those of quantum key distribution (QKD) systems in which the quantum information is encoded in the frequency sidebands of an attenuated coherent state [MMG+99b, MMGR99, MMG+99a, BMMP07]. Such systems allow efficient transmission of quantum information at telecommunication wavelengths. The main advantage of this method for encoding and carrying out transformations on optical qubits is that one does not need to stabilize paths in optical interferometers. Rather, one must only lock the local RF oscillators used by Alice and Bob, which is much easier. Furthermore, information encoded in sidebands in unaffected by birefringence in the optical fiber used for transmission. Recent improvements to these experiments have included dispersion compensation and long-distance synchronization of the sender and receiver [CPPM08].

The architecture reported in [MMG+99b, MMGR99, MMG+99a] was dedicated to QKD using faint laser pulses, but it is inefficient when single photons are used because weak modulation amplitudes are required. To overcome this limitation, an alternative method was proposed in [BMMP07] in which information is encoded in both the amplitude and relative phase of three frequency bands generated by EOPMs. This second approach is attractive because in principle the EOPMs need not attenuate the signal, because there is no need for a strong reference pulse and because the EOPMs can address many frequency sidebands simultaneously. We will describe QKD applications of the method in section 3.3.

In this chapter, we introduce our method to manipulate energy-time entangled photons. First, we describe classical and single-photon schemes for manipulating the frequency degree of freedom with EOPMs, which create frequency sidebands. These experiments can be viewed as high-dimensional frequency analogues of the spatio-temporal and polarization experiments presented in section 1.3. Correspondence principles imply that classical interference translates to single-photon interference, and single-photon interference translates to two-photon interference. We show how we can transpose the setup to the entangled-photon case, leading to the notion of *frequency-bin entanglement*. We also show how the high-dimensional interference pattern created by EOPMs can be restricted to interference between effective two-dimensional states. We describe in detail our experimental tools —mainly composed of off-the-shelf components— to implement the method and acquire reliable data. Finally, we present our experimental results, i.e. high-visibility two-photon interference patterns in optical fibers at telecommunication wavelengths, demonstrating that the method can be reliably implemented.

2.1 Phase modulation

Optical nonlinearities give rise to a number of phenomena which modify the frequencies of the light fields involved in the process, such as the well-known second-harmonic generation, or parametric down-conversion [Boy03, Agr07]. Light fields can also interact with the network oscillations created by an acoustic wave: the *acousto-optic effect* corresponds to photon–phonon interactions. Annihilation of a photon at frequency ω_0 and a phonon at frequency Ω creates a photon at frequency $\omega_0 + \Omega$, and annihilation of a photon at frequency $\omega_0 + \Omega$ creates a phonon at frequency Ω and a photon at frequency ω_0. Such an effect can be used to create frequency sidebands, but the frequencies of acoustic waves are typically limited to hundreds of MHz. As we shall see, the electro-optic effect can lead to a high number of frequency sidebands separated by a radio-frequency of several GHz. We consider a medium with $\chi^{(2)}$ nonlinear susceptibility, such as lithium niobate ($LiNbO_3$). When an electric field is applied, the *linear electro-optic effect* can be interpreted as a modulation of the refractive index of the medium by the field. It leads to the modulation of the phase of the optical wave traveling across the medium.

Figure 2.1 represents the experimental configuration considered in this section. We consider a source of light $\int \mathrm{d}\omega\, f(\omega-\omega_0)\,\mathcal{E}(\omega)$, with $f(\omega-\omega_0)$ dropping rapidly to zero for $|\omega-\omega_0| > \Omega_S$. Such a quasi-monochromatic beam can be obtained by using a long-coherence laser or by passing the light of a broadband source through a narrow-band frequency filter, as schematized in figure 2.1. As will be seen in the quantum case, the exact frequency of a photon is not relevant; if it is selected by a frequency filter of bandwidth Ω_F aligned on the frequency ω_0, we say it belongs to the frequency bin centered on ω_0. Here we will thus approximate the classical wave of bandwidth $\Omega_S < \Omega_F$ as a stationary wave $A\,\mathrm{e}^{-\mathrm{i}\omega_0 t}$.

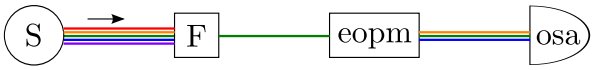

Figure 2.1: Experimental setup for phase modulation of classical light. A light beam emitted by source S is spectrally filtered by frequency filter F. The monochromatic light is sent through an electro-optic phase modulator EOPM, generating new frequencies, resolved with an optical spectrum analyzer OSA.

We consider an RF signal

$$V(t) = v\, f(\gamma - \Omega t)\,, \tag{2.1}$$

where f is a periodic function of time: $f(t+T) = f(t+2\pi/\Omega) = f(t)$. The quantities v, γ and Ω are thus the amplitude, phase and (angular) frequency —see appendix A— of the RF signal, respectively. For the GHz radio-frequencies we work with, sine modulation is by far the easiest to implement experimentally. The sine modulating signal $V(t) = v\,\sin(\gamma-\Omega t)$ imposes an optical phase variation $\varphi(t) = c\,\sin(\gamma-\Omega t)$. The normalized amplitude c is linked to the voltage v applied to the modulator by the relation

$$c = \frac{\pi\, v}{V_\pi}\,, \tag{2.2}$$

by definition of the half-wave voltage V_π characterizing the response of the modulator at the radio-frequency considered, which depends on material and geometry. The coefficients

$$U_n(c,\gamma) = J_n(c)\mathrm{e}^{\mathrm{i}n\gamma}\,, \tag{2.3}$$

where J_n is the nth-order Bessel function of the first kind, are the Fourier components of the periodic function $f(t) = \mathrm{e}^{\mathrm{i}\varphi(t)} = \mathrm{e}^{\mathrm{i}c\sin(\gamma-\Omega t)}$, so that

$$\mathrm{e}^{\mathrm{i}\varphi(t)} \equiv \mathrm{e}^{\mathrm{i}c\sin(\gamma-\Omega t)} = \sum_{n=-\infty}^{+\infty} J_n(c)\,\mathrm{e}^{\mathrm{i}n(\gamma-\Omega t)}\,. \tag{2.4}$$

This expression is the Jacobi–Anger expansion [CPV+08]. After phase modulation, the wave $A\,\mathrm{e}^{-\mathrm{i}\omega_0 t}$ is thus transformed according to

$$A\,\mathrm{e}^{-\mathrm{i}\omega_0 t}\,\mathrm{e}^{\mathrm{i}\varphi(t)} = A\sum_{n=-\infty}^{+\infty} J_n(c)\,\mathrm{e}^{\mathrm{i}n\gamma}\,\mathrm{e}^{-\mathrm{i}(\omega_0+n\Omega)t}\,. \tag{2.5}$$

Figure 2.2 shows the effects of such a modulation when used in the setup of figure 2.1. *Frequency sidebands* appear at integer multiples of the radio-frequency Ω in the spectrum of a phase-modulated optical wave. To resolve the sidebands, the bandwidth of the source has to be narrow enough: $\Omega_S < \Omega_F$. The relative heights of the peaks are given by $|J_n(c)|^2$. We note that these developments constitute well-known facts in frequency modulation, where the coefficient (2.2) is known as the *modulation index*, or *modulation depth*.

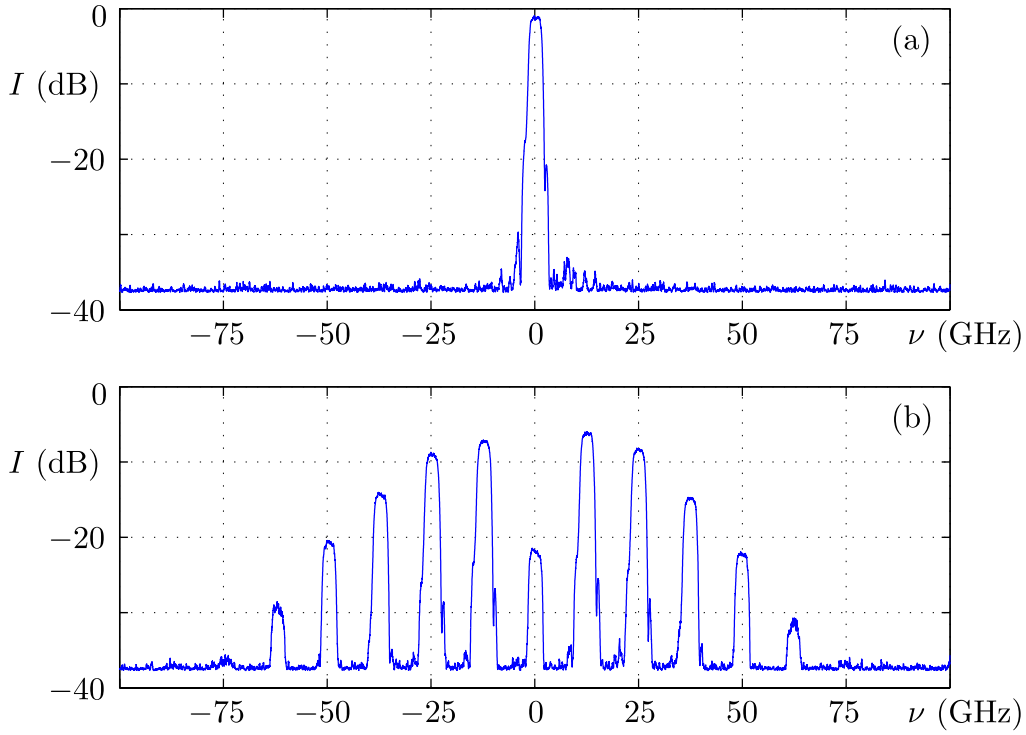

Figure 2.2: Measurement results of phase modulation of classical light, obtained with the setup of figure 2.1. Panel (a) shows the quasi-monochromatic intensity spectrum of a broadband light source passed through a narrowband frequency filter, in this case a fiber Bragg grating preceded by a circulator. Frequency "0" corresponds here to a wavelength of 1547.73 nm. Panel (b) shows the spectrum affected by phase modulation with a sine modulating signal of frequency $\Omega/2\pi = 12.5$ GHz and normalized amplitude $c \approx 2.74$, the maximal value attained with the radio-frequency setup used for the measurement. Eleven frequency bins are present.

The nth frequency sideband carries a relative phase $n\gamma$ imposed by the RF phase γ. When two EOPMs operated at the same frequency Ω are cascaded, an interference occurs. With $\varphi_{\mathrm{A}}(t) = a\sin(\alpha - \Omega t)$ and $\varphi_{\mathrm{B}}(t) = b\sin(\beta - \Omega t)$ the periodic phases imposed by each modulator, and using (2.4), we obtain:

$$A\,\mathrm{e}^{-\mathrm{i}\omega_0 t}\,\mathrm{e}^{\mathrm{i}\varphi_{\mathrm{A}}(t)}\,\mathrm{e}^{\mathrm{i}\varphi_{\mathrm{B}}(t)} = A\sum_p J_p(a)\mathrm{e}^{\mathrm{i}p\alpha}\sum_q J_q(b)\mathrm{e}^{\mathrm{i}q\beta}\mathrm{e}^{-\mathrm{i}(p+q)\Omega t}\mathrm{e}^{-\mathrm{i}\omega_0 t} \tag{2.6}$$

$$= A\sum_d\sum_p J_p(a)J_{d-p}(b)\,\mathrm{e}^{\mathrm{i}p\alpha}\,\mathrm{e}^{\mathrm{i}(d-p)\beta}\,\mathrm{e}^{-\mathrm{i}d\Omega t}\,\mathrm{e}^{-\mathrm{i}\omega_0 t} \tag{2.7}$$

$$\equiv A\sum_d c_d(a,\alpha;b,\beta)\,\mathrm{e}^{-\mathrm{i}(\omega_0+d\Omega)t}\,. \tag{2.8}$$

As shown in [Woo10, OMW+12], one can derive a simpler analytic expression for the parameter

$$c_d(a,\alpha;b,\beta) = \sum_p U_p(a,\alpha)U_{d-p}(b,\beta) = \sum_p J_p(a)J_{d-p}(b)\,\mathrm{e}^{\mathrm{i}p\alpha}\,\mathrm{e}^{\mathrm{i}(d-p)\beta}\,. \tag{2.9}$$

We start with the definition

$$J_n(c) = \frac{1}{2\pi}\int_{-\pi}^{\pi}\mathrm{d}\theta\,\mathrm{e}^{\mathrm{i}c\sin\theta}\mathrm{e}^{-\mathrm{i}n\theta} \tag{2.10}$$

to rewrite

$$c_d(a,\alpha;b,\beta) = \frac{1}{(2\pi)^2}\int_{-\pi}^{\pi}\mathrm{d}\theta'\int_{-\pi}^{\pi}\mathrm{d}\theta''\,\mathrm{e}^{\mathrm{i}a\sin\theta'}\mathrm{e}^{\mathrm{i}b\sin\theta''}\sum_p \mathrm{e}^{\mathrm{i}p(\alpha-\beta+\theta''-\theta')}\mathrm{e}^{-\mathrm{i}d(\theta''-\beta)}\,. \tag{2.11}$$

Using the fact that $\sum_p \mathrm{e}^{\mathrm{i}p\theta} = 2\pi \sum_n \delta(\theta - 2\pi n)$, thus

$$\sum_p \mathrm{e}^{\mathrm{i}p(\alpha-\beta+\theta''-\theta')} = 2\pi \sum_n \delta(\alpha - \beta + \theta'' - \theta' - 2\pi n)\,, \tag{2.12}$$

we get

$$c_d(a,\alpha,;b,\beta) = \frac{1}{2\pi}\int_{-\pi}^{\pi} \mathrm{d}\theta\, \mathrm{e}^{\mathrm{i}a\sin(\theta+\alpha)}\mathrm{e}^{\mathrm{i}b\sin(\theta+\beta)}\mathrm{e}^{-\mathrm{i}d\theta}\,. \tag{2.13}$$

Since adding two sine waves with the same period yields another sine wave, we can write

$$a\sin(\theta+\alpha) + b\sin(\theta+\beta) = C\sin(\theta+\Gamma)\,, \tag{2.14}$$

with, using basic trigonometric relations,

$$C^2 = a^2 + b^2 + 2ab\cos(\alpha-\beta) \quad \text{and} \quad \tan\Gamma = \frac{a\sin\alpha + b\sin\beta}{a\cos\alpha + b\cos\beta}\,. \tag{2.15}$$

This thus implies that

$$\begin{aligned} c_d(a,\alpha;b,\beta) &= \frac{1}{2\pi}\int_{-\pi}^{\pi} \mathrm{d}\theta\, \mathrm{e}^{\mathrm{i}C\sin(\theta+\Gamma)}\mathrm{e}^{-\mathrm{i}d\theta} && (2.16)\\ &= \frac{1}{2\pi}\int_{-\pi}^{\pi} \mathrm{d}\theta\, \mathrm{e}^{\mathrm{i}C\sin\theta}\mathrm{e}^{-\mathrm{i}d\theta}\mathrm{e}^{\mathrm{i}d\Gamma} && (2.17)\\ &= J_d(C)\,\mathrm{e}^{\mathrm{i}d\Gamma} && (2.18)\\ &= U_d(C,\Gamma)\,. && (2.19) \end{aligned}$$

This is equivalent to the *Graf addition formula* [AS72]. Intuitively, this express that two EOPMs used in series, driven by sinusoidal RF signals of the same frequency, have the same action as a single EOPM.

If $N_{d=0}^{(\mathrm{class})}\big(a=b=0;n\big)$ is the optical power in frequency bin n when the modulation is off, when modulation is on the optical power $N_d^{(\mathrm{class})}$ measured in bin $n+d$ (shifted of d times the radio-frequency Ω) is:

$$N_d^{(\mathrm{class})}\big(a,\alpha;b,\beta;n\big) = J_d^2\big([a^2+b^2+2ab\cos(\alpha-\beta)]^{1/2}\big) \times N_{d=0}^{(\mathrm{class})}\big(a=b=0;n\big)\,. \tag{2.20}$$

Note that the total power is conserved. Figure 2.3 schematically represents the consecutive phase modulations of a classical light beam.

2.2 Single-photon interference

Figure 2.4 illustrates the equivalent situation with a single-photon source. Using the correspondence principle, we expect the EOPMs to act on photon probability amplitudes the same way they act on complex fields in coherent optics. Indeed, let consider a (quantum) optical wave at frequency ω_0 propagating in a modulator subject to a (classical) sine electric signal at frequency Ω. Possible interactions are the annihilation of a radio-frequency photon at frequency Ω and a photon at frequency $\omega_0 + n\Omega$, which creates a photon at frequency $\omega_0 + (n+1)\Omega$, and the annihilation of a photon at frequency $\omega_0 + (n+1)\Omega$, which creates a radio-frequency photon at frequency Ω and a photon at frequency $\omega_0 + n\Omega$. Rigorous treatment of the quantum electro-optic effect can be found in [YY84]. Complementary studies of the manipulation of photons in the frequency domain using EOPMs can be found in [Blo06, CFP10, CFP11].

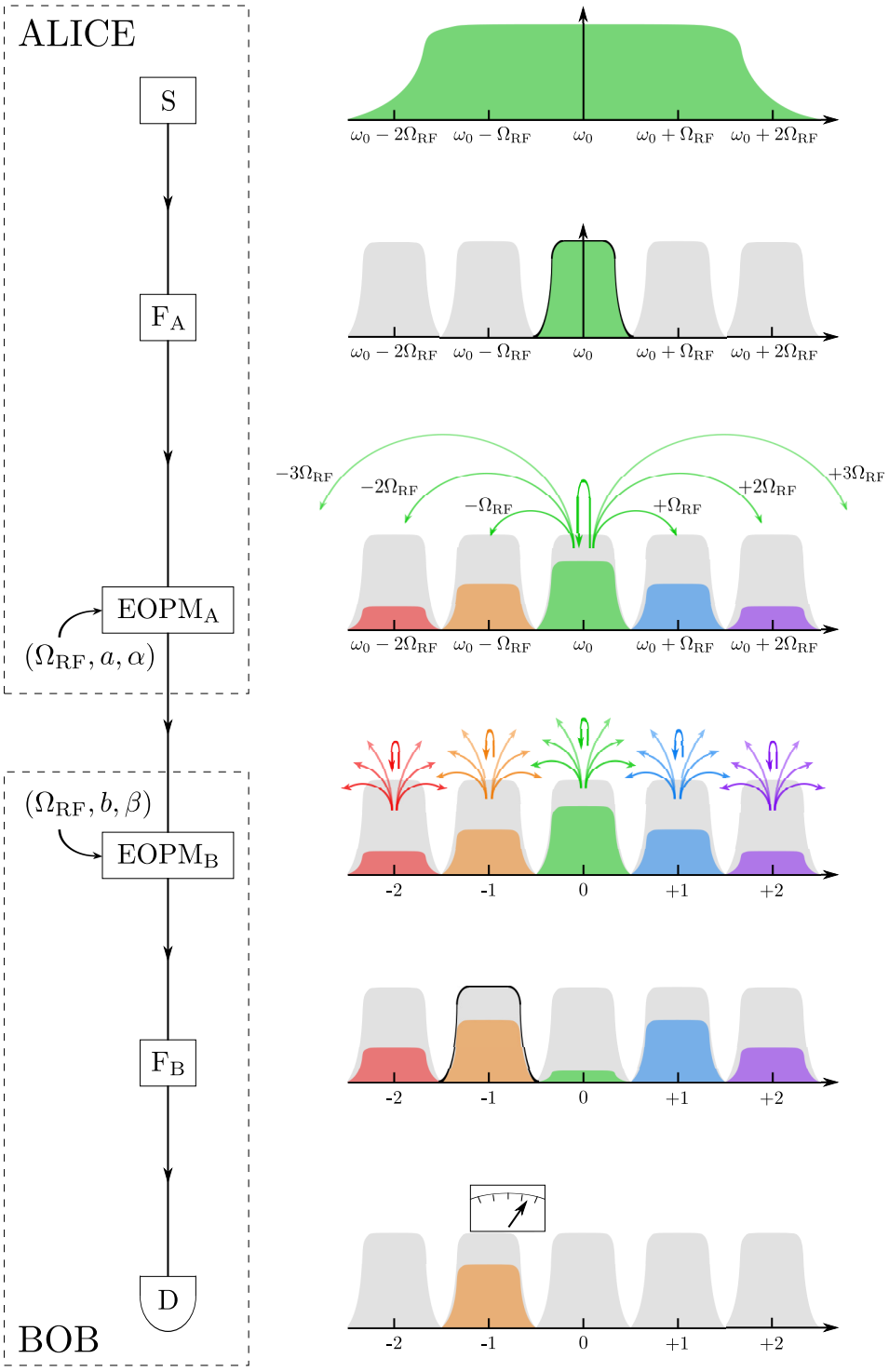

Figure 2.3: Classical interference in the frequency domain. The light emitted by a broadband source S is sent through a narrow-band frequency filter F_A of center frequency ω_0. The emerging beam, centered on frequency ω_0, is subsequently directed through electro-optic phase modulators $EOPM_A$ and $EOPM_B$, controlled by Alice and Bob respectively, each of which generates frequency shifts of integer multiples of the RF signal frequency Ω_{RF}. Frequency filter F_B and photodetector D allow Bob to investigate the intensity of the resulting light beam in different frequency bins.

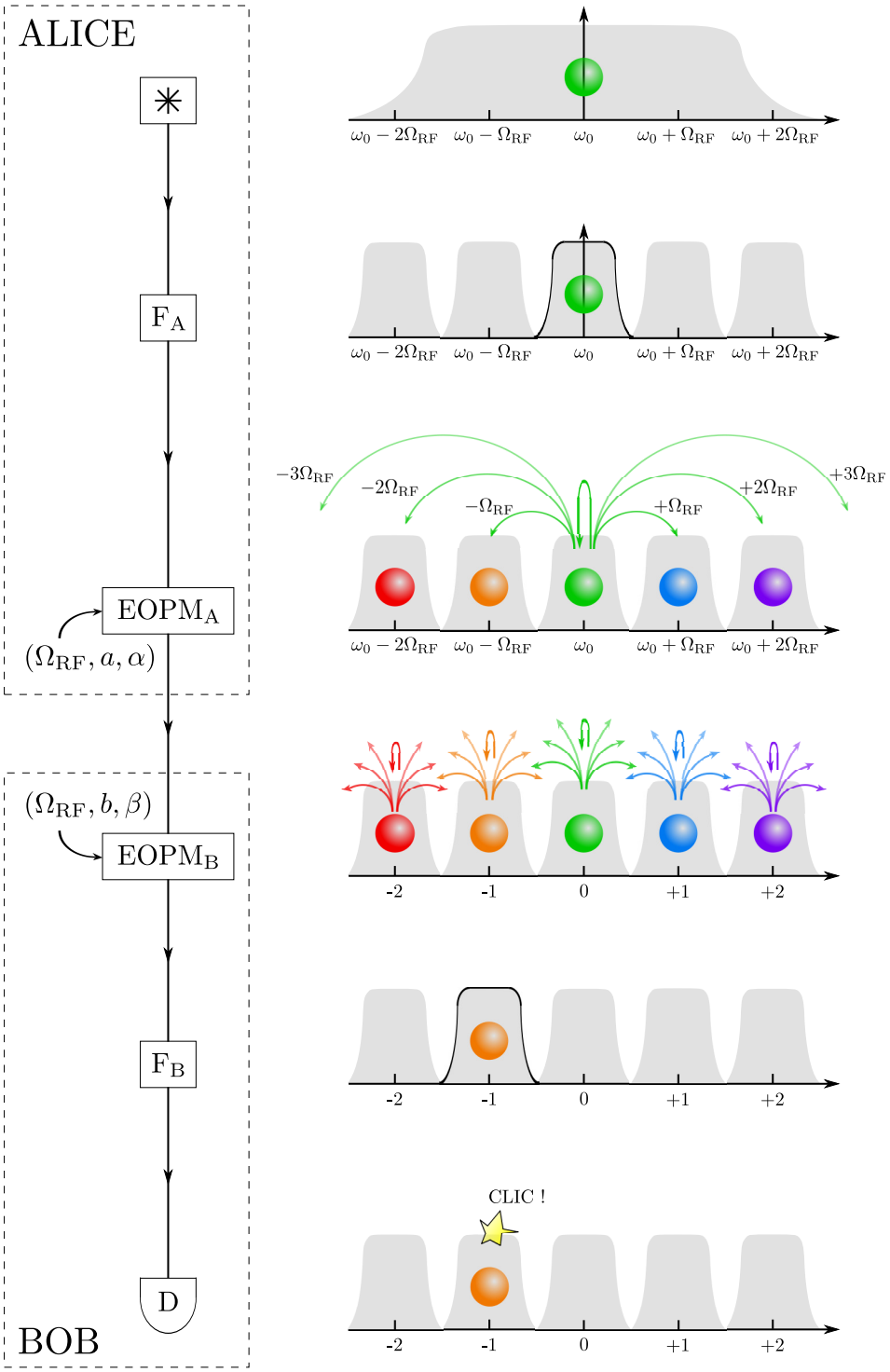

Figure 2.4: Single-photon interference in the frequency domain. Photons with frequencies in the vicinity of ω_0 are prepared by sending the photons emitted by a single-photon source through a narrow-band frequency filter F_A of center frequency ω_0. The emerging photons are subsequently directed through $EOPM_A$ and $EOPM_B$, controlled by Alice and Bob respectively, each of which generates frequency shifts of integer multiples of the RF signal frequency Ω_{RF}. Frequency filter F_B and photodiode D allow Bob to investigate the arrival rate of photons in different frequency bins.

As in the classical case, a real source generates non-stationary quantum states of the form $|\psi\rangle = \int_\omega \xi(\omega-\omega_0)a^\dagger_\omega|0\rangle$ and $|\phi\rangle = \int_\omega \xi(\omega-\omega_1)a^\dagger_\omega|0\rangle$, where $a^\dagger_\omega$ is the creation operator in the pulsation mode ω and $\xi(\omega)$ represents the spectral profile [Blo06]. These two states are in general not orthogonal, $\langle\psi|\phi\rangle \neq 0$. Nevertheless, for sufficiently peaked spectrum profiles, $\langle\psi|\phi\rangle \approx 0$. We make the assumption that we deal with perfectly monochromatic modes. We introduce the notation $|\omega_0\rangle$, which represents a single photon at frequency ω_0. This state is perfectly orthogonal to states $|\omega \neq \omega_0\rangle$.

Following (2.4), a photon at frequency ω_0 passing through an EOPM driven by a sine RF signal undergoes the unitary transformation

$$\hat{U}(c,\gamma)\,|\omega_0\rangle = \sum_{n=-\infty}^{+\infty} U_n(c,\gamma)|\omega_0+n\Omega\rangle \quad \text{with} \quad U_n(c,\gamma) = J_n(c)\mathrm{e}^{\mathrm{i}n\gamma}\,. \tag{2.21}$$

We adopt the discretized notation $|\omega_0+n\Omega\rangle \equiv |n\rangle$:

$$\hat{U}(c,\gamma)|0\rangle = \sum_{n=-\infty}^{+\infty} U_n(c,\gamma)|n\rangle \quad \text{with} \quad U_n(c,\gamma) = J_n(c)\mathrm{e}^{\mathrm{i}n\gamma}\,, \tag{2.22}$$

which remains valid for a non-perfectly monochromatic source if its spectral profile is peaked enough on ω_0, as will be analyzed in the entangled-photon case. After phase modulation, the probability to detect the photon in frequency bin n is $|J_n(c)|^2$. If one does not make a measurement of the photon frequency, the photon is in a quantum superposition in the frequency domain.

If the photon is subject to consecutive phase modulations $\varphi_\mathrm{A}(t) = a\sin(\alpha-\Omega t)$ and $\varphi_\mathrm{B}(t) = b\sin(\beta-\Omega t)$, we readily find:

$$\begin{aligned}
\hat{U}(b,\beta)\,\hat{U}(a,\alpha)\,|0\rangle &= \sum_p J_p(a)\mathrm{e}^{\mathrm{i}p\alpha}\sum_q J_q(b)\mathrm{e}^{\mathrm{i}q\beta}|p+q\rangle &(2.23)\\
&= \sum_d\sum_p J_p(a)J_{d-p}(b)\mathrm{e}^{\mathrm{i}p\alpha}\mathrm{e}^{\mathrm{i}(d-p)\beta}|d\rangle &(2.24)\\
&\equiv \sum_d c_d(a,\alpha;b,\beta)|d\rangle\,. &(2.25)
\end{aligned}$$

We recover the same coefficients as in the classical case:

$$c_d(a,\alpha;b,\beta) = \sum_p U_p(a,\alpha)U_{d-p}(b,\beta) = U_d(C,\Gamma) = J_d(C)\mathrm{e}^{\mathrm{i}d\Gamma}\,. \tag{2.26}$$

The photon therefore exhibits single-photon interferences in the frequency domain. This is due to the fact that one cannot distinguish between the different "frequency paths" the photon could have followed before being detected in frequency bin $n+d$. Since there are more than two paths, we do not recover the traditional sine-squared interference pattern, but rather a Bessel pattern originating from the sine modulating signal. The rate of photons detected in frequency bin $n+d$ will thus be:

$$N^{(1)}_d\big(a,\alpha;b,\beta;n\big) = J^2_d\big([a^2+b^2+2ab\cos(\alpha-\beta)]^{1/2}\big)\times N^{(1)}_{d=0}\big(a=b=0;n\big)\,, \tag{2.27}$$

where $N^{(1)}_{d=0}\big(a=b=0;n\big)$ is the photon rate for frequency bin n when the modulation is off.

2.3 Two-photon interference

We now consider two-photon experiments which will exhibit nonlocal two-photon interferences in the frequency domain, see figure 2.5. These experiments are based on three components. Our description follows references [OCN+10], [OMW+12] and [OWPH+14].

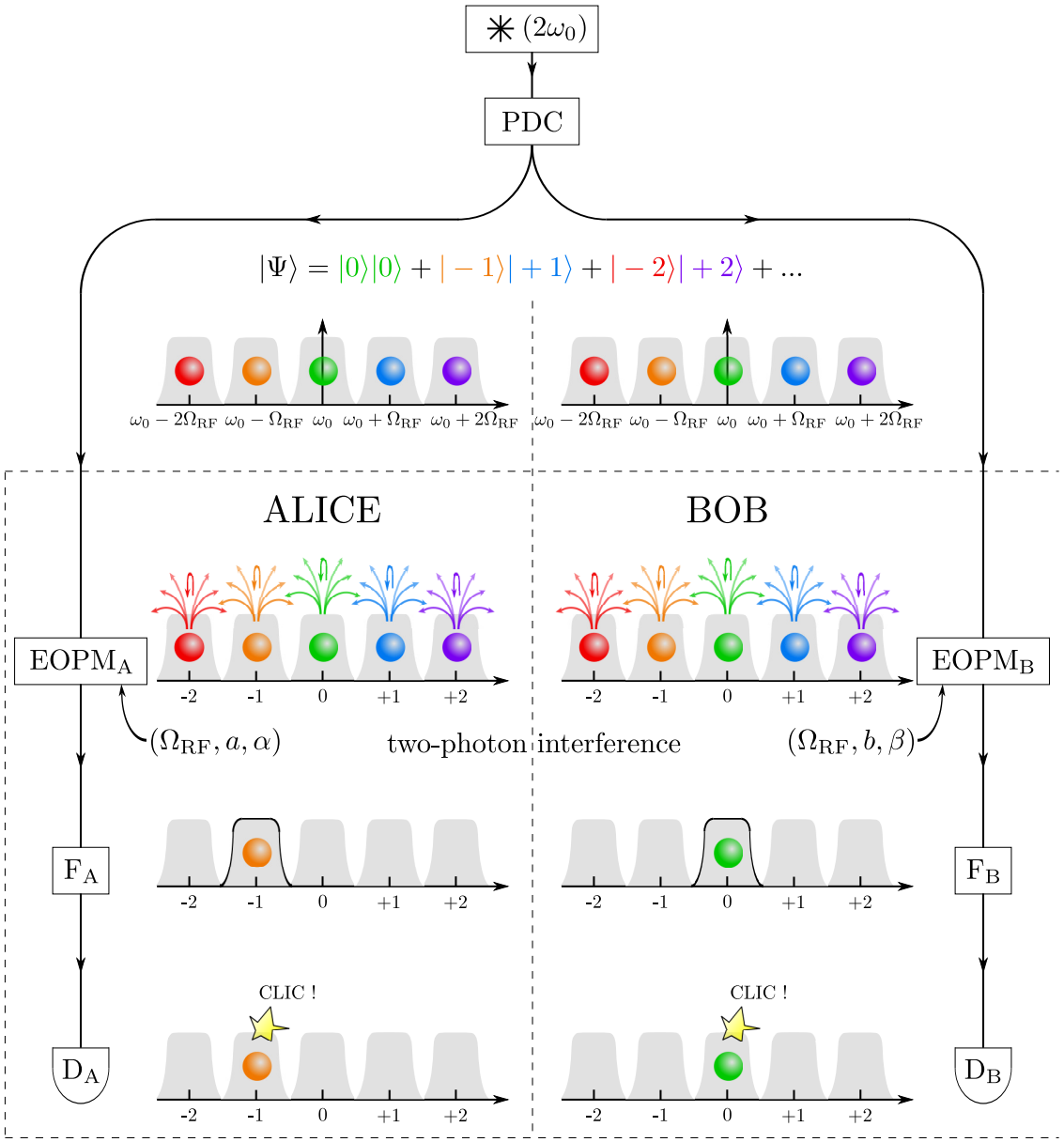

Figure 2.5: Two-photon interference in the frequency domain. A narrow-band laser of frequency $2\omega_0$ pumps a parametric down-converter PDC and generates entangled photon pairs. One photon in each entangled pair is sent to Alice, who sends her photon through EOPM$_A$ which generates frequency shifts. Frequency filter F$_A$ and photodiode D$_A$ allow Alice to detect photons arriving in different frequency bins. Bob similarly manipulates and detects the second photon using EOPM$_B$, filter F$_B$, and his own photodiode D$_B$. The joint two-photon statistics exhibit nonlocal interference.

First, a parametric down-conversion source S produces the frequency-entangled state

$$|\Psi\rangle = \int \mathrm{d}\omega f(\omega)|\omega_0+\omega\rangle|\omega_0-\omega\rangle \simeq \int \mathrm{d}\omega|\omega_0+\omega\rangle|\omega_0-\omega\rangle\,. \tag{2.28}$$

The energy of each photon is uncertain, while the total energy is fixed by $2\omega_0$, the frequency of the supposedly perfectly monochromatic laser pumping the $\chi^{(2)}$ nonlinear waveguide. If one measures the frequencies of Alice and Bob's photons, one finds perfect correlations: if Alice obtains $\omega_0+\omega$, Bob obtains $\omega_0-\omega$. Considering the finite linewidth of the pump laser would

make the pump frequency $2\omega_0$ slightly uncertain. The complex function $f(\omega) = r(\omega)e^{i\phi(\omega)}$ characterizes the bandwidth of the signal and idler photons. Because f varies slowly with frequency, for the theoretical analysis is is often useful to approximate it as constant, thus neglecting the finite bandwidth of the photon pairs. Note that taking the Fourier transform of (2.28) would yield a description of the state in terms of time entanglement: the arrival time of each photon is uncertain, but the difference between the arrival time of Alice's and Bob's photons is well defined.

Second, an EOPM driven by a radio-frequency signal $v\sin(\gamma - \Omega t)$ with adjustable amplitude v and phase γ realizes the unitary transformation (2.21)

$$|\omega\rangle \mapsto \sum_{n\in\mathbb{Z}} J_n(c)e^{in\gamma}|\omega + n\Omega\rangle\,. \tag{2.29}$$

Alice's and Bob's photons are independently modulated with adjustable parameters (a, α) and (b, β), respectively.

Third, frequency filters in front of single-photon detectors realize projections

$$\Pi_F = \int d\omega\, g(\omega)\Pi_{\omega_0+n\Omega+\omega}\,, \tag{2.30}$$

with $\Pi_\omega = |\omega\rangle\langle\omega|$ the projector onto the frequency state ω, and $g(\omega)$ is a function characteristic of the frequency filter. In practice the frequency can only be measured with precision Ω_F given by the width of the frequency filter used. This leads to the notion of frequency bin: all photons whose frequencies are contained in the interval $[\omega_F - \Omega_F/2, \omega_F + \Omega_F/2]$ are grouped into a single frequency bin centered on frequency $\omega_F = \omega_0 + n\Omega$. To resolve the frequency bins separated by the radio-frequency Ω, the function $g(\omega)$ describing the frequency filter must thus tend to zero for $|\omega| \geq \Omega/2$, i.e. Ω_F must be less than Ω.

To analyze these experiments, we begin with the state (2.28). Because the EOPMs only shift the frequency by integer multiples of Ω and the frequency filters are aligned on the frequencies $\omega_0 + n\Omega$, it is convenient to rewrite the state as

$$\begin{aligned}
|\Psi\rangle &= \int_{-\Omega/2}^{+\Omega/2} d\omega \sum_{n=-\infty}^{+\infty} f(n\Omega+\omega)|\omega_0 + n\Omega + \omega\rangle|\omega_0 - n\Omega - \omega\rangle && (2.31)\\
&\simeq \int_{-\Omega/2}^{+\Omega/2} d\omega \sum_{n=-\infty}^{+\infty} f_n|n,\omega\rangle|-n,-\omega\rangle && (2.32)\\
&= \sum_{n=-\infty}^{+\infty} f_n|n\rangle|-n\rangle \otimes \int_{-\Omega/2}^{+\Omega/2} d\omega|\omega\rangle|-\omega\rangle && (2.33)\\
&= |\Psi_\Pi\rangle \otimes |\Psi_{\text{off}}\rangle\,. && (2.34)
\end{aligned}$$

In (2.32), f is assumed to vary slowly, so that its dependence on ω can be neglected: $f(n\Omega + \omega) \simeq f_n$. The identification $|n\rangle \otimes |\omega\rangle = |n,\omega\rangle = |\omega_0 + n\Omega + \omega\rangle$ defines a factorization $\mathcal{H}_F = \mathcal{H}_\Pi \otimes \mathcal{H}_{\text{off}}$ of the Hilbert space $\mathcal{H}_F$ of frequency states into separate "discrete" and "offset" spaces, $\mathcal{H}_\Pi$ and $\mathcal{H}_{\text{off}}$, respectively, with respect to which the source state $|\Psi\rangle$ is (approximately) separable. We adopt the normalization

$$\langle m|n\rangle = \delta_{mn}\,, \qquad \langle\omega'|\omega\rangle = \delta(\omega' - \omega)\,. \tag{2.35}$$

In this representation, the action of an EOPM becomes

$$|n\rangle \otimes |\omega\rangle \mapsto \sum_{p\in\mathbb{Z}} J_p(c)e^{ip\gamma}|n+p\rangle \otimes |\omega\rangle = \big(U(c,\gamma) \otimes \mathbb{I}_{\text{off}}\big)|n\rangle \otimes |\omega\rangle\,, \tag{2.36}$$

with the unitary transformation $U(c,\gamma)$ acting only on $\mathcal{H}_\Pi$ and $\mathbb{1}_{\text{off}}$ is the identity in the offset space. We see explicitly that the description of the relevant part of our setup is entirely contained in the discrete space. Indeed, the offset frequency ω only affects the probability of response of the filter —whose action can also be factorized— via the factor $|g(\omega)|^2$, and is otherwise never measured or recorded in the course of the experiment. The EOPMs will cause contributions from different values of the index n to interfere, while contributions from different values of the offset parameter ω will add probabilistically: with a sufficiently precise measurement of the frequencies of the photons exiting the EOPMs, we could determine a specific value for ω. Consequently, we restrict the remainder of the theoretical analysis to the discrete space and adopt the discretized version:

$$|\Psi\rangle = \sum_{n=-\infty}^{+\infty} f_n |n\rangle|-n\rangle\,. \tag{2.37}$$

The factorization and isolation of the discrete space formalizes the concept of "frequency bin": $|n\rangle$ denotes a photon with frequency $\omega_0 + n\Omega + \omega$ for some $\omega \in \left[-\Omega/2, \Omega/2\right]$. Recall that we denote $f_n = r_n e^{i\phi_n} = f(n\Omega+\omega), \forall n$. Validity of the hypothesis that f_n varies slowly with n is justified if Ω is very small compared to the frequency range over which f varies. In our experiments the bandwidth of the photon-pair source (the scale over which f changes) is approximately 5 THz, while $\Omega/2\pi$ is 12.5 or 25 GHz.

Photons A and B are separated and sent through EOPMs with respective parameters (a,α) and (b,β). The state (2.37) is transformed according to:

$$\hat{U}(a,\alpha)\otimes\hat{U}(b,\beta)|\Psi\rangle = \sum_{n,d} f_n\, c_d(a,\alpha;b,\beta)\,|n\rangle|-n+d\rangle\,, \tag{2.38}$$

where we use the approximation $f_n \approx f_{n+p}$. This is valid for small values of p. According to Carlson's rule [CCR02], the amplitude of the generated sidebands $J_p(c)$ becomes progressively negligible for $|p| > c+1$. Given the amplitudes c experimentally accessible, we will address frequency bins $p \in \{-5,5\}$, see figure 2.2, which justifies the approximation.

The joint probability of Alice detecting a photon in the frequency bin n on which frequency filter $\mathrm{F_A}$ is aligned and Bob detecting a photon in frequency bin $-n+d$ on which frequency filter $\mathrm{F_B}$ is aligned is given by

$$P_d(a,\alpha;b,\beta;n) = \left|\langle n|\langle -n+d|\Psi\rangle\right|^2 = |f_n|^2\left|c_d(a,\alpha;b,\beta)\right|^2 = |f_n|^2 J_d^2(C)\,, \tag{2.39}$$

with the parameter C given by (2.15). It implies the normalization $\sum_d P_d(a,\alpha;b,\beta;n) = |f_n|^2$ required by conservation of probability. With modulation turned off the photons do not change frequency and the correlations are trivial: $P_{d=0}(a=b=0;n) = |f_n|^2$ and $P_{d\neq 0}(a=b=0;n) = 0$, as expected. The coincidence rate for frequency bins n and $-n+d$ will be given by

$$N_d^{(2)}(a,\alpha;b,\beta;n) = J_d^2\left([a^2+b^2+2ab\cos(\alpha-\beta)]^{1/2}\right) \times N_{d=0}^{(2)}(a=b=0;n)\,, \tag{2.40}$$

where $N_{d=0}^{(2)}(a=b=0;n)$ is the coincidence rate for frequency bins n and $-n$ when the modulation is off. Manipulating frequency-entangled photons with EOPMs gives rise to Bessel-type interference patterns, rather than the usual sine interference patterns in optics when only two modes are present. Note that single-photon rates are unaffected by the modulation: f_n being supposedly constant in the frequency range where the EOPMs act, the in- and out-couplings to and from each frequency bin are exactly compensating each other.

Rates $N^{(\text{class})}$, $N^{(1)}$ and $N^{(2)}$, given by relations (2.20), (2.27) and (2.40) respectively, exhibit the same functional dependence on $(a,\alpha;b,\beta)$. As indicated in section 1.3, there is a mathematical

correspondence between correlation experiments on maximally entangled states and prepare-and-measure schemes, based on the identity (1.46).

However, in general, these two schemes correspond to different experiments because implementing U_{B}^{T} is physically different from implementing U_{B}. This is the case, for example, in experiments involving time bins. In our setup however, where the transformations $U_{\mathrm{A,B}}$ are realized by EOPMs, $U_{\mathrm{B}}^{T} = U_{\mathrm{B}}$ (in the frequency-bin basis), in the sense that: $\langle -n|\hat{U}(a,\alpha)|p\rangle = \langle -p|\hat{U}(a,\alpha)|n\rangle$. The above mathematical identity thus translates to a physical correspondence between transition amplitudes in two-photon and single-photon experiments, with all the RF parameters (amplitudes and phases) kept unchanged.

In practice, this corresponds to the equivalence between the scheme depicted in figure 2.6, in which photons belonging to a particular frequency bin are selected by a filter and subsequently modulated with parameters (a,α) and (b,β), and figure 2.7, in which entangled photons are manipulated by EOPMs. Specifically, the amplitude of detecting photons in frequency bins $-n$ and $n+d$ in experiment 2.7 is proportional to the amplitude of detecting a photon in frequency bin $n+d$ given it was prepared in frequency bin n in experiment 2.6:

$$\begin{aligned} & \langle -n|\langle n+d|\hat{U}(a,\alpha)\otimes\hat{U}(b,\beta)|\Psi\rangle \\ = \;& \sum_{p} f_p \langle n+d|\hat{U}(b,\beta)|-p\rangle\langle -n|\hat{U}(a,\alpha)|p\rangle \\ \simeq \;& f_n \sum_{p} \langle n+d|\hat{U}(b,\beta)|-p\rangle\langle -p|\hat{U}(a,\alpha)|n\rangle \\ = \;& f_n \langle n+d|\hat{U}(b,\beta)\hat{U}(a,\alpha)|n\rangle\,, \end{aligned} \tag{2.41}$$

where in line 3 we have invoked the assumption that f_n is approximately constant over the experimentally accessible range of frequencies which interfere, and we used the completeness relation $\sum_p |p\rangle\langle p| = 1$.

Identical RF settings thus give rise to identical interference patterns both in single-photon and two-photon experiments. This identity is very useful as it makes it possible to test the quality of the RF setup using a broadband light source.

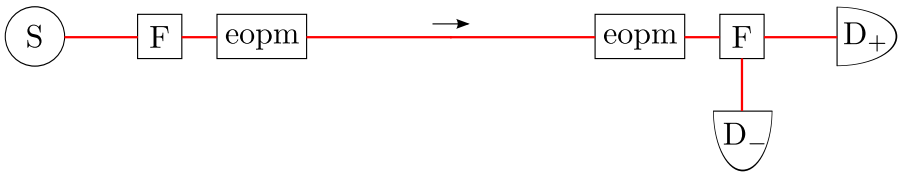

Figure 2.6: Single-photon interference in the frequency domain. A photon prepared in the frequency bin n is subsequently modulated with parameters (a,α) and (b,β), then detected in a specific frequency bin $n+d$ in detector D_+.

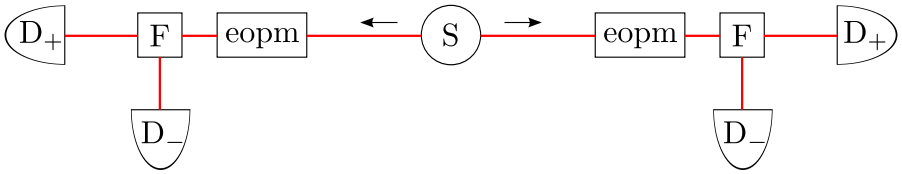

Figure 2.7: Two-photon interference in the frequency domain. A source S produces frequency-entangled photons which are separately modulated with respective parameters (a,α) and (b,β), then detected in respective frequency bins $-n$ and $n+d$ in detectors D_+.

2.4 A variation with interleavers

While the high dimensionality of the entangled state (2.28) can be beneficial, it is sometimes desirable to work with well-known two-dimensional states for which most quantum communication protocols, such as the BB84 key distribution scheme, are designed. For qubits it is also easier to collect all the outcome results, which allows to test the CHSH Bell inequality, see section 3.1. This is thus of interest for applications such as quantum cryptography or low-dimensional tests of quantum nonlocality. Here, following [OWPH$^+$14], we show how to define, manipulate, and measure effective two-dimensional states in the frequency domain.

The key idea is to use periodic frequency filters that discriminate between two sets of frequency bins, those with *even* and *odd* frequencies. This implements a coarse-grained measurement that projects onto two orthogonal subspaces. In our theoretical analysis, we show how this reduces the high-dimensional photon state to an effective two-dimensional state. The experiment consists of preparing the state (2.28), sending Alice's and Bob's photons through EOPMs driven by RF signals with identical frequency Ω but different amplitudes and phases, (a, α) and (b, β), and finally determining whether the frequency is even or odd by passing the photon through interleavers and directing the outputs to single-photon detectors.

An interleaver is a standard component used in the telecommunication industry that separates the frequencies centered on $\omega_0 + 2n\Omega$ from those centered on $\omega_0 + (2n+1)\Omega$, where ω_0 is a fixed offset, and $n \in \mathbb{Z}$. We shall use interleavers as components that allow the measurement of even and odd frequencies. If we follow the interleaver by single-photon detectors, then a click of one of the detectors corresponds to the projection onto one of the two operators:

$$\Pi_{\mathrm{E}} = \int_{-\Omega}^{+\Omega} \mathrm{d}\omega\, g(\omega) \sum_n \Pi_{\omega_0+2n\Omega+\omega}\,, \qquad \Pi_{\mathrm{O}} = \int_{-\Omega}^{+\Omega} \mathrm{d}\omega\, g(\omega) \sum_n \Pi_{\omega_0+(2n+1)\Omega+\omega}\,, \tag{2.42}$$

where $\Pi_\omega = |\omega\rangle\langle\omega|$ is the projector onto the frequency state $|\omega\rangle$ and $g(\omega)$ is a function characteristic of the interleaver which is maximal in the vicinity of $\omega = 0$ and very small when $|\omega| > \Omega/2$. Following the reasoning of section 2.3, we can factorize the projections (2.42) between discrete and offset spaces.

The effective qubits manipulated in our setup are made explicit when we express the source state $|\Psi_\Pi\rangle$ (2.31) and actions of the EOPMs (2.29) and interleavers (2.42) in the basis of *even* and *odd frequency phase states*. These states can be derived from our setup's symmetries with respect to translations of frequency bins. Formally, let us denote

$$\mathcal{T}_k : |n\rangle \mapsto |n+k\rangle \tag{2.43}$$

the (unitary, for n varying from $-\infty$ to $+\infty$) operation consisting of translation in the frequency domain by k frequency bins. The EOPM and interleaver actions are symmetric with respect to translations by k and $2k$, respectively, in the sense that

$$\big[U(c,\gamma), \mathcal{T}_k\big] = 0\,, k \in \mathbb{Z} \quad \text{and} \quad \big[\Pi_{\mathrm{E}}, \mathcal{T}_k\big] = \big[\Pi_{\mathrm{O}}, \mathcal{T}_k\big] = 0\,, k \in 2\mathbb{Z}\,. \tag{2.44}$$

As the amplitude f_n varies slowly, the source state has the approximate symmetry

$$\mathcal{T}_k \otimes \mathbb{T}_{-k} |\Psi_\Pi\rangle \simeq |\Psi_\Pi\rangle\,. \tag{2.45}$$

Consequently, the EOPMs and source will share eigenstates with the $\mathcal{T}_1$ operator, while the interleaver action eigenstates will coincide with those of $\mathcal{T}_2$.

A full set of eigenstates of the $\mathcal{T}_1$ operator is given by the frequency phase states, which we define by

$$|\varphi\rangle = \frac{1}{\sqrt{2\pi}} \sum_n \mathrm{e}^{\mathrm{i}n\varphi} |n\rangle\,, \tag{2.46}$$

such that $\mathcal{T}_k|\varphi\rangle = \mathrm{e}^{-\mathrm{i}k\varphi}|\varphi\rangle$. The inverse of this expression is given by

$$|n\rangle = \frac{1}{\sqrt{2\pi}} \int_{-\pi}^{\pi} \mathrm{d}\varphi\, \mathrm{e}^{-\mathrm{i}n\varphi}|\varphi\rangle\,. \tag{2.47}$$

For the $\mathcal{T}_2$ operator, a complete basis of eigenstates that will prove convenient is given by the even and odd frequency phase states

$$|\varphi\rangle_{\mathrm{E}} = \frac{1}{\sqrt{\pi}} \sum_{n\in 2\mathbb{Z}} \mathrm{e}^{\mathrm{i}n\varphi}|n\rangle\,, \qquad |\varphi\rangle_{\mathrm{O}} = \frac{1}{\sqrt{\pi}} \sum_{n\in 2\mathbb{Z}+1} \mathrm{e}^{\mathrm{i}n\varphi}|n\rangle\,, \tag{2.48}$$

with $\mathcal{T}_2|\varphi\rangle_{\mathrm{E}} = \mathrm{e}^{-\mathrm{i}2\varphi}|\varphi\rangle_{\mathrm{E}}$ and $\mathcal{T}_2|\varphi\rangle_{\mathrm{O}} = \mathrm{e}^{-\mathrm{i}2\varphi}|\varphi\rangle_{\mathrm{O}}$. Note that

$$|\varphi\rangle = \frac{1}{\sqrt{2}}\big[|\varphi\rangle_{\mathrm{E}} + |\varphi\rangle_{\mathrm{O}}\big] \quad \text{and} \quad |\varphi+\pi\rangle = \frac{1}{\sqrt{2}}\big[|\varphi\rangle_{\mathrm{E}} - |\varphi\rangle_{\mathrm{O}}\big]\,. \tag{2.49}$$

In terms of these states, the even and odd projection operators (restricted to the discrete space) take the form

$$\Pi_{\mathrm{E}} = \int_0^{\pi} \mathrm{d}\varphi\, |\varphi\rangle_{\mathrm{E}}\langle\varphi|_{\mathrm{E}} \quad \text{and} \quad \Pi_{\mathrm{O}} = \int_0^{\pi} \mathrm{d}\varphi\, |\varphi\rangle_{\mathrm{O}}\langle\varphi|_{\mathrm{O}}\,, \tag{2.50}$$

and the entangled source state can be rewritten as

$$|\Psi_{\Pi}\rangle \simeq \frac{1}{\sqrt{N}} \sum_n |n\rangle|-n\rangle = \frac{1}{\sqrt{N}} \int_{-\pi}^{\pi} \mathrm{d}\varphi\, |\varphi\rangle|\varphi\rangle = \frac{1}{\sqrt{N}} \int_0^{\pi} \mathrm{d}\varphi\, \big(|\varphi\rangle_{\mathrm{E}}|\varphi\rangle_{\mathrm{E}} + |\varphi\rangle_{\mathrm{O}}|\varphi\rangle_{\mathrm{O}}\big)\,, \tag{2.51}$$

where we idealize $|\Psi_{\Pi}\rangle$ as an infinite sum, and N is a normalization constant symbolically representing the number of frequency bins over which f_n is nonzero, and formally equal to $2\pi\delta(0)$, see [OCN+10] for a discussion of normalization. We observe that the photons have always the same parity. Note that, depending on the position of ω_0 with respect to even and odd frequency bins, one can also produce a state where the photons have always a different parity.

The action of an EOPM on a frequency phase state is

$$\begin{aligned} U(c,\gamma)|\varphi\rangle &= \frac{1}{\sqrt{2\pi}} \sum_m \mathrm{e}^{\mathrm{i}m\varphi} \sum_p J_p(c)\mathrm{e}^{\mathrm{i}p\gamma}|m+p\rangle && (2.52)\\ &= \sum J_p(c)\mathrm{e}^{\mathrm{i}p(\gamma-\varphi)} \frac{1}{\sqrt{2\pi}} \sum_n \mathrm{e}^{\mathrm{i}n\varphi}|n\rangle && (2.53)\\ &= \mathrm{e}^{\mathrm{i}c\sin(\gamma-\varphi)}|\varphi\rangle\,. && (2.54) \end{aligned}$$

Since $|\varphi\rangle = \big[|\varphi\rangle_{\mathrm{E}} + |\varphi\rangle_{\mathrm{O}}\big]/\sqrt{2}$ and $|\varphi+\pi\rangle = \big[|\varphi\rangle_{\mathrm{E}} - |\varphi\rangle_{\mathrm{O}}\big]/\sqrt{2}$, we find that

$$U(c,\gamma)|\varphi\rangle_{\mathrm{E}} = \cos\theta|\varphi\rangle_{\mathrm{E}} - \mathrm{i}\sin\theta|\varphi\rangle_{\mathrm{O}} \quad \text{and} \quad U(c,\gamma)|\varphi\rangle_{\mathrm{O}} = -\mathrm{i}\sin\theta|\varphi\rangle_{\mathrm{E}} + \cos\theta|\varphi\rangle_{\mathrm{O}}\,, \tag{2.55}$$

where we have set $\theta = c\sin(\gamma-\varphi)$. For a fixed phase φ, by varying the modulation parameters c and γ, we can implement a σ_x rotation of any desired angle between the even and odd frequency phase states.

The construction of [OWPH+14] thus shows how to define effective qubits $\big\{|\varphi\rangle_{\mathrm{E}}, |\varphi\rangle_{\mathrm{O}}\big\}$ in the frequency domain, and how EOPMs realize σ_x rotations on the effective qubits. However, the angle of the rotation depends on the phase φ of the effective qubit. This phase is not experimentally accessible. Since the entangled state (2.51) is given by an integral over φ, this will imply a modified interference pattern with reduced visibility. Transforming the source state with EOPMs of modulation parameters (a,α) and (b,β), we calculate the probability of jointly detecting two photons in even or odd frequency bins [Woo10, OWPH+14]:

$$P(\mathrm{E},\mathrm{E}) = P(\mathrm{O},\mathrm{O}) = \frac{1}{4}\big[1+J_0(2C)\big] \quad \text{and} \quad P(\mathrm{E},\mathrm{O}) = P(\mathrm{O},\mathrm{E}) = \frac{1}{4}\big[1-J_0(2C)\big]\,, \tag{2.56}$$

with C defined by (2.15). Note that $P(\mathrm{E},\mathrm{E})$ and $P(\mathrm{O},\mathrm{O})$ never vanish, whereas $P(\mathrm{E},\mathrm{O})$ and $P(\mathrm{O},\mathrm{E})$ vanish whenever $C = 0$, which occurs whenever $a = b$ and $\alpha - \beta = \pi$, as in this case $J^2_{d=0}(C) = 1$. Because of the average over φ, the interference pattern differs from the traditional sine-squared function.

2.5 Experimental implementation

Figure 2.8 depicts the implementation of the setup of figure 2.7, based on functional "blocks". First, a source S produces the frequency-entangled state (2.28), with ω_0 in the telecommunication C-band. Second, EOPMs driven by RF signals with identical frequency Ω but different amplitudes and phases, (a, α) and (b, β), realize interference in the frequency domain. Third, filters select given (sets of) frequency bins. Fourth, the joint statistics of the single-photon detectors is acquired with a data acquisition system.

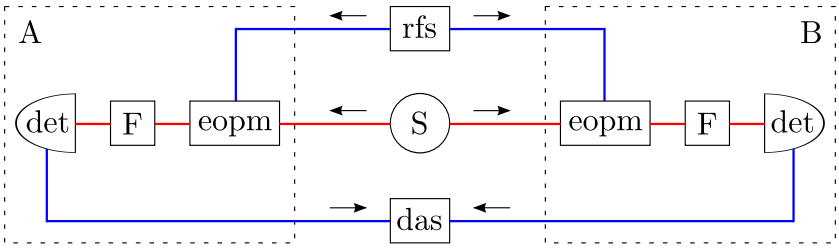

Figure 2.8: Schematic representation of a generic experimental setup. A source S produces frequency-entangled photons. The two photons are sent into separate optical fibers (in red). Each goes through an electro-optic phase modulator EOPM. Alice's and Bob's modulation parameters can be independently set with a dedicated radio-frequency system RFS connected to the EOPMs with electronic cables (in blue). The photons belonging to specific (sets of) frequency bins are detected with single-photon detectors following frequency filters F. The electronic signals of the detectors are sent to a data acquisition system DAS which registers the relative detection times and outputs a histogram of these events.

In the following subsections, we describe our experimental methods for generating, manipulating, filtering and detecting frequency-bin entangled photons. Our experimental implementations all use commercially available fiber-pigtailed and electro-optic components, and operate in the telecommunication C-band. In order to produce high-visibility interference patterns, our architecture must fulfill some critical requirements that we describe through the evolution of our experimental setups.

2.5.1 Generation

Our photon-pair source is schematized in figure 2.9. A fiber-coupled continuous-wave laser (from SACHER LASERTECHNIK) pumps a periodically-poled lithium niobate (PPLN) waveguide (from HC PHOTONICS). The wavelength of the laser can be tuned around 775 nm by manually adjusting the external cavity of the diode, and more finely by controlling the temperature, the driving current, or the voltage of a piezo-electric element acting on the cavity. The linewidth of the laser is about 2 MHz, which is far less than the bandwidth of the filters and the radio-frequency used —a few GHz.

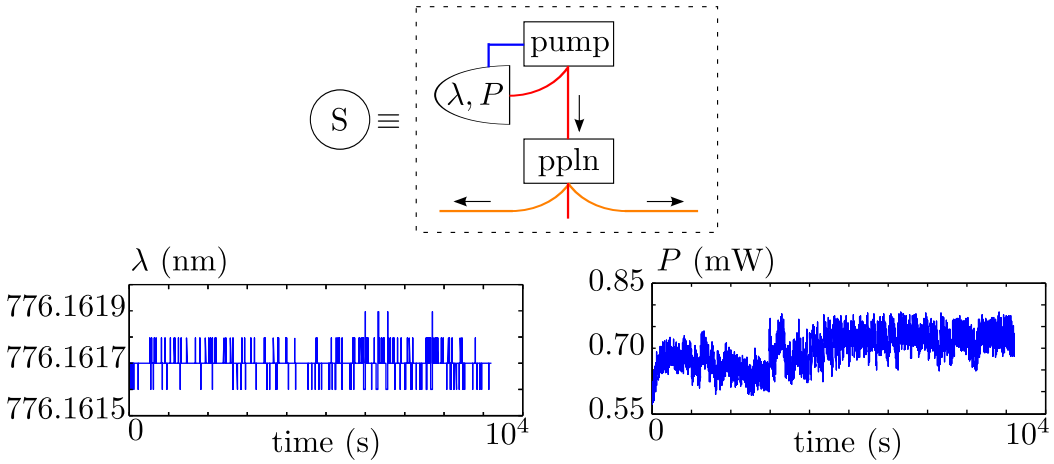

Figure 2.9: Detail of the photon-pair source. A continuous-wave PUMP laser at frequency $2\omega_0$ is injected in a periodically-poled lithium niobate waveguide PPLN, generating by parametric down-conversion signal and idler photons at frequencies $\omega_0 \pm \omega$. The remaining pump power is eliminated and the photons are separated with fiber components. A part of the pump power is directed to a wavelength-meter and a power-meter to measure its wavelength λ and power P. A retroaction controlling the piezo-electric element acting on the external cavity of the laser locks the wavelength on a desired value, 776.1617 nm in this case. No power stabilization is performed. Typical time evolution of wavelength λ and power P of the pump laser are shown.

In order to achieve a high and stable SNR, fine control of the pump laser wavelength is compulsory. Each down-converted photon must belong to a frequency bin whose width is set by the band-pass filters, of the order of a few GHz. The pump wavelength must thus be accurately set at the center of a frequency bin. To this end, we implemented an active stabilization, based first on an analogic system, and then on a numeric system: 10% of the power of the pump laser is sent to a wavelength meter (EXFO) that compares the measured wavelength and a reference. A proportional-integral-derivative loop generates an error signal which feeds the piezoelectric transducer of the external cavity of the laser, stabilizing the wavelength of the laser with an absolute precision of ± 0.2 pm, see figure 2.9. The degeneracy frequency ω_0 of the photon pairs is thus controlled with a precision of about ± 0.04 GHz. Measurements of the wavelength and power of the laser are stored and treated by a MATLAB routine.

In the $\chi^{(2)}$ medium, the pump photons at frequency $2\omega_0$ can split into signal and idler photons at frequencies $\omega_{s,i} = \omega_0 \pm \omega$. We measured a photon-pair spectrum extending on the whole C-band. The process is made efficient by engineering the *quasi phase matching* technique in the periodically-poled waveguide, achieved by carefully controlling the waveguide's temperature. Its optimization can be based on measurements in the second-harmonic regime. To achieve a fine conversion wavelength control and good efficiency, the PPLN crystal is placed in an oven or on a Peltier cell for accurate temperature stability. It is then possible to efficiently generate frequency-entangled photon pairs centered at a specific frequency ω_0. A detailed treatment of the photon-pair production in periodically-poled media can be found in [NME08], as it has been previously studied in *Université libre de Bruxelles* [PHNB+07]. PPLN waveguides have emerged as the preferred photon-pair source at telecommunication wavelengths because of their very high spectral brightness [TDRZ+01, TTDR+02, HBT+08]. The characteristics of the two waveguides we have used are presented in table 2.1.

At the output of the PPLN, the remaining pump beam is rejected by a fiber drop filter. It easily offers high isolation, the pump being at a very different wavelength than the photon pairs.

Table 2.1: Characteristics of the periodically-poled lithium niobate waveguides.

team	Brussels	Besançon
manufacturer	HC Photonics	HC Photonics
stabilization method	oven	Peltier cell
stabilization time	$\sim$ min	$\sim$ hours
length	4 cm	3 cm
chip normalized efficiency	80%/W/cm^2	150%/W/cm^2
input coupling efficiency	$\approx$ 50%	$\approx$ 65%
output coupling efficiency	$\approx$ 50%	$\approx$ 65%
output fiber	SMF	PMF

The photons of each pair are separated (with 50% probability) with a 3-dB fiber coupler, such that each photon in every entangled pair is sent through an independent EOPM. Note that a deterministic separation based on frequency can be achieved, as was done for the experiment involving interleavers, see section 2.6.

2.5.2 Manipulation

The photons pass through EOPMs (from EOSPACE) whose typical characteristics are presented in table 2.2. Their active axes must be aligned with the linear polarization of the photons. Our PPLN being of type I, the photons are identically polarized. In our experiments, either polarization-maintaining fiber components ensure that the photons' polarizations are aligned with the active axes of the modulators, or we carefully attach the non-polarization maintaining fibers and use fiber polarization controllers to realize the needed polarization rotations.

Table 2.2: Characteristics of the electro-optic phase modulators.

RF bandwidth	$\simeq$ 25 GHz
V_π	$\simeq$ 3 V
optical loss	2.5 – 3.5 dB

The EOPMs are driven by an RF signal at frequency $\Omega/2\pi = 12.5$ or 25 GHz, with adjustable amplitude and phase (a, α) and (b, β). These parameters must be set independently, precisely and reproducibly. To this end, we used RF systems where the signal of an RF generator is split and manipulated independently on Alice's and Bob's sides. We note that it is possible to use two synchronized RF generators instead of one, and share the synchronization signal through electronic cables or optical fibers. The limited RF power limits the accessible values of the parameter c defined by (2.2) and given by $c = \pi V_\pi^{-1} R^{1/2} P^{1/2}$, where V_π is the half-wave voltage of the EOPM, internal resistance $R = 50\,\Omega$, and P is the RF power applied to the modulator. For a radio-frequency 12.5 GHz we attained a maximal value of $c \approx 2.74$. At this value, eleven frequency bins are created, see figure 2.2. The bandwidth sampled by the EOPMs is thus approximately 125 GHz, which is much smaller than signal and idler bandwidths (approximately 5 THz).

Due to the equivalences demonstrated in section 2.3, the RF setup can be characterized entirely with classical light. This allows us to perform precise calibration measurements. In [OCN$^+$10], manual phase shifters and attenuators were used. In [OMW$^+$12], a dedicated RF architecture based on frequency translation allowed high-resolution phase and amplitude control of the RF

signals with better accuracy. The RF phase was automatically controlled by I&Q modulation, while the RF amplitude still made use of mechanically adjustable attenuators. Details can be found in [OMW+12]. Finally, we developed the fully-automated RF system of figure 2.10, which was used in [OWPH+14] and subsequent experiments.

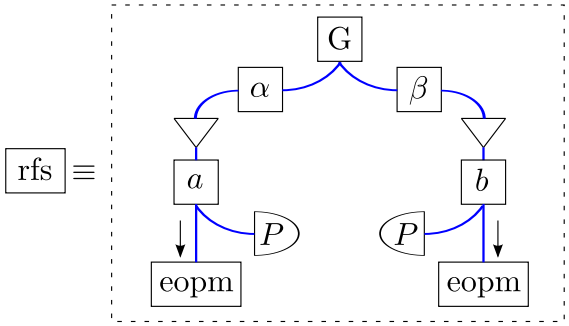

Figure 2.10: Detail of the radio-frequency system. The power of a 25-GHz generator G is split by a power splitter and directed to Alice's and Bob's EOPMs. RF isolators (not shown) guarantee the independence of each arm. The phases α and β are fixed by variable phase shifters. After amplification, amplitudes a and b are adjusted with variable attenuators. Ten per cent of the power of each signal is sent to an RF power meter allowing precise measurement of the RF power applied to the EOPM. The motorized phase shifters and attenuators are remotely-controlled and interfaced to a computer.

Precise characterization of the setup of figure 2.10 shows a phase reproducibility better than 10^{-2} rad, while power resolution is 10^{-2} dB, with a precision better than 0.1 dB. A MATLAB routine allows to switch on and off the RF generator and amplifiers and to select amplitudes and phases (a, α) and (b, β). This is realized by controlling the voltage sources linked to the motor-driven RF phase shifters and attenuators. We implemented a voltage switch to be able to increase or decrease these parameters in a fully automated way.

2.5.3 Filtration

Figure 2.11 illustrates the action of frequency filters. They need to discriminate between frequency bins separated by a radio-frequency of 12.5 or 25 GHz. In our setup, narrow-band frequency filters were implemented with fiber Bragg gratings (FBGs) preceded by a circulator, the reflected frequency being detected. The FBGs were characterized with a broadband light source. The main characteristics of the FBGs we used are presented in table 2.3.

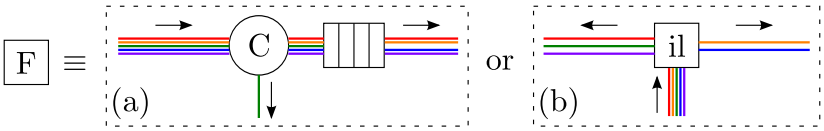

Figure 2.11: Detail of the frequency filtration. (a) Selection of one frequency bin with a fiber Bragg grating preceded by a circulator C. (b) Separation between even and odd frequency bins with an interleaver IL.

The spectral characteristics of the home-made FBGs used in [OCN+10, OMW+12] are visible on figure 2.2. Fixed filters select photons belonging to the frequency bin $[\omega_F - \Omega_F/2, \omega_F + \Omega_F/2]$ centered on $\omega_F = \omega_0$ and restricted to a 3 dB width $\Omega_F/2\pi \approx 3$ GHz, smaller than the radio-frequency $\Omega/2\pi = 12.5$ or 25 GHz. The filter transmission drops very steeply. Isolation better than 30 dB at half the radio-frequency Ω ensures that frequency bins are well isolated from

Table 2.3: Characteristics of the fiber Bragg gratings.

team	Besançon	Brussels
manufacturer	home-made	Acreo
wavelength	1547.7 nm or tunable	tunable around 1552 nm
full width at half maximum	$\approx$ 3 GHz	$\approx$ 4 GHz
isolation at 6.25 and 12.5 GHz	$>$ 30 dB	$\approx$ 30 dB
loss	$\approx$ 0.2 dB	$\approx$ 0.5 dB

each other. The filters are athermally packaged to reduce central wavelength deviation to 1 pm/K, which is very important to ensure the stability of the experimental measurements. A misalignment would affect the coincidence rate, see the function $g(\omega)$ in (2.30). We recall that the bandwidth of the pump laser (approximately 2 MHz) is much smaller than the bandwidth of the FBGs, while the bandwidth of the signal and idler photons (approximately 5 THz) is much larger. In [OCN$^+$10], the temperature of Bob's filter is controlled by a Peltier module, which allows continuous tuning of the reflected frequency ω_B over a 1-nm range around ω_0. In [OWPH$^+$14], interleavers (OPTOPLEX) aligned on the ITU grid were used. The principle is illustrated in figure 2.11. We refer to section 2.6 for more details.

2.5.4 Detection

The photons are detected with single-photon detectors (SPDs) of two types: avalanche photodiodes (APDs) and superconducting single-photon detectors (SSPDs). Table 2.4 presents their main characteristics, as measured in our experimental implementations. Imperfections of SPDs include that the probability of detection given a photon enters the device (the efficiency η) is less than one, and that the device will click at a non-zero rate (the dark-count rate τ_{dk}) even when no photon is present.

Table 2.4: Characteristics of the single-photon detectors.

type	APD	SSPD
manufacturer	idQuantique	Scontel
model	id201	FCOPRS-001
wavelength	C-band	visible and IR
operation mode	gated at 100 kHz	continuous
	with 100 ns time windows	
efficiency	10 – 15%	$\simeq$ 5%
dark-count rate	$2 \cdot 10^{-5}$ – $6 \cdot 10^{-5}$ /ns	$\simeq$ 10 Hz
	(i.e. 200 – 600 kHz)	(condition-dependent)
timing jitter	$\simeq$ 500 ps	$\simeq$ 50 ps
temperature	-50°C (Peltier module)	1.7 K (helium vapor)

The signals generated by the SPDs are directed to a data acquisition system (DAS). A time-to-digital converter (TDC, AGILENT Acqiris system, timing resolution of about 50 ps) measures the time $t_B - t_A$ elapsed between the arrival of an electric signal at a "start" electronic input and the arrival of a signal at a "stop" input. The raw values are stored and treated by a MATLAB routine to produce histograms of the events, i.e. the number of coincident detection events as a function of $t_B - t_A$. Figure 2.12 illustrates a typical coincidence measurement. It exhibits a narrow peak when the photons arrive in coincidence, superposed to a background due to accidental coincidences. Automated RF control and measurement data acquisition (both for

two-photon experiments and characterization procedures) has enabled full automatization of our experiments: rates are measured during automatically adjustable times in automatically adjustable RF configurations.

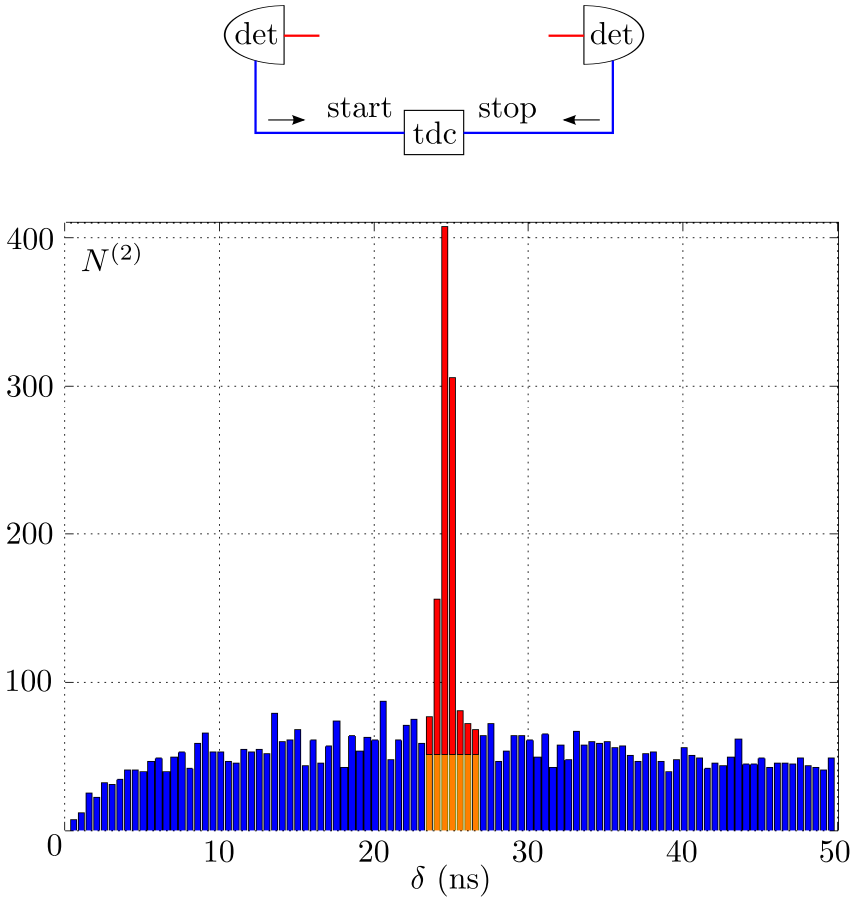

Figure 2.12: Detail of the data acquisition system. A detection event on Alice's detector triggers the data acquisition: the electric signal is sent to a time-to-digital converter TDC. At the reception of an electric signal from Bob's detector, the TDC stores the time elapsed between the two events. The bottom figure shows a typical histogram. When correlated photons are present, a coincidence peak emerges from these time-resolved coincidence measurements. An automated data analysis allows to extract the values of raw and net coincidence counts (in red and orange, estimation of N_{net} and N_{noise}). One can straightforwardly generalize the principle with more than two detectors.

Note that in [OCN+10], [OMW+12] and [POD+13] (see chapter 5), we used one "stop" signal, as shown in figure 2.12, but the TDC accepts several "stop" signals. In [OSC+13] (see chapter 4), we used three detectors, one for Alice and two for Bob, implying a straightforward two-"stop" generalization of the setup. In [OWPH+14], we used four detectors, two for each protagonist, implying the necessary division of Alice's detection signals to produce one "start" signal common to both her detectors, and four "stop" signals.

To quantitatively analyze the results of coincidence measurements, we define the raw and net numbers of coincident events

$$N_{\text{raw}} = \int_{t_i}^{t_f} N(t)\mathrm{d}t\,, \tag{2.57}$$

$$N_{\text{net}} = N_{\text{raw}} - N_{\text{noise}} = N_{\text{raw}} - (t_f - t_i)\tau_{\text{acc}}\,, \tag{2.58}$$

where

$$\tau_{\text{acc}} = \frac{1}{t_{\max} - t_f} \int_{t_f}^{t_{\max}} N(t)\mathrm{d}t \tag{2.59}$$

is the rate of accidental coincidences, and $N(t)$ is the number of coincidences at time $t = t_{\text{B}} - t_{\text{A}}$. We thus define a signal time window whose jitter-dependent size $t_f - t_i$ (typically $\sim$ ns) has to be carefully —since all the quantities will depend on this definition— selected (manually or by the MATLAB routine) so as to contain all the signal coincidence counts. Outside this window, up to the maximum delay $t_{\max}$, only noise is present. Estimation of N_{net} with (2.58) and (2.59) relies on the assumption that the noise is uniformly distributed through the histogram, so that N_{noise} is the estimation of the number of coincidences due to the accidental background. In general this assumption is verified in the vicinity of a coincidence peak; if this is not the case, the procedure can be easily generalized to other-shaped backgrounds of accidental coincidences.

The signal coincidence counts originate from the joint detection of each photon of a given pair. Due to imperfect sources and detectors, the background noise has several origins: a joint detection of two photons originating from two different pairs or from another optical generation process, a detection of a photon and a dark count, or two dark counts. Such a background depends greatly on the detectors' parameters, and on the source characteristics. It is then natural to consider the net coincidence counts to evaluate the quality of our setup for manipulating entangled photons. In particular, we expect the theoretical prediction (2.40) to be better verified when considering the net coincidence counts. It is also important to note that in our experiments the quantities $N(a, \alpha; b, \beta; n)$ and $N(a = b = 0; n)$ intervening in (2.40) cannot be measured simultaneously. In order to evaluate the *normalized rate*

$$\tilde{N}_d^{(2)}(a, \alpha; b, \beta; n) = \frac{N_d^{(2)}(a, \alpha; b, \beta; n)}{N_{d=0}^{(2)}(a = b = 0; n)}\,, \tag{2.60}$$

we have to assume that the quantity $N_{d=0}^{(2)}(a = b = 0; n)$ is known, being evaluated with sequential or parallel measurements. Such an assumption relies on the stability of the setup, and creates for example loopholes in Bell tests, see section 3.1.

Our automated data treatment allows to extract important quantities such as the coincidence rate, the coincidence-to-accidental ratio CAR (or signal-to-noise ratio SNR), the coincidence peak bandwidth, and the *raw* and *net* visibilities, defined as follows:

$$V_{\text{raw}} = \frac{N_{\max} - N_{\min}}{N_{\max} + N_{\min}}\,, \tag{2.61}$$

$$V_{\text{net}} = \frac{(N_{\max} - N_{\text{noise}}) - (N_{\min} - N_{\text{noise}})}{(N_{\max} - N_{\text{noise}}) + (N_{\min} - N_{\text{noise}})}\,, \tag{2.62}$$

where $N_{\max}$ and $N_{\min}$ correspond to the (raw) maximal and minimal coincidence counts when varying the RF parameters. The visibility is a critical parameter for the quality of a setup. Its evaluation can be done directly with the data or via an adjusted curve, e.g. based on a statistical "fit". We note that the duration of each measurement has to be long enough so as to allow a good statistical precision —which scales as the square root of N— on the evaluation of all the quantities involved in the data treatment.

We conclude by noting that the coincidence measurements can be efficiently simulated when taking into account all the parameters of the experiment: source rate and emission spectrum, optical losses, radio-frequency parameters, filters' spectra, detection efficiency and jitter, etc.

2.6 Experimental results

Our experimental results published in [OCN+10], [OMW+12] and [OWPH+14] are based on the generic setup of figure 2.8 and rely on the components described in section 2.5.

In [OCN+10], the non-stabilized pump laser is set at $\lambda_p \approx 773.865$ nm, corresponding to a degeneracy wavelength $\lambda_0 = 2\pi c/\omega_0 \approx 1547.73$ nm. It injects 6 mW of power into the Besançon PPLN. EOPMs are driven by $\Omega/2\pi = 12.5$ GHz signals whose parameters are mechanically adjusted. The reflected frequency of Alice's FBG is kept fixed on ω_0 while the value of d is chosen by adjusting the reflected frequency of Bob's filter to $\omega_0 + d\Omega$. The photons belonging to the frequency bin reflected by the filters are detected with APDs set on 15% efficiency. Coincidences are measured at a rate of approximately 10 Hz, with a CAR value around 100 when modulation is turned off. The data are background-corrected. The normalized (net) coincidence rate $\tilde{N}_d^{(2)}(a, \alpha; b, \beta; n = 0)$ plotted in figure 2.14 as a function of the RF parameters exhibits two-photon interference.

First, we scanned the modulation amplitudes $a = b$ (taken to be equal) when $\delta \equiv \alpha - \beta = 0$. The number of frequency bins that interfere together is approximately given by the number of values of d for which N_d takes a significant value, and it increases when a, b increase. In our experiment, we were able to scan the values $a, b \in \{0, 2.74\}$. When $a \approx b \approx 2.74$, there are contributions from $d = 0$ to $d = 5$. By the symmetry of (2.40), there should also be contributions from $d = -1$ to $d = -5$. This shows that at least eleven frequency bins are coherently addressed by the EOPMs.

Second, we scanned the phase δ when $a \approx b \approx 2.74$. Equation (2.40) predicts that when $\delta = \pi$, only $d = 0$ contributes, and that the quantity $N_{d=0}^{(2)}(a = b = 2.74, \delta; n = 0)$ should vanish for specific values δ^*. This allows us to estimate the visibility of interferences through the usual formula (2.62), with the maximum for $\delta = \pi$ and the minimum for $\delta = \delta^*$. From the data reported in figure 2.14, we estimate that the net visibility is equal to $98 \pm 1\%$.

Note that the acquisition time per measured point was constant, corresponding to a number of coincidences approximately equal to $10^3 \tilde{N}$. Statistical uncertainties are the main source of uncertainty. The remaining discrepancies between theoretical curves and experimental measurements are due to other factors, such as lack of stability of the pump laser (visible in the $d = 1$ curve versus $\alpha - \beta$), limited precision on the RF parameters, and limited visibility. Note also that when $d = 5$, the filter FBG_B was at the limit of its tuning range, and it may have not been perfectly centered on $\omega_0 + 5\Omega$, in which case there would be a systematic underestimation of $N_{d=5}$.

In [OMW+12], the analogically-stabilized pump laser is set at 773.8715 nm, corresponding to a degeneracy wavelength of 1547.743 nm. It injects 3 mW of power into the Besançon PPLN. EOPMs are driven by 25 GHz signals generated by the frequency translation setup, with automated control of phases (and accuracy much improved) and manual control of amplitudes. Both home-made FBGs are kept fixed on the degeneracy wavelength. The photons are detected with SSPDs. Coincidences are measured at a 20-Hz rate, with a CAR value approximately equal to 2×10^3 when modulation is turned off. High stability of the source, stability and precision of the RF signals driving the EOPMs, and use of low-noise SSPDs, allow us to detect the two-photon interference pattern with high precision.

We tested the equivalence of the experiments represented in figures 2.3, 2.4 and 2.5: as predicted by equations (2.20), (2.27) and (2.40), rates $N^{(\text{class})}$, $N^{(1)}$ and $N^{(2)}$ should have the same functional dependence on the RF parameters. In the case of classical optics and one-photon experiments, we presented in total three versions of the experiment, differing mainly in the optical source S employed, which can be a coherent polarized narrow-band laser, a non-coherent

non-polarized broadband light source or a broadband incoherent source attenuated to reach the single-photon regime. In the first case, neither filtration nor polarization management is required, since all the photons emitted already belong to a given frequency bin, with their polarization aligned with the active axes of the modulators. In the second version, the light beam must first pass through a filter and a polarizer before being sent through the setup; this corresponds more strictly to the entangled-photon case, where signal and idler photons have a broad spectrum. For the single-photon experiment, the broadband source is attenuated until it contains, on average, much fewer than one photon in each frequency bin within each 2.5-ns detection time window of the APD used in gated mode with 100-kHz repetition rate.

We chose $d = 0$ and varied the parameter C, defined by (2.15), by scanning one of the phases α or β with $a = b$ fixed. As mentioned, this procedure permits evaluation of the interference visibility, the value of which is critical for the performance of the system. We extract the visibilities using (2.61) and (2.62). The maximal rate $N_{\max}$ is obtained in principle for $C^* = 0$, such that $J_0^2(C^*) = 1$. For $a = b$ this is achieved with a phase difference $\alpha - \beta = \pi$. The minimal rate $N_{\min}$ is obtained for any of the positive roots $\{C_i^*\}$ of J_0, for which $J_0^2(C_i^*) = 0, \forall i$. The visibility therefore attains a theoretical maximum value of 1. If $a = b$, the first root C_i^* is attainable at sufficiently high RF powers ($a = b \gtrsim 1.2$) with the phase difference $\alpha - \beta = \arccos(C_1^{*2}/2a^2 - 1)$.

Our results are summarized in figure 2.15 and table 2.5. Figure 2.15 is a plot of $J_d\big([a^2 + b^2 + 2ab\cos(\alpha - \beta)]^{1/2}\big)^2$ as a function of $\alpha - \beta$ for $d = 0$ and $a = b \approx 2.25$. The experimentally derived rates $N^{(\text{class})}$, $N^{(1)}$ and $N^{(2)}$ —normalized by $N^{(\text{class})}$, $N^{(1)}$ and $N^{(2)}$ with modulation turned off— are superposed to the theoretical curve. The close agreement of the experimental data taken with the different experimental schemes validates the predictions of (2.20), (2.27) and (2.40), and thereby demonstrates the equivalence of the classical optics, single-photon and two-photon experiments. Note that an uncontrolled phase shift arises due to propagation times in the optical fibers between the source and each EOPM, see discussion in section 3.4. The experimental results are therefore horizontally shifted in order to obtain the best possible agreement with the theoretical curve. This is the only parameter that is adjusted to fit the data.

Table 2.5: Experimentally measured visibilities. Data from [OMW+12].

	Classical expt (laser source)	Classical expt (broadband source)	One-photon expt	Two-photon expt
V_{raw}	$(99.79 \pm 0.01)\%$	$(99.41 \pm 0.12)\%$	$(87.25 \pm 0.38)\%$	$(99.17 \pm 0.11)\%$
V_{net}	$(99.79 \pm 0.01)\%$	$(99.41 \pm 0.12)\%$	$(99.27 \pm 0.43)\%$	$(99.76 \pm 0.11)\%$

Table 2.5 gives the values of the visibilities V_{raw} and V_{net} extracted from curves such as those reported in figure 2.15. In the classical case a very low noise detector was used to measure maximal and minimal rates, which is why $V_{\text{raw}} \approx V_{\text{net}}$. Both the laser source and the broadband source were used. In the single-photon case an APD with a relatively high dark-count rate was used, which explains the low value of the raw visibility. In the entangled-photon case, the high value of V_{raw} is due to the quality of the SSPDs used, which are much less noisy than APDs. Maximal and minimal rates were measured for several minutes in order to obtain a good statistical precision on the visibilities.

The values of V_{raw} depend strongly on the noise inherent in the detectors and thus vary greatly across the different cases. By contrast, the values of V_{net} are all almost equal and notably high. This agreement once again confirms the equivalence between the different experiments. It also allows us to separate the contributions to visibility degradation due to the experimental setup from those inherent to the detectors (detector noise and dark counts) and sources (in particular noise due to multi-photon events) used. The main contributions from the setup itself are imperfect frequency-bin isolation, imperfect polarization management and imperfect

control of the RF parameters. The visibilities we obtained are comparable to the best results reported for two-photon interference at telecommunication wavelengths; see, e.g., [MIH+10].

In [OWPH+14], we reported two-photon interference obtained with the periodic frequency filters called interleavers, see section 2.4 and figure 2.16. The numerically-stabilized pump laser is set at $\lambda_p = 776.1617$ nm, corresponding to a degeneracy wavelength $\lambda_0 = 1552.3234$ nm. It injects 0.7 mW of power into the Brussels PPLN. EOPMs are driven by 25 GHz signals created by the fully-automated setup of figure 2.10. The photons are detected with four APDs (the id201's of table 2.4 and noisier id200's) operated at 10% efficiency. When modulation is off, coincidences are measured at a rate ≈ 1.5 Hz and with a CAR of ≈ 2. These low values are due to the gated operation and high dark-count rates of the APDs, and to the high losses from pair creation to detection (≈ 18 dB for each channel, see below). The setup corresponding to this configuration is represented in figure 2.13.

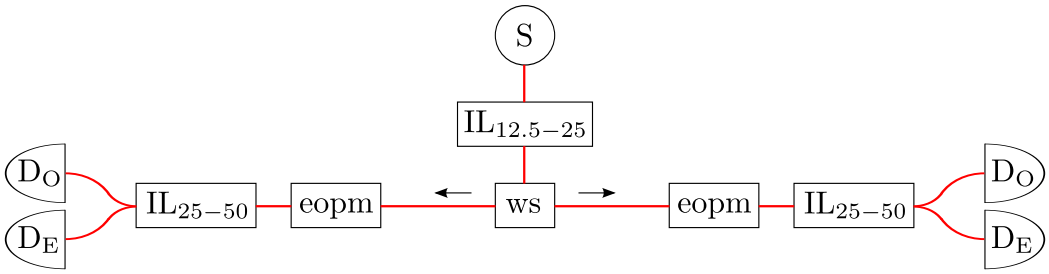

Figure 2.13: Experimental setup with interleavers. Photons from the PPLN pass through a 12.5–25 interleaver creating a nice frequency comb, and a few frequency bins are selected and separated by a WaveShaper filter. After polarization management (not shown) and phase modulation, odd (O) and even (E) frequency bins are detected behind a 25–50 interleaver on each side.

The degeneracy frequency is $\omega_0/2\pi = c/2\lambda_p = 193.125$ THz. In what follows, we relate frequencies to the International Telecommunication Union DWDM grid in the C-band: multiples of 50 GHz are said to be on the 50-grid, multiples of 25 GHz are on the 25-grid, and other frequencies are off the grid. In order to create a nice frequency comb, the photons pass through a 12.5–25 frequency interleaver. The photons whose frequencies belong to a-few-GHz-wide intervals centered on the 25-grid are collected at the output, while those centered on intervals with a 12.5 GHz offset are thrown away with more than 25 dB extinction. The reason for using this first filter can be understood with figure 2.17, where the transmission spectra of all filters used in the experiment are shown. Indeed, whereas the outputs of the 25-50 interleavers (discriminating even and odd frequencies before detection, see below) have ≈ 25 dB extinction at the center of each pass band, they only have ≈ 3 dB extinction at the edges of the band. Hence photons at the edges of the pass bands have quite high and equal probabilities to exit the even and odd ports, which would result in an important decrease of visibility of interference if the 25–50 interleavers were used alone. The spectra in panel (d) of figure 2.17 show that upon using the initial 12.5–25 interleaver that removes the photons at the edges of the pass bands, the even and odd outputs are now separated by 25 dB over the whole frequency band.

The state at the output of this periodic filter can be written as in (2.33):

$$|\Psi\rangle = \sum_{n\in\mathbb{Z}} f_n |n\rangle|-n\rangle \otimes \int_{-\Omega/2}^{\Omega/2} \mathrm{d}\omega\, h(\omega)\, |\omega\rangle|-\omega\rangle\,, \tag{2.63}$$

where $\Omega = 25$ GHz and $h(\omega)$ is a function that represents the effect of the 12.5–25 frequency interleaver (it is maximal around $\omega = 0$ and tends rapidly to zero). The pump is rejected with more than 100 dB extinction when taking into account all filters preceding detection.

Photons then pass through a programmable filter (WaveShaper from FINISAR) which is configured to direct photons from bins $n = +(\text{resp. } -)1, 2, 3, 4, 5, 6$ to Alice (resp. Bob). Thus we obtain the state

$$|\Psi\rangle = \frac{1}{\sqrt{6}} \sum_{n=1}^{6} |n\rangle|-n\rangle \otimes \int_{-\Omega/2}^{\Omega/2} \mathrm{d}\omega\, h(\omega)\, |\omega\rangle|-\omega\rangle\,, \tag{2.64}$$

where we omit the factors f_n on such a reduced bandwidth. The restriction to only 6 frequency bins is realized so that dispersion can be neglected. Otherwise, photons in different frequency bins accumulate different phase shifts during propagation through the optical fibers that deteriorate the two-photon interference pattern. The number of frequency bins could be increased if dispersion compensation were implemented. Note that limiting the number of frequency bins will decrease the visibility of the interference pattern.

On each arm, a polarization controller followed by a polarizer ensures that the polarization of the photons is aligned with the axis of the EOPM. Finally, the photons are directed to a 25–50 frequency interleaver. One output collects photons belonging to the 50-grid, i.e. frequency bins with n odd (result O), while the other collects photons remaining from the 25-grid, i.e. frequency bins with n even (result E). The four APDs allow the simultaneous acquisition of EE, EO, OE and OO coincidences by the TDC. Histograms show that when no modulation is applied, only EE and OO coincidences are present, as expected by (2.64). We note that it is possible to change the correlations by changing the wavelength of the pump: e.g., when $\lambda_p = 776.1115\,\text{nm}$, we measure inverted correlations.

The experimental measurements, some of which are shown and commented in figure 2.16, are in good agreement with the theoretical predictions (2.56). When $a = b$, the probabilities $P(\mathrm{E},\mathrm{O})$ and $P(\mathrm{O},\mathrm{E})$ should vanish when the phase difference $\alpha - \beta$ is scanned, which enables one to evaluate the (net) visibility (2.62) of the interference fringes. For the value $a = b = 0.6955$ used in the figure, we measured $V = 90\%$ and $V = 80\%$ depending on which combination, EO or OE, is considered. This limited visibility is attributed to non-ideal state preparation: limited bandwidth and dispersion.

The experiment reported in [OWPH$^+$14] could be further improved. The coincidence rate, CAR, and interference visibility could be enhanced by the use of SSPDs. Using a designated filtering line and/or a source based on a resonator which would directly produce a frequency comb of the form (2.63) would limit losses and enhance purity of the quantum state. The full bandwidth of the two-photon state could be exploited provided dispersion management is realized. These improvements would bring the method closer to practical applications.

Hence, using frequency-bin entangled photons, one has the choice to exploit high-dimensional entanglement [OCN$^+$10, OMW$^+$12], or to manipulate more conventional two-dimensional entanglement, on which most quantum information protocols are based [OWPH$^+$14]. Advantages of frequency-bin entanglement include: the use of optical, electro-optic and RF components that are commercially available and allow easy interconnection and remote control; the use of optical components that allow good polarization management, frequency-bin isolation and stability; the use of an RF system that allows stability, independence, easy calibration and precise adjustment of parameters; overall reproducibility and robustness allowing day-long experiments with no measurable drift or decrease in performance; no interferometric stabilization required over laboratory distance scales (meters of optical fibers). Manipulating frequency entangled photons with EOPMs and frequency filters, raw visibilities in excess of 99% can readily be obtained (comparable to the highest visibilities obtained using other photonic degrees of freedom) and high-dimensional quantum states can be manipulated (dimension as high as eleven easily obtained). Our method is potentially a competitive platform for the realization of quantum communication protocols at telecommunication wavelengths.

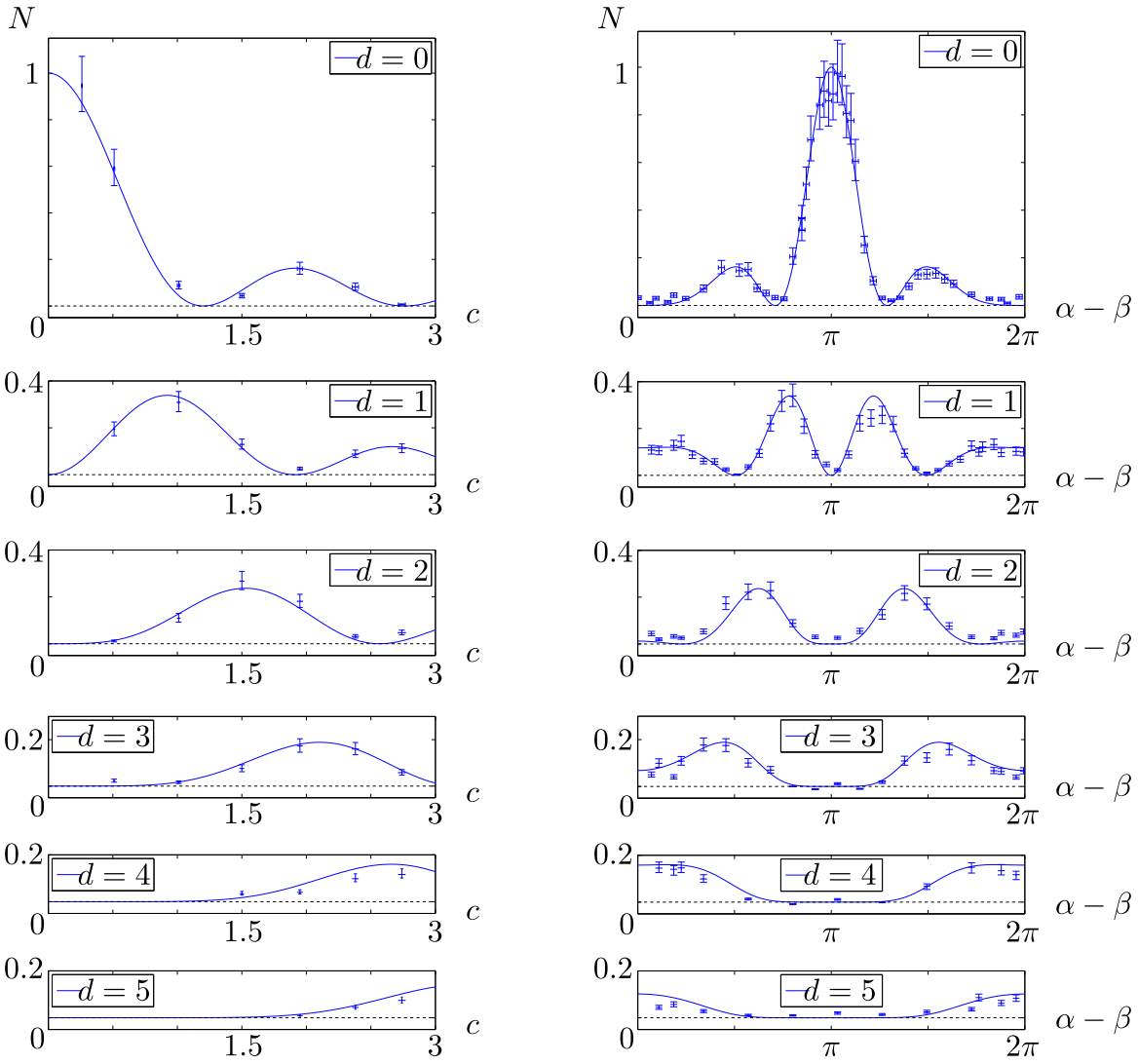

Figure 2.14: High-dimensional two-photon interference patterns versus radio-frequency parameters. Theoretical predictions (curves) and experimental measurements (symbols with error bars) of the normalized coincidence rate N_d. Left: $N_d(c, c, \alpha - \beta = 0)$ when $\alpha - \beta \approx 0$ and the amplitude $a \approx b \equiv c$ is scanned, for $d = 0, 1, 2, 3, 4, 5$. The experimental measurements are plotted entirely in terms of measured quantities, and do not depend on any adjustable parameters. Values of c are deduced from measures of the radio-frequency power. Horizontal error bars are due to the limited resolution of the power meter used (we assumed a relative uncertainty on c of 10^{-2}). Vertical error bars are statistical. Right: $N_d(a = 2.74, b = 2.74, \alpha - \beta)$ when $a \approx b \approx 2.74$ and the phase $\alpha - \beta$ is scanned, for $d = 0, 1, 2, 3, 4, 5$. To plot the experimental measurements we used the value indicated by the mechanical phase shifter, x, and converted it to a phase value using the relation $\alpha - \beta = \mu x + \nu$. Parameters μ (which can be determined by classical measurements) and ν were adjusted to get a good fit with the theoretical predictions. Horizontal error bars are due to the limited resolution of the phase shifter used (we assumed an absolute uncertainty on $\alpha - \beta$ of 5×10^{-2} rad). Vertical error bars are statistical. Figure adapted from [OCN+10].

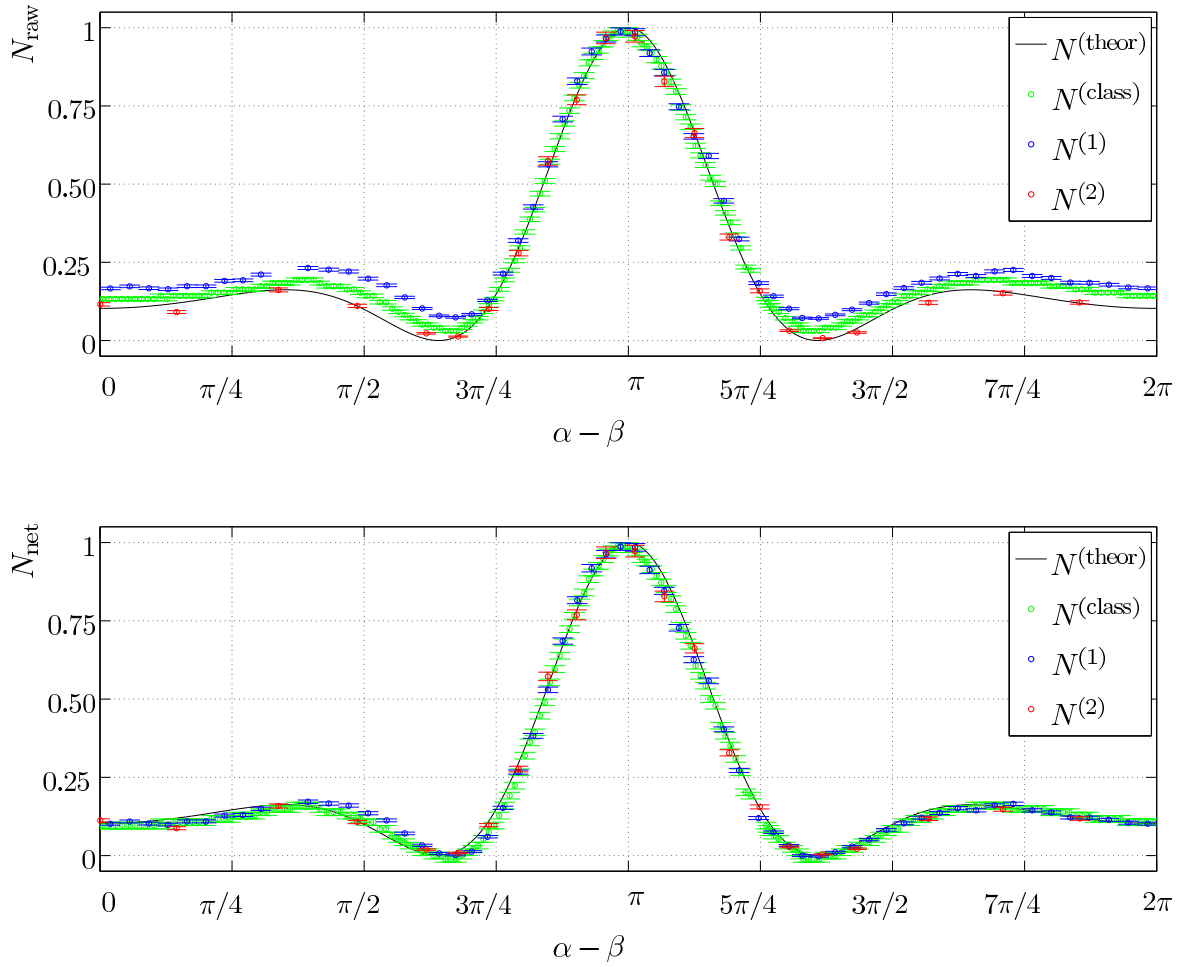

Figure 2.15: High-visibility interference patterns in the frequency domain. The Bessel-type interference described by (2.20), (2.27) and (2.40) is plotted for $d = 0$ and $a = b \approx 2.25$ as a function of the phase difference $\alpha - \beta$. The raw (with detector noise) and net (detector noise subtracted) data are shown respectively on the top and bottom panels. On both plots, the theoretical curve is included in black, the green data points are the normalized light intensity $N^{(\text{class})}$ (obtained using the tunable laser source), the blue data points correspond to the normalized photon rate $N^{(1)}$, i.e. the single-photon interference pattern (obtained using the broadband source, attenuated to the single-photon regime), and the red data points correspond to the normalized coincidence rate $N^{(2)}$, i.e. the two-photon interference pattern (obtained using the PPLN source). The error bars are statistical. Note that the classical measurements $N^{(\text{class})}$ are made with a relatively noisy photodiode, and the raw visibility for the green data points in the top panel is therefore less than reported in table 2.5, where a low-noise photodiode was used. Note also that when detector noise is subtracted (bottom panel) the different experimental data points superpose exactly, demonstrating the equivalence of the interference schemes, but deviate slightly from the theoretical curve. We attribute this to small errors in the calibration of I&Q parameters, so that the actual RF phases α and β deviate slightly from their theoretical value. Figure from [OMW+12].

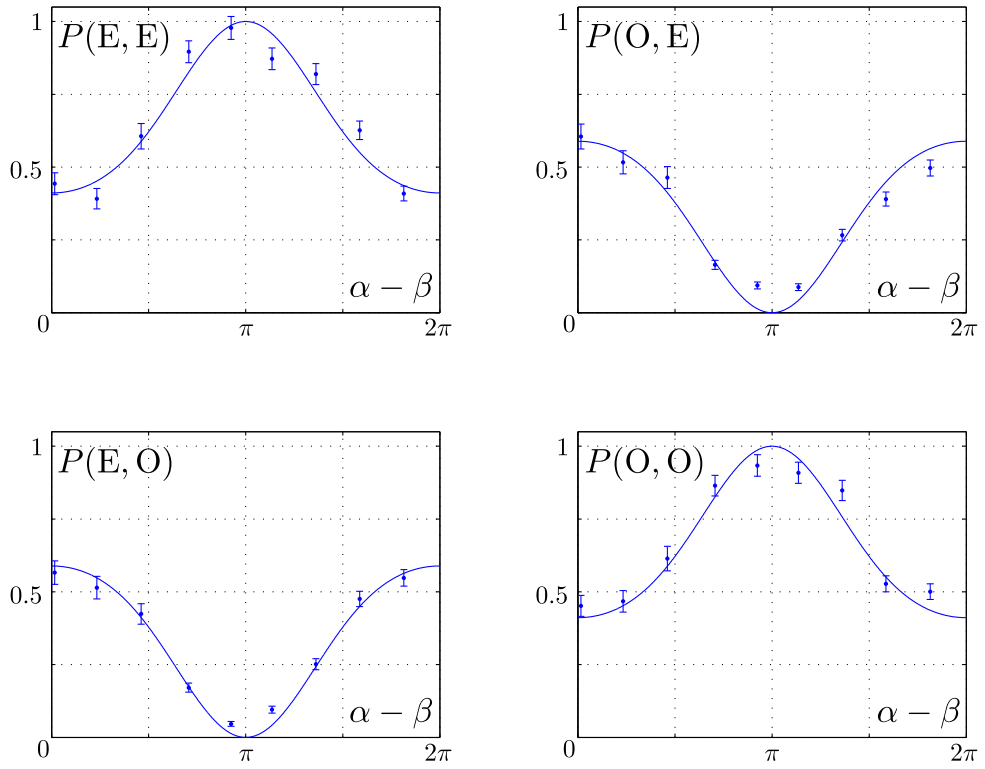

Figure 2.16: Two-dimensional two-photon interference patterns using interleavers. Parameters are: $a = b = 0.6955$, and α is changed with β kept constant. Curves are theoretical predictions (2.56) for coincidence probabilities $P(\mathrm{E},\mathrm{E})$, $P(\mathrm{E},\mathrm{O})$, $P(\mathrm{O},\mathrm{E})$ and $P(\mathrm{O},\mathrm{O})$. Symbols are experimental results: they correspond to the number of coincidences $N(\mathrm{E},\mathrm{E})$, $N(\mathrm{E},\mathrm{O})$, $N(\mathrm{O},\mathrm{E})$ and $N(\mathrm{O},\mathrm{O})$ simultaneously registered for each combination of outputs. A normalization based on the coincidence rates registered when modulation is off is realized; error bars are statistical; background noise of the histograms has been subtracted. The net interference visibility (calculated on curves that should cancel) is evaluated to be $(85 \pm 5)\%$, depending on the combination considered. Figure from [OWPH$^+$14].

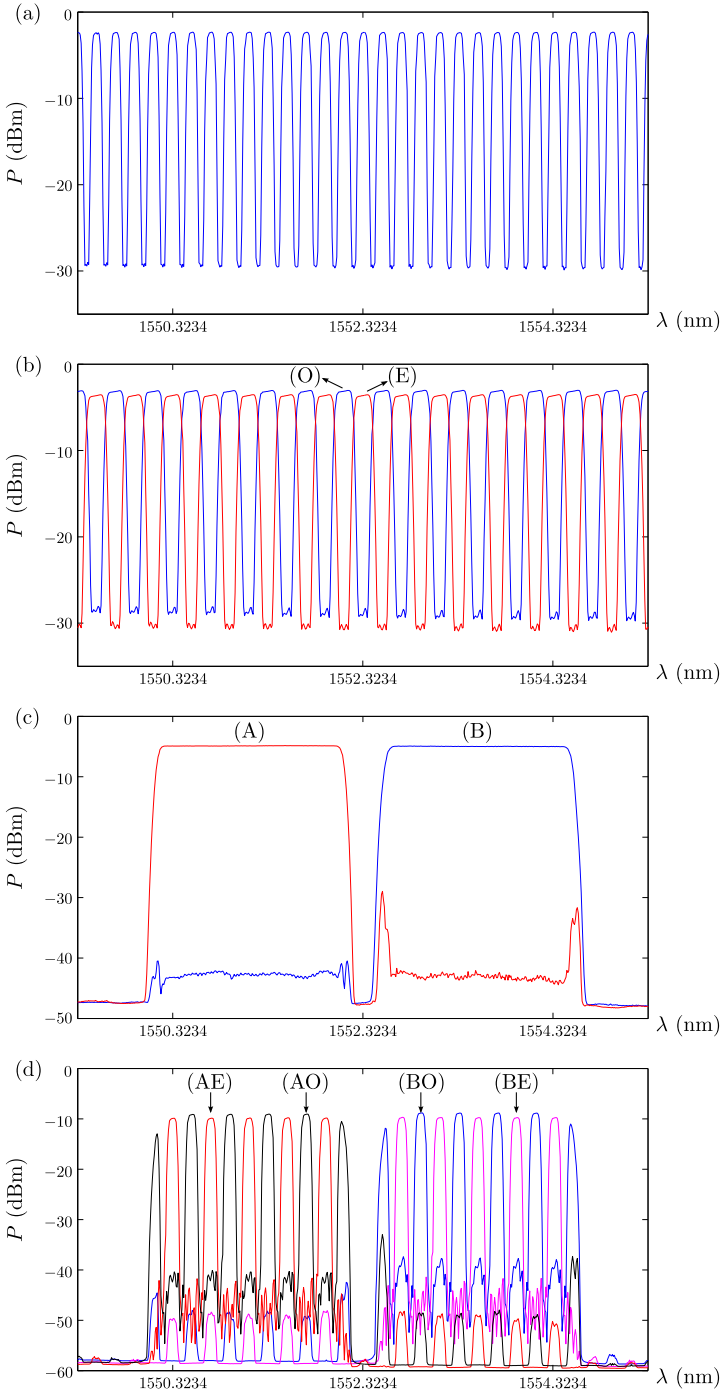

Figure 2.17: Spectra of the periodic frequency filters called interleavers. Since $\lambda_p = 776.1617\,\text{nm}$, 1552.3234 nm corresponds to the degeneracy frequency ω_0. From top to bottom: a) Output of the 12.5–25 interleaver. b) Even (red curve labeled E) and odd (blue curve labeled O) outputs of a 25–50 interleaver. c) Programmable WaveShaper filter; photons belonging to the red, labeled A, (resp. blue, labeled B) output are sent to Alice (resp. Bob). d) Spectrum obtained when cascading 12.5–25 interleaver, WaveShaper and 25–50 interleaver; red curve labeled AE: Alice, even; black curve labeled AO: Alice, odd; magenta curve labeled BE: Bob, even; blue curve labeled BO: Bob, odd. Figure from [OWPH+14].

Chapter 3

Uses of frequency-bin entangled photons

We have described in chapter 2 how frequency-entangled photons manipulated by electro-optic phase modulators (EOPMs) exhibit interference patterns in the frequency domain. Entanglement is a necessary resource for several quantum optics experiments and quantum information protocols. A standard experimental proof of manipulation of entanglement is to demonstrate a violation of a Bell inequality. In the first section of this chapter, we show that the two-photon interference patterns exhibited by frequency-bin entangled photons allow the violation of Bell inequalities. In the second section, we show how frequency-bin entanglement survives after interaction within plasmonic nanostructures, opening the way to investigations in *quantum plasmonics*, a promising new field for subwavelength quantum optics. In the third section, we recall previous results demonstrating that EOPMs can be used to code information in the frequency domain in view of quantum key distribution (QKD) applications [BMMP07], and we present a potential alternative implementation. Finally, we briefly discuss other potentialities of our method.

3.1 Violation of Bell inequalities

Here we show how frequency-bin entangled photons addressed locally by EOPMs can in principle be used to perform quantum nonlocality experiments. That is, we show that the correlations between Alice's and Bob's detectors should not be explainable by a local hidden variable (LHV) model, as discussed in section 1.2.

Frequency-bin entangled photons produce high-dimensional two-photon interference patterns. Detecting simultaneously all the results with narrow-band frequency filters would require a lot of detectors —one for each frequency bin. Here we consider a setup with only two detectors, one on Alice's side and one on Bob's side. We will make assumptions to reduce the requirements of the Bell test. The procedure we follow is exposed in [OCN+10].

Our starting point is the CH74 inequality (1.24), which we recall here:

$$P(++|x_0\,y_0) + P(++|x_0\,y_1) + P(++|x_1\,y_0) - P(++|x_1\,y_1) \leq P(+|x_0) + P(+|y_0)\,, \quad (3.1)$$

with $P(+|x) = \sum_b P(+b|x\,y)$, $P(+|y) = \sum_a P(a+|x\,y)$, and where x_0, x_1 are two possible settings of Alice's measurement apparatus and y_0, y_1 are two possible settings of Bob's measurement apparatus. In our case, the measurement settings correspond to a choice of amplitude and phase applied to the EOPMs: $x_0 = (a_0, \alpha_0)$, $x_1 = (a_1, \alpha_1)$, $y_0 = (b_0, \beta_0)$, $y_1 = (b_1, \beta_1)$.

Each measurement has two possible outcomes. The symbol + denotes one of them. The other outcome, −, does not intervene explicitly in the inequality. We take the outcome + in (3.1) to correspond to the photon being registered in the frequency bin "0", centered on the degeneracy frequency ω_0, on which is aligned a narrow-band frequency filter. All other frequency bins are associated with the result −, which is not detected in our setup.

The joint probabilities in (3.1) can be estimated directly, since they are proportional to the rate of coincidences $N^{(2)}_{d=0}$ in Alice's and Bob's frequency bins 0. The quantities $P(+|x_0)$ and $P(+|y_0)$ cannot be measured directly with our setup. However, we can estimate these quantities by making the following assumption, identical in spirit to the one made by Clauser–Horne in [CH74]:

$$P(+|x_0) = P(+|y_0) = P(+|a=0) = P(+|b=0) = P(++|a=b=0)\,. \tag{3.2}$$

The quantum theory of our experiment implies —assuming the variations of the function $f(\omega)$ describing the signal and idler photons bandwidths are negligible, see chapter 2— that (3.2) is true. We assume it is also obeyed by LHV models. That is, we assume, both in quantum theory and in LHV models, that the number of photons detected by Alice (Bob) in the frequency bin 0 is the same when Alice's (Bob's) detector has setting x_0 (y_0) and when Alice's (Bob's) phase modulator is turned off, that is, when $a = 0$ ($b = 0$).

Inserting (3.2) in (3.1) and dividing by $P(++|a=b=0)$ leads to the inequality $S \leq 2$, with experimental estimate

$$\begin{aligned} S &= [\,N^{(2)}_{d=0}(a_0,\alpha_0;b_0,\beta_0;n) + N^{(2)}_{d=0}(a_0,\alpha_0;b_1,\beta_1;n) + N^{(2)}_{d=0}(a_1,\alpha_1;b_0,\beta_0;n) \\ &\quad - N^{(2)}_{d=0}(a_1,\alpha_1;b_1,\beta_1;n)\,]/N^{(2)}_{d=0}(a=b=0;n) \qquad (3.3) \\ &= \tilde{N}^{(2)}_{d=0}(a_0,\alpha_0;b_0,\beta_0;n) + \tilde{N}^{(2)}_{d=0}(a_0,\alpha_0;b_1,\beta_1;n) + \tilde{N}^{(2)}_{d=0}(a_1,\alpha_1;b_0,\beta_0;n) \\ &\quad - \tilde{N}^{(2)}_{d=0}(a_1,\alpha_1;b_1,\beta_1;n)\,, \qquad (3.4) \end{aligned}$$

where the normalized coincidence rates $\tilde{N}$ are defined by (2.60). In order to investigate whether (3.3) can be violated experimentally, we first substitute (2.40) to rewrite (3.3) as

$$S = J_0^2(C_{00}) + J_0^2(C_{01}) + J_0^2(C_{10}) - J_0^2(C_{11})\,, \tag{3.5}$$

where

$$C_{ij} = \left[a_i^2 + b_j^2 + 2a_ib_j\cos(\alpha_i - \beta_j)\right]^{1/2}, \tag{3.6}$$

and $i,j \in \{0,1\}$. An analytic optimization of (3.5) was realized in [Woo10, OMW$^+$12]. The optimization relies on the fact that the parameters C_{ij} obey constraints imposed by the form of (3.6). In particular, they can be identified to the lengths of the sides of a quadrilateral, so that each of the four C_{ij} is bounded by the sum of the other three, e.g. $C_{11} \leq C_{00} + C_{01} + C_{10}$. The eight-parameter optimization of (3.3) is thus reduced to a four-parameter optimization with constraints. In [Woo10, OMW$^+$12], it is demonstrated that the optimum of (3.5) lies along the boundary $C_{00} = C_{01} = C_{10} = C_{11}/3$. The optimum $C_{00} \approx 0.550$, for which $S \approx 2.389$, corresponds to the RF parameters

$$(a_0,\alpha_0) = (b_0,\beta_0) = (0.275,\theta)\,, \qquad (a_1,\alpha_1) = (b_1,\beta_1) = (0.825,\theta+\pi)\,. \tag{3.7}$$

Reaching the optimal value requires the use of variable —but small— modulation amplitudes and precise phase adjustment.

In [OMW$^+$12], we evaluated the experimental violation of the CH74 inequality. Scans of both phases α and β at the amplitudes (a_0,b_0), (a_0,b_1), (a_1,b_0), (a_1,b_1) given in (3.7) enabled precise selections of the phases α_0, α_1, β_0, β_1 for which the violation is largest. Measurements were

then performed for phases and amplitudes optimizing the violation. The experimental results, listed in table 3.1, agree with the theoretical predictions up to the statistical errors and imply that the CH74 inequality is violated by more than 18 standard deviations. This again shows how frequency-bin entangled photons can be manipulated with high precision.

Table 3.1: CH74 Bell inequality violation results. $x_i\, y_j$, $i, j \in \{0, 1\}$, is the notational shorthand for $(a_i, \alpha_i; b_j, \beta_j)$. The column "Theory" gives the values that should be obtained at the point (3.7) for which the CH74 violation is maximal. Note that the experimental values agree with theoretical predictions up to statistical errors. Data from [OMW+12].

	Theory	Expt $N^{(2)}_{\text{raw}}$ (with noise)	Expt $N^{(2)}_{\text{net}}$ (noise subtracted)
$x_0\, y_0$	0.857	0.862 ± 0.006	0.861 ± 0.006
$x_0\, y_1$	0.857	0.863 ± 0.006	0.862 ± 0.006
$x_1\, y_0$	0.857	0.854 ± 0.006	0.853 ± 0.006
$x_1\, y_1$	0.182	0.190 ± 0.003	0.186 ± 0.003
S	2.389	2.389 ± 0.021	2.391 ± 0.021

For comparison we note that the maximum value of (3.3) attainable by quantum theory for systems of dimension 2 is 2.414, which is quite close to the maximum value of 2.389 attainable using EOPMs on frequency-bin entangled photons. However, as the frequency-bin entangled photons belong to a Hilbert space of dimension greater than 2, it may be that the maximum value attainable by some local measurements on the state exceeds this value. The algebraic maximum for this expression is 3, which cannot be exceeded by any measurement.

In [OCN+10], a similar Bell test was carried on, but by imposing a fixed amplitude $c = a_0 = a_1 = b_0 = b_1$, so that the coefficients (3.6) take the form $C_{ij} = \sqrt{2}c[1 + \cos(\alpha_i - \beta_j)]^{1/2}$, $i, j \in \{0, 1\}$. For a fixed c and taking without loss of generality $\alpha_0 = 0$, one must find the phases α_1, β_0 and β_1 optimizing (3.5). The results of the optimization are shown in table 3.2. The observed correlations do not reach the theoretical optima for large values of c. For large values the curve $N^{(2)}$ is more strongly peaked around $\alpha - \beta = \pi$. For the optimal values, $\alpha - \beta$ lies on the slopes of this peak. Relatively poor resolution of the components used in [OCN+10], leading to slight errors on a, b, α and β, provides a possible explanation for the discrepancy between the theoretical optima and the observed violation of (3.3). The theoretical value of S tends to the global optimal value of 2.389, but requires arbitrarily large RF amplitudes. When the amplitudes are large, the two-photon interference pattern is much more sensitive to small errors in the RF amplitudes and phases. In [OMW+12], the optimal value is attained for rather small values of the RF amplitudes. Together with more accurate components, this makes the experiment much more robust.

The CH74 inequality is based on a simplifying assumption on the marginal statistics that was not tested directly. The normalization quantity $N^{(2)}_{d=0}(a = b = 0; n)$ in (3.3) must be measured separately. Even assuming that (3.2) is true, an accurate evaluation relies on the stability of the experiment. Interleavers provide a way to get around this problem. When the states are two dimensional, it is easier to access all measurement outcomes simultaneously since only four detectors are needed, which is better suited for tests of the CHSH Bell inequality, see figure 1.1. Here we denote the two results $+$ and $-$ by E and O, i.e. the photon is detected in an even or odd frequency bin, with $x_i = (a_i, \alpha_i)$ and $y_j = (b_j, \beta_j)$, $i, j \in \{0, 1\}$, denoting choices of modulation amplitudes and phases. Inserting (2.56) into (1.16), with the definitions (1.9), the CHSH expression reads

$$S = J_0(2C_{00}) + J_0(2C_{01}) + J_0(2C_{10}) - J_0(2C_{11})\,, \tag{3.8}$$

Table 3.2: CH74 Bell inequality violation results with equal radio-frequency amplitudes. RF phases α_0, α_1, β_0 and β_1 optimize the violation of the CH74 inequality for RF amplitude $c = a_0 = a_1 = b_0 = b_1$. The experimental values, with statistical uncertainties, are compared to the theoretical predictions. Data from [OCN$^+$10].

c	α_0	α_1	β_0	β_1	S_{theor}	S_{expt}
0.51	0	1.42	3.85	2.43	2.15	2.14 ± 0.06
1.01	0	1.02	3.65	2.63	2.31	2.29 ± 0.06
1.50	0	0.72	3.50	2.78	2.35	2.27 ± 0.05
1.95	0	0.56	3.42	2.86	2.37	2.25 ± 0.05

with the parameters C_{ij} given by (3.6). Following reasoning similar to the optimization of the CH74 inequality, it is found in [Woo10] that (3.8) attains a maximal theoretical value of $S \approx 2.566$ at the point

$$(a_0, \alpha_0) = (b_0, \beta_0) = (0.2318, \theta)\,, \qquad (a_1, \alpha_1) = (b_1, \beta_1) = (0.6955, \theta + \pi)\,. \tag{3.9}$$

Even though the interference is not perfect, see section 2.6, a significant violation of the CHSH inequality is theoretically possible —but not equal to the value $2\sqrt{2}$ attainable with maximally entangled qubits, see section 1.2. Experimentally, we evaluated the expression (1.25), with the definitions (1.26), from the number of coincidences $N(\mathrm{E},\mathrm{E})$, $N(\mathrm{E},\mathrm{O})$, $N(\mathrm{O},\mathrm{E})$ and $N(\mathrm{O},\mathrm{O})$ simultaneously registered for each combination of outputs, and with parameters x_i and y_j deterministically and sequentially selected —after loss equalization and scans at optimal amplitudes. Our results are shown in table 3.3. The CHSH inequality is violated by more than 40 standard deviations. Although noise is subtracted, the theoretical optimum is not attained due to other experimental imperfections, mainly limited visibility, see section 2.6.

Table 3.3: CHSH Bell inequality violation results. The first column corresponds to the optimal settings, $x_i = (a_i, \alpha_i)$, $y_j = (b_j, \beta_j)$, $i, j \in \{0, 1\}$. Second and third columns are theoretical predictions and experimental results (with statistical uncertainties), respectively. Data from [OWPH$^+$14].

	Theory	Experiment
$x_0\, y_0$	0.796	0.764 ± 0.002
$x_0\, y_1$	0.796	0.698 ± 0.002
$x_1\, y_0$	0.796	0.714 ± 0.002
$x_1\, y_1$	-0.178	-0.158 ± 0.002
S	2.566	2.334 ± 0.008

The violation of the CHSH inequality is realized by simultaneously measuring all coincidence probabilities, so that no further assumption is needed for the Bell test, contrary to the CH74 inequality case. We should however mention that the above results do not provide a decisive test of local causality as we have not closed either the detection or locality loopholes. Nevertheless, our results show that our approach allows the study of quantum correlations of frequency-entangled photons, and could in principle, i.e. if experimental imperfections (mainly losses and detector inefficiencies) were small, be adapted to permit a decisive test of local causality. From an applied perspective, even imperfect Bell tests have become a standard way to evaluate experimental methods. In our case, estimation of the Bell parameter requires a fine tuning of the RF parameters and high stability of the photon-pair source. Violations of Bell inequalities are further evidence of the efficiency of frequency-bin entanglement.

3.2 Plasmon-assisted transmission

Plasmonics forms a major part of nanophotonics, which explores how electromagnetic fields can be confined over dimensions on the order of or smaller than the wavelength. Light-matter interaction probed at the nanoscale attracts much attention nowadays, both for its fundamental interest and potential applications, including all-integrated optics [BDE03]. Localized surface plasmon polaritons (LSPPs) and surface plasmon polaritons (SPPs) are electromagnetic excitations coupled to electron charge density waves, localized on metallic nanostructures and metal-dielectric interfaces, respectively. The presence of LSPPs or SPPs allows confinement of light on scales far below that of conventional optics. Quantum plasmonics is a growing field studying interactions between quantum light fields and plasmonic excitations. This research could lead to new classes of quantum devices, such as single-photon sources, transistors and ultra-compact circuitry at the nanoscale [JS11, Jac12, TMÖ$^+$13]. Fundamental studies explore a "mesoscopic" physics, a unique quantum state being coherently carried by billions of electrons.

Transmission through metallic nanostructures cannot be accounted for by classical diffraction theory. Such structures allow conversion of photons into surface plasmons which tunnel through the structure before reradiating as photons [ELG$^+$98, MMGVL$^+$01]. This light-matter interaction preserves quantum coherence: an important finding was the discovery that entanglement survives during interaction of entangled photons with metallic nanostructures. This has been investigated with polarization [AVEW02, MGVE$^+$04], time-bin [FRM$^+$05] and orbital angular-momentum [RGH$^+$06] entanglement. Recent works include single-particle and double-particle interference experiments —such as demonstration of the Hong–Ou–Mandel effect— with plasmons, demonstrating the quantum bosonic nature of plasmonic excitations [SKD$^+$05, FHGZ06, AMY$^+$07, KGB$^+$09, HSL$^+$09, GTMCM$^+$11, DMSKC$^+$12, HKZ13, DGA14, FLKA14, Ste14, DMST$^+$14, CLR$^+$14].

We studied the interactions of frequency-bin entangled photons with different nanostructures: gold nano-pillars fabricated by nanocoating lithography [FTK06, KF09, KF10], and hybrid structures [UKC$^+$13]. By combining a continuous metal film and a dielectric photonic crystal, these "plasmonic waveguides" support both LSPPs and SPPs, allowing to control the interplay between them. Plasmo-photonic two-dimensional crystals exhibit a complex resonance pattern, which can be characterized using both numerical simulations and measurements of the electric near-field patterns. Photon-plasmon coupling is strongly increased if overlapping (plasmonic-photonic) resonances exist. This allows investigation of the effect of resonances on photon-matter interaction. Specifically, we address two pivotal questions. First, in which cases and to what extent frequency-bin entanglement survives when a photon is subject to a plasmonic conversion? Second, could plasmonic structure and nature of its resonance pattern affect the efficiency of the conversion process?

Our experimental setup is depicted in figure 3.1. Frequency-entangled photons are separately modulated by EOPMs, and detected in a given frequency bin after selection by a narrow-band frequency filter. We used components described in section 2.5. In the present experiment, the laser at 776.04 nm pumps the Brussels PPLN, and Acreo FBGs are aligned on the degeneracy wavelength 1552.08 nm. The EOPMs are driven by 25-GHz signals generated by the fully-automated RF setup. Amplitudes were chosen close to the value $a = b \approx 1.2$, so that scans of phase $\alpha - \beta$ should lead to a cancellation of the two-photon coincidence rate (2.40). This allows to evaluate the (net) visibility (2.62), which is our benchmark for the quality of the entanglement. In the present setup, before being phase modulated, one of the photons is coupled out its fiber and sent through a plasmonic nanostructure before being coupled again into a fiber. Evaluation of the visibility of the interference pattern in the presence of a plasmonic conversion allows to quantitatively estimate the preservation or degradation of frequency-bin

entanglement in the process.

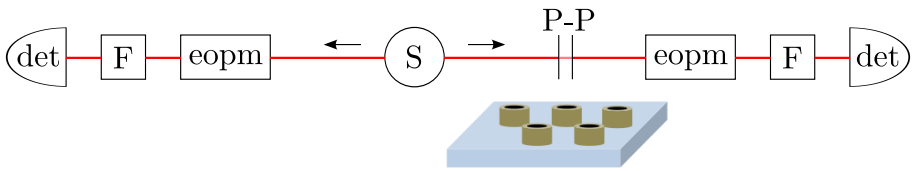

Figure 3.1: Experimental setup for plasmon-assisted transmission of entangled photons. As described in chapter 2, a source S, consisting of a laser pumping a nonlinear waveguide, generates frequency-entangled photons in the telecommunication C-band. The photons, directed through distinct optical fibers, are separately manipulated by EOPMs. Narrow-band frequency filters F select photons belonging to a specific frequency bin, which are detected by single-photon detectors. The joint statistics exhibits a two-photon interference pattern in the frequency domain, obtained by varying the parameters (a, α) and (b, β) of the radio-frequency signals driving the EOPMs. The originality of the present setup is that, before being phase modulated, one of the photons is coupled out its fiber and sent through a plasmonic nanostructure P–P before being coupled again into a fiber. The inset depicts a gold nano-pillar structure used in the experiment (rotated so as to be placed transversally to the light beam). The pillar width and height are 200 nm and the pitch between each nano-pillar is 460 nm.

Plasmonics suffers from intrinsic losses. Compared to the case where no sample is present —allowing calibration of the experiment— insertion of a sample tends to diminish the coincidence rate and coincidence-to-accidental ratio (CAR). However observed coincidence rates (typically $\sim$ Hz) are consistent with the samples' transmission values measured with classical light. Moreover, figure 3.2, presenting coincidence peaks obtained after transfer of a photon through a gold sample, shows the role of the plasmonic conversion process. With a nanostructure, the coincidence rate and CAR dramatically increase compared to the case where no nanostructure is present. This is due to the transmission-enhancement originating from the photon-plasmon-photon conversion process.

Coincidence rates and CARs are loss-dependent. To investigate whether frequency-bin entanglement is preserved when a photon is transferred through a plasmonic nanostructure, we evaluated the visibility of two-photon interference patterns —in good agreement with the theoretical prediction (2.40)— extracted from coincidence measurements. Our results, which will be detailed in a future publication, provide strong evidence that frequency-bin entangled photons can propagate through these plasmo-photonic nanostructures. Taking into account the loss-dependent background noise, no degradation of the (net) visibility is observed for all tested samples. Our measurements clearly show the robustness of frequency-bin entanglement, which survives after interactions with the plasmo-photonic structures, offering possibilities for a variety of applications in which quantum states can be encoded into the collective motion of a many-body electronic system without demolishing their quantum nature.

3.3 Quantum key distribution

As we have seen in section 1.3, ultra-secure communication can be achieved with quantum key distribution (QKD). Due to the equivalence between prepare-and-measure and entanglement-based schemes, QKD can be implemented with serial manipulation of single photons or parallel manipulation of entangled photons. The most used platforms are polarization and time-bin

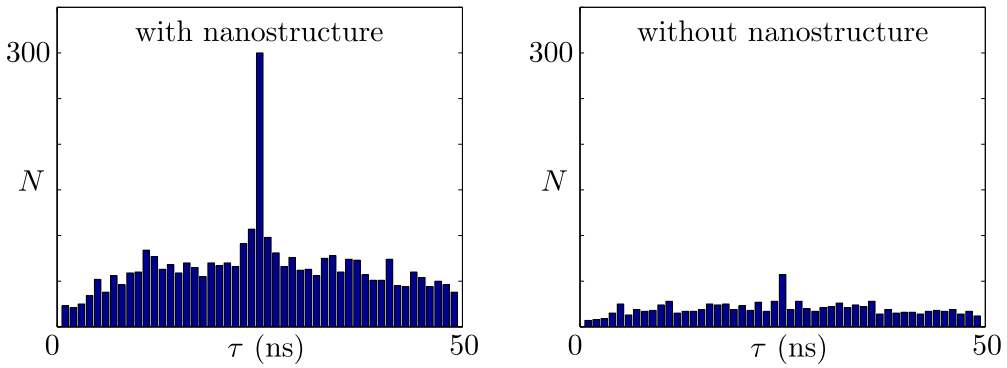

Figure 3.2: Coincidence peaks obtained after transfer of a photon through a gold sample. Acquisition time is 5 minutes for each panel. The samples corresponding to the left and right measurements had the same thickness and were used in the same experimental conditions described by figure 3.1. While the right sample was constituted of pure gold, a nanostructure was present on the left sample. The enhanced coincidence rate and coincidence-to-accidental ratio for the left sample are signatures of the huge transmission enhancement due to plasmonic processes, the vast majority of analyzed photons having indeed been subject to such a plasmonic conversion.

encoding. The conceptual parallel between time bins and frequency bins suggests that, instead of coding information in the relative phase of time bins, one could code information in the relative phase of frequency bins. Here we present potential implementations of the BB84 protocol based on electro-optic phase modulation of single photons. We consider prepare-and-measure schemes, in which Alice encodes information in the state of a single photon, and Bob decodes the information at the reception of the photon. We start by describing the implementation proposed by Matthieu BLOCH, Steven W. MCLAUGHLIN, Jean-Marc MEROLLA and Frédéric PATOIS in [BMMP07].

3.3.1 The Bloch–McLaughlin–Merolla–Patois implementation

We follow the description made in [BMMP07]. A monochromatic single-photon source emits photons in the frequency state $|0\rangle$, adopting the discretized notation of (2.22). After sine phase modulation with parameters (a, α), so as to obtain the state $\sum_n J_n(a)\mathrm{e}^{\mathrm{i}n\alpha}|n\rangle$, a narrow-band frequency filter selects only frequency bins -1, 0 and 1, yielding the state

$$|\psi\rangle = \frac{J_0(a)|0\rangle + J_1(a)\mathrm{e}^{\mathrm{i}\alpha}|1\rangle + J_{-1}(a)\mathrm{e}^{-\mathrm{i}\alpha}|-1\rangle}{\sqrt{J_0^2(a) + 2J_1^2(a)}}\,, \tag{3.10}$$

produced with efficiency $\eta(a) = J_0^2(a) + 2J_1^2(a)$, all the components being supposed ideal. In this three-dimensional Hilbert space, one can identify the states

$$|0_{b0}\rangle = |0\rangle \quad \text{and} \quad |1_{b0}\rangle = \frac{1}{\sqrt{2}}\big(|1\rangle - |-1\rangle\big)\,, \tag{3.11}$$

$$|0_{b1}\rangle = \frac{1}{\sqrt{2}}\big[|0\rangle + \frac{1}{\sqrt{2}}\big(|1\rangle - |-1\rangle\big)\big] \quad \text{and} \quad |1_{b1}\rangle = \frac{1}{\sqrt{2}}\big[|0\rangle - \frac{1}{\sqrt{2}}\big(|1\rangle - |-1\rangle\big)\big]\,, \tag{3.12}$$

to the BB84 states (1.42) and (1.43). The maximally conjugated bases $b0$ and $b1$ of the same two-dimensional subspace are suitable for the implementation of the BB84 protocol. To produce

these states, Alice uses the following RF parameters: amplitudes $a(0_{b0}) = 0$, $a(1_{b0}) \equiv a_0 \approx 2.405$, $a(0_{b1}) = a(1_{b1}) \equiv a_1 \approx 1.161$, such that $J_0(a_0) = 0$ and $J_0(a_1) = \sqrt{2}J_1(a_1)$, with phases $\alpha(1_{b0}) = \alpha(0_{b1}) = 0$ and $\alpha(1_{b1}) = \pi$. The states are thus produced with efficiency

$$\eta(0_{b0}) = 1\,, \qquad \eta(1_{b0}) = J_0^2(a_0) + 2J_1^2(a_0) \approx 0.539\,, \tag{3.13}$$

$$\eta(0_{b1}) = \eta(1_{b1}) = J_0^2(a_1) + 2J_1^2(a_1) \approx 0.953\,. \tag{3.14}$$

To generate the four states with equal probability, Alice must proceed to a biased random selection, producing states $|0_{b0}\rangle$, $|1_{b0}\rangle$, $|0_{b1}\rangle$ and $|1_{b1}\rangle$ with respective probabilities 0.202, 0.374, 0.212 and 0.212, so that the total encoding efficiency is 0.808.

At the reception, Bob modulates (with a sine signal at the same radio-frequency) the phase of the photon with parameters (b, β), and uses a narrow-band filter distinguishing between the frequency bin "0" and the others. Both outputs are followed by single-photon detectors, which we denote by D_+ (associated to the frequency bin "0") and D_-. The choice $b = 0$ allows perfect discrimination of states $|0_{b0}\rangle$ and $|1_{b0}\rangle$, while states $|0_{b1}\rangle$ and $|1_{b1}\rangle$ lead to random results. To implement the measurement in basis $b1$, Bob selects the parameters $(b, \beta) = (a_1, 0)$. The state $|0_{b1}\rangle$ will always give rise to detection events in detector D_- and never in detector D_+, i.e. $P(D_-|0_{b1}) = 1 - P(D_+|0_{b1}) = 1$, but the state $|1_{b1}\rangle$ will not be discriminated perfectly: $P(D_+|1_{b1}) = 1 - P(D_-|1_{b1}) = 0.953 < 1$. Erroneous detections increase the quantum bit-error rate (QBER) by approximately 1.2%. As stated in [BMMP07], if we reasonably assume that Eve does not control Bob's receiver, Bob's nonperfect measurements do not create a security loophole. Still, the increase in QBER has to be accounted for when distilling the secret key, which slightly reduces the key rate and transmission distance. An experimental proof-of-principle of the feasibility of the setup, using attenuated coherent states and FBGs, was exhibited in [BMMP07].

3.3.2 An alternative implementation

We again consider that Alice prepares four states for the BB84 protocol, noted for clarity of notations in this section $|a_0, \alpha_0\rangle$, $|a_1, \alpha_1\rangle$ (first basis) and $|b_0, \beta_0\rangle$, $|b_1, \beta_1\rangle$ (second basis). However, now, Alice does not apply any filtration: she sends directly to Bob the four states, obtained with a sine-modulating signal of parameters (c, γ) equal to (a_0, α_0), (a_1, α_1), (b_0, β_0) or (b_1, β_1):

$$|c, \gamma\rangle \equiv \sum_n J_n(c) \mathrm{e}^{\mathrm{i}n\gamma} |n\rangle\,. \tag{3.15}$$

Such states lie in a high-dimensional Hilbert space and cannot be identified with the traditional BB84 states. To evaluate if they are suitable for the protocol, a "basis overlap" angle θ is defined:

$$\sqrt{1 + |\sin\theta|} = \frac{1}{2}\big|\langle a_0, \alpha_0|b_0, \beta_0\rangle + \langle a_0, \alpha_0|b_1, \beta_1\rangle + \langle a_1, \alpha_1|b_0, \beta_0\rangle - \langle a_1, \alpha_1|b_1, \beta_1\rangle\big|\,. \tag{3.16}$$

The parameter θ evaluates the "non-orthonality" of the states used. Security proofs of the BB84 protocol against classes of collective attacks depend on the value of θ and the bit error rate δ, see details in [Woo13]. For maximally conjugated bases, $\theta = \pi/2$, and the asymptotic key rate $r \to 1$ when $\delta \to 0$, while $r \to 0$ when $\delta \to 11\%$. The parameter

$$S = \langle a_0, \alpha_0|b_0, \beta_0\rangle + \langle a_0, \alpha_0|b_1, \beta_1\rangle + \langle a_1, \alpha_1|b_0, \beta_0\rangle - \langle a_1, \alpha_1|b_1, \beta_1\rangle \tag{3.17}$$

has to be greater than 2 to guarantee a rate $r > 0$, with $r \to 1$ for $S = 2\sqrt{2}$. Our goal is thus to maximize the expression (3.17) by using states of the form (3.15). Since

$$\langle a, \alpha|b, \beta\rangle = \langle p| \sum_p \sum_q J_p(a) \mathrm{e}^{-\mathrm{i}p\alpha} J_q(b) \mathrm{e}^{\mathrm{i}q\beta} |q\rangle = \sum_p J_p(a) J_q(b) \mathrm{e}^{\mathrm{i}p(\beta-\alpha)} = J_0(C)\,, \tag{3.18}$$

with

$$C^2 = a^2 + b^2 - 2ab\cos(\alpha - \beta)\,, \tag{3.19}$$

the expression (3.17) takes the form:

$$S = J_0(C_{00}) + J_0(C_{01}) + J_0(C_{10}) - J_0(C_{11})\,. \tag{3.20}$$

We must maximize the parameter S under constraints

$$C_{ij}^2 = a_i^2 + b_j^2 - 2a_i b_j \cos(\alpha_i - \beta_j) \quad \text{and} \quad J_0(C_a) = J_0(C_b) = 0\,, \tag{3.21}$$

where $C_a^2 = a_0^2 + a_1^2 - 2a_0a_1\cos(\alpha_0 - \alpha_1)$ and $C_b^2 = b_0^2 + b_1^2 - 2b_0b_1\cos(\beta_0 - \beta_1)$, so that we have: $\langle a_0, \alpha_0 | a_1, \alpha_1\rangle = \langle b_0, \beta_0 | b_1, \beta_1\rangle = 0$. We denoted the quantity (3.17) S to highlight the similarity with Bell optimizations described in section 3.1. Again, the parameters C_{ij} can be identified to the lengths of the sides of a quadrilateral, as represented in figure 3.3. As shown in [Jot14], an analytical optimization taking into account the additional constraints for parameters C_a and C_b leads to a value $S \approx 2.470$ for $C_{00} = 1.5322$, $C_{01} = C_{10} = 0.8726$ and $C_{11} = 3.2775$. A corresponding set of RF parameters is given by: $a_0 = b_0 = 0.7661$, $a_1 = b_1 = 1.6387$, $\alpha_0 = \beta_1 = 0$, and $\alpha_1 = \beta_0 = \pi$.

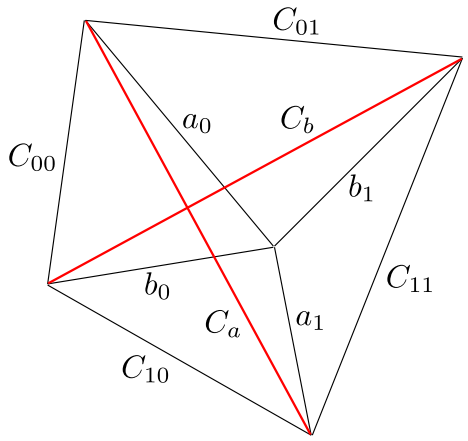

Figure 3.3: Graphical representation of the optimization under constraints. The red segments represent the parameters C_a and C_b whose value must ensure that $\langle a_0, \alpha_0 | a_1, \alpha_1\rangle = \langle b_0, \beta_0 | b_1, \beta_1\rangle = 0$. Figure adapted from [Jot14].

Bob implements his two measurement bases with his own EOPM, driven with parameters equal to, e.g., (a_0, α_0) and (b_0, β_0). When he chooses the correct basis, a narrow-band filter discriminating between the frequency bin 0 and the other frequencies allows a perfect discrimination of the states. Due to the non-perfect "basis overlap" ($\theta = 31.7°$), measurements of states in the wrong basis do not give perfectly random results, which will decrease the secret-key rate. In the ideal case where no errors are present, the bound is calculated to be $r \to 0.2093$, while $r \to 0$ for error values $\delta \approx 1\%$ only. We should mention however that the bound on r is not guaranteed to be optimal, as can be seen with the low value of r even when no error is present.

A proof-of-principle experiment has been conducted in the context of a master thesis [Jot14]. The setup is illustrated in 3.4. The results showed that the states were produced and manipulated with precision, but the measurements were too noisy to extract a secret key, in view of the very bad noise tolerance of the implementation.

3.4 Discussion

Our experimental methods are relatively straightforwardly adaptable to field experiments, such as long-distance Bell inequality violation, QKD and other quantum communication pro-

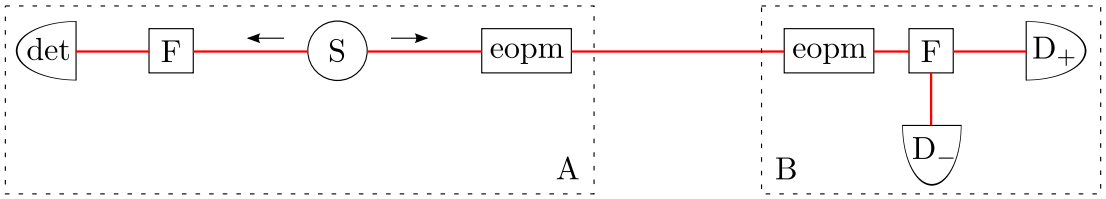

Figure 3.4: Experimental setup for quantum key distribution with frequency bins. A source S generates frequency-entangled photons. The detection of a photon at frequency ω_0 heralds the production of a photon at frequency ω_0. Alice modulates the photon with randomly chosen parameters and sends it to Bob, which implements a measurement in two different bases with his own EOPM.

tocols. However, if one wants to realize long-distance experiments, one must consider the effect of dispersion. If a photon of frequency ω propagates a distance L, its state is transformed according to

$$|\omega\rangle \mapsto \mathrm{e}^{\mathrm{i}k(\omega)L}|\omega\rangle \simeq \mathrm{e}^{\mathrm{i}(\beta_0+\beta_1(\omega-\omega_0)+\beta_2/2(\omega-\omega_0)^2+\beta_3/6(\omega-\omega_0)^{3\cdots})L}|\omega\rangle\,, \tag{3.22}$$

where we have developed the wave number k in series in $\omega-\omega_0$. When considering frequency coding of information, the zeroth order term $\mathrm{e}^{\mathrm{i}\beta_0 L}$ is an overall phase, and has no physical influence. The first order term $\mathrm{e}^{\mathrm{i}\beta_1(\omega-\omega_0)L}$ can be absorbed into the phase γ of the RF field applied to the EOPM. In all calculations as well as the analysis of the experiments we absorb the phases $\mathrm{e}^{\mathrm{i}\beta_1(\omega-\omega_0)L}$ into the phases of the RF fields.

The fact that phases accumulated during propagation can be absorbed into the phases of the RF fields underlies the inherent high stability of experiments using frequency bins. Indeed stability of our experimental setup requires that $\beta_1\Omega_{\mathrm{RF}}L \ll 1$ (since the only frequencies that interfere are those separated by small multiples of Ω_{RF}). This should be contrasted with interference experiments in the spatial domain, where one is sensitive to the phase $\beta_0 L$. Approximate equality of the phase and group velocities implies that $\beta_0 \simeq \beta_1\omega_0$. Since $\Omega_{\mathrm{RF}}/\omega_0 \simeq 10^{-4}$, our experiments are less sensitive to changes in fiber lengths by a factor of roughly 10^{-4}. This implies that in laboratory experiments, no stabilization is required. In field experiments, however, where propagation distances are tens of kilometers, the local RF oscillators must be synchronized.

It should be noted that the equivalence of figures 2.4 and 2.5, described by equations (2.27) and (2.40), holds only when neglecting the effect of dispersion. The phases accumulated in the two experiments are not the same, which causes an horizontal shift of the interference patterns, since the accumulated phase has to be absorbed into the phases of the RF fields. A problem is that the higher order terms in (3.22) due to frequency dispersion cannot be absorbed in the phase γ of the RF field. This modification of the coefficients $c_d(a,\alpha;b,\beta)$ cannot be neglected for long-distance and/or broad-spectrum applications.

In particular, the interleaver approach allows one in principle to manipulate and measure frequency-entangled photons produced by a broadband source with low spectral brightness, as the interleavers that separate the even and odd frequencies act over a very broad bandwidth. This, however, requires dispersion compensation, as otherwise photons with different detunings exhibit different interference patterns that average to zero over the bandwidth of the photons —even in laboratory conditions.

We note that if dispersion may degrade the quality of interferences in certain cases, it could also be beneficial for discriminating the frequency bins in an analysis setup without frequency filters.

An important route would be to generalize the accessible unitary transformations. The class of unitary transformations explored in this work, defined by (2.21), is somewhat limited. For example, the use of non-sinusoidal voltages would give rise to much more general families of unitary transformations $|0\rangle \mapsto \sum_n f_n(c)\mathrm{e}^{\mathrm{i}n\gamma}|n\rangle$, where f_n are the Fourier coefficients of the considered voltage. For instance, sawtooth signals allow a deterministic frequency translation.

A lot of experiments could benefit from a more general transformation. In particular, it would allow a better exploitation of the high dimensionality. High-dimensional entanglement has been studied in a number of experiments, see e.g. [SS94, BLPK05, VWZ02, TAZG04, DRMS$^+$04, OMV$^+$05, vELDW07, DLB$^+$11]. High-dimensional QKD [BPT00, AKBH07] allows to establish a key at a potentially higher rate than that afforded by standard, two-dimensional QKD protocols: more than one bit of information can be generated when a single photon is detected. QKD protocols better suited than BB84 to frequency-bin entanglement and Bell inequalities adapted to high dimensions, such as the CGLMP inequality [CGL$^+$02], should be explored. The fact that an EOPM acts as a high-dimensional frequency beam splitter suggests high-dimensional frequency experiments analogue to two-dimensional spatial experiments, such as a Hong–Ou–Mandel experiment. Let mention also that the conjugate use of two photon-pair sources with EOPMs and narrow-band frequency filters would allow an entanglement swapping experiment with frequency-bin entangled photons.

Chapter 4

Silicon-on-insulator integrated source of polarization-entangled photons

Throughout this chapter, we follow very closely reference [OSC+13]. We report the experimental generation of polarization-entangled photons at telecommunication wavelengths using spontaneous four-wave mixing in silicon-on-insulator (SOI) wire waveguides. The key component is a two-dimensional coupler that transforms path entanglement into polarization entanglement at the output of the device. Using quantum state tomography we find that the produced state has fidelity 88% with a pure nonmaximally entangled state, and violates the CHSH Bell inequality by $S = 2.37 \pm 0.19$.

4.1 Silicon-on-insulator platform

Polarization constitutes one of the degrees of freedom most often used in quantum information. It is not the most adapted degree of freedom for long-distance fiber-optic implementations, but demonstration of polarization entanglement at telecommunication wavelengths remains attractive. High-quality polarization-entangled photon-pair sources have been reported based on both $\chi^{(2)}$ [KMW+95, FNM+07, MIH+10] and $\chi^{(3)}$ nonlinear processes [TI04, LVSK05]. In a $\chi^{(3)}$ medium, four-wave mixing involves two photons of a pump field at frequency ω_0, which annihilate and create signal and idler photons at frequencies $\omega_{s,i} = \omega_0 \pm \omega$ (therefore also producing frequency-entangled states of the form (2.28)).

To minimize cost and footprint, recent work focuses on the integration of such sources. Various platforms are investigated. The SOI platform, based on reliable and low-cost complementary metal–oxyde–semiconductor (CMOS) technology, is a promising avenue for integrated photon-pair sources based on spontaneous four-wave mixing, both in straight wire waveguides [SLF+06] and in ring resonators [CPHB+09]. Advantages of the SOI platform are: mechanical stability, great optical confinement, compatibility with fabrication procedures used in micro-electronics (CMOS), and relatively high nonlinearity [CME10]. An extensive description of light propagation in silicon waveguides and a discussion of quantum optics uses of SOI can be found in [CME10]. Here we build on the work done by Stéphane CLEMMEN, using his experimental methods and a chip conceived by him [CME10].

Earlier studies [Tak12] reported time-bin entanglement [TTF+07, HTF+08] and polarization entanglement based either on a nonintegrated polarizing beam splitter [TFT+08] or on a polarization rotator sandwiched between two nonlinear silicon wire waveguides [MLJF+12]. Here

we present an SOI integrated source of polarization-entangled photons in which two nanophotonic waveguides produce path entanglement that is subsequently converted at the output of the chip into polarization entanglement using a two-dimensional grating coupler. This is analogous to previous bulk or fiber optics experiments, such as [FAO+07]. We characterize the source using two-photon interferences, quantum state tomography, and Bell inequality violation.

4.2 Experimental setup

Our experiment, based on the setup of figure 1.7, is depicted in figure 4.1. Our goal is to produce a quantum superposition of the type $(|HH\rangle + |VV\rangle)/\sqrt{2}$, corresponding to a Bell state in polarization, see chapter 1. The source and the analysis and detection parts are made of non-integrated fiber components. Polarization entanglement is produced at the interface between the SOI chip and an optical fiber. On the chip, the pump beam is split into different waveguides, coherently producing photon pairs in each waveguide, therefore generating path entanglement. Combination of the fluxes on a two-dimensional grating coupler which sends photons in the same fiber but with orthogonal polarizations [TCB+03] converts it to polarization entanglement —which could also be converted in another type of entanglement.

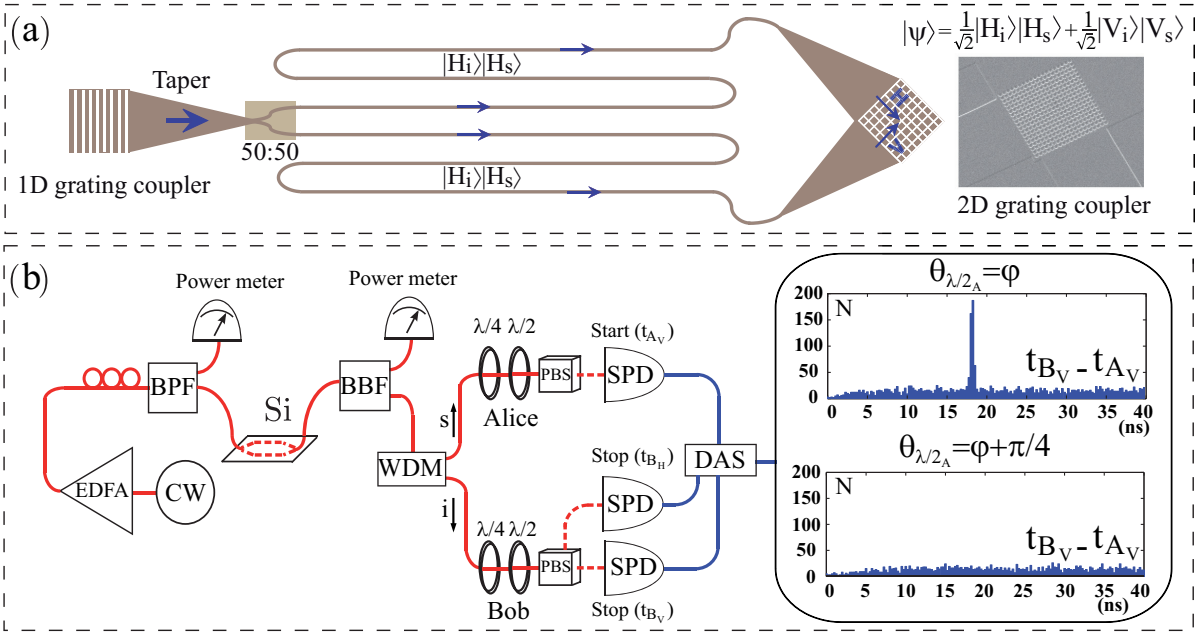

Figure 4.1: Experiment for producing and analyzing polarization-entangled photons. (a) Schematic of the SOI chip producing polarization-entangled photon pairs. The pump power is split into two waveguides which are recombined at the output of the chip with a two-dimensional grating coupler. Inset: SEM image of the two-dimensional grating coupler. (b) Experimental setup for generating and measuring polarization-entangled photons. See text for a detailed description. Insets show typical results for constructive and destructive interference. Each time bin in the histograms is 250 ps long. Figure from [OSC+13].

Our SOI source was fabricated by the ePIXfab at IMEC with 193 nm deep UV lithography. A pump beam is coupled into the structure using a one-dimensional grating coupler followed by a taper [CME10]. A 50/50 multimode coupler [BSD+10] then splits the light into two sil-

icon wire waveguides. The waveguides have transverse dimension 500 nm $\times$ 220 nm and length 15 mm. At the operating wavelength (telecommunication C-band) the waveguides are monomode and guide only TE (horizontal) polarization.

Four-wave mixing in the waveguides leads to photon-pair production, and hence to the state $a'|H_{s1}\rangle|H_{i1}\rangle + b'|H_{s2}\rangle|H_{i2}\rangle$, where s, i refer to signal and idler frequencies, $1, 2$ refer to the first and second waveguides, and we have indicated that the polarization is horizontal. The coefficients a' and b' take into account possible deviations from a perfect $50/50$ coupler, or different losses in the two waveguides. The light propagating in the waveguides is coupled into an optical fiber using inverted tapers [CME10] and a 2D grating coupler [TCB$^+$03], see figure 4.1(a). Two-dimensional grating couplers enable polarization-insensitive SOI structures, as they couple the two orthogonal polarizations propagating in an optical fiber to the two TE modes propagating in two distinct silicon waveguides. They can provide an extinction ratio between both polarizations higher than 18 dB [TCB$^+$03]. In our case the 2D grating coupler converts path entanglement into polarization entanglement. The state in the optical fiber is thus

$$|\Psi(a,b)\rangle = a|H_s\rangle|H_i\rangle + b|V_s\rangle|V_i\rangle\,, \tag{4.1}$$

where the new coefficients a, b take into account possible polarization-dependent losses of the 2D grating coupler.

The experimental setup is depicted in figure 4.1(b). A 1-mW continuous-wave laser at 1539.6 nm (Agilent) is amplified to 7 mW with an erbium-doped fiber amplifier (EDFA) and then spectrally filtered by a bandpass filter (BPF). Injection and extraction losses are both approximately equal to 6 dB, and losses in each arm of the structure are close to 3 dB. The 1.75 mW power on chip is divided in both device arms. The output containing the transmitted pump and entangled photons is collected by a cleaved nonpolarization-maintaining standard telecommunication fiber (SMF) and passes through a band-block filter (BBF) —with an isolation of more than 110 dB, see [CME10]— to reject the pump, and a wavelength division multiplexer (WDM) to separate signal (s) and idler (i) photons into two different fiber channels, which are sent to Alice's (A) and Bob's (B) stations. The signal and idler ports are centered at 1530 and 1550 nm, respectively, with a bandwidth of 20 nm. The characteristics of the filtration system are described in [CME10].

Alice and Bob locally and independently analyze their photons using a free-space analyzer consisting of a quarter-wave plate (QWP $\lambda/4$), a half-wave plate (HWP $\lambda/2$), and a polarizing beam splitter (PBS). Only one output of Alice's PBS —corresponding to the vertical polarization component— is available, while both outputs of Bob's PBS are available. The photons emerging from the three outputs are directed to superconducting single-photon detectors (SSPDs, from Scontel, efficiency $\approx 5\%$, dark-count rate ≈ 10 Hz including straight light, time resolution ≈ 50 ps, see section 2.5). There is roughly 20 m of standard non-polarization maintaining single-mode telecommunication optical fiber (SMF) from the chip to the analyzers. Total losses from after ejection to the detectors are estimated at 3.6 dB for Alice, and 5.5 and 6.8 dB for Bob's two channels.

Electronic signals from the SSPDs are directed to a data acquisition system (DAS) consisting of a time-to-digital converter (Agilent Acqiris, time resolution ≈ 50 ps, see section 2.5) connected to a computer. The DAS records the relative times $t_{\mathrm{B}_V} - t_{\mathrm{A}_V}$ and $t_{\mathrm{B}_H} - t_{\mathrm{A}_V}$ between Alice's and Bob's detections and generates a histogram of these events.

When correlated photons are present, a coincidence peak emerges from these time-resolved measurements. The illustrative histograms (inset of figure 4.1) provide examples of constructive and destructive interference. Data acquisition and treatment are entirely automated (see section 2.5). However, in this experiment, a manual adjustment of the analyzers' settings is required.

4.3 Experimental results

To quantitatively analyze the results, we use the raw and net numbers of coincident events defined by (2.57), (2.58) and (2.59), with $t = t_{B_V} - t_{A_V}$ or $t = t_{B_H} - t_{A_V}$. The time window for the signal has size $t_f - t_i = 0.8$ ns.

From these quantities we deduce that in the case of constructive interference, coincidences are measured at a rate $\approx$ 0.4 Hz and the coincidence-to-accidental ratio is approximately equal to 8. This rather low value (which could be increased by using resonators or filters) is due to the continuous-wave operation —which increases the effect of the intrinsic noise of SOI waveguides [CPS+12]— and to the high losses from chip to detector. Dark counts are almost negligible due to the use of superconducting detectors. We carefully attached the fibers to guarantee stable injection and ejection and avoid polarization drift, so that no active power nor polarization stabilization is required, and measurements are repeatable for several hours. This has been finely characterized with automated calibration measurements.

Results of two-photon interference measurements are presented in figure 4.2. Coincidence rates are plotted as a function of the angle of Alice's half-wave plate. Note that because no polarization management is performed before the analyzers, all phase plate angles must be adjusted to get a good contrast.

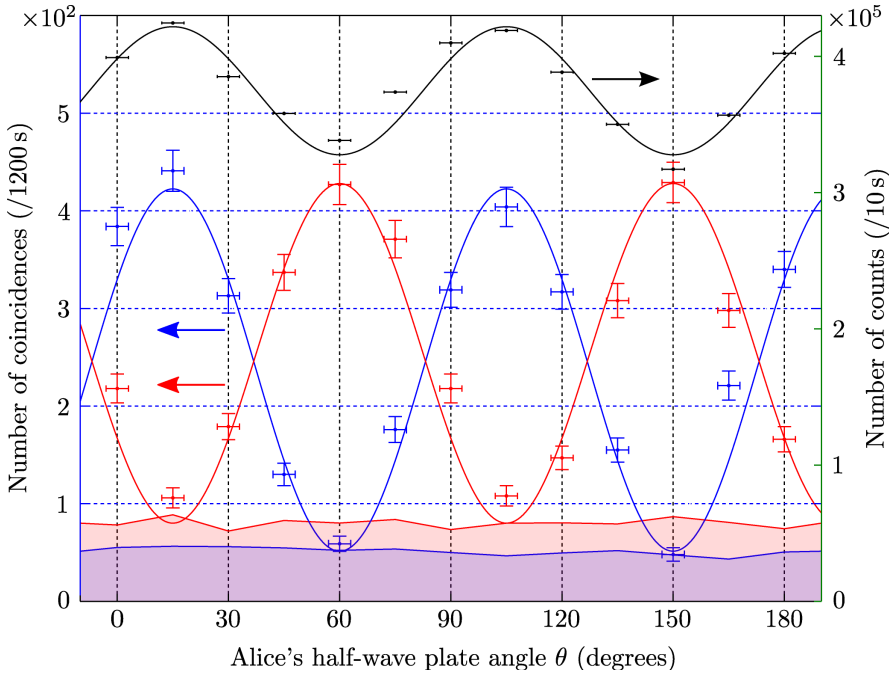

Figure 4.2: Interference of polarization-entangled photons from an SOI chip. Horizontal axis is the angle θ of Alice's half-wave plate, on which a precision of $\pm 3°$ is assumed. Left vertical axis is the number of coincidences between Alice's and Bob's detectors registered during 20 minutes. Symbols are experimental results with statistical error bars, while curves are sinusoidal fits assuming a perfect net visibility. Shaded regions correspond to measured accidental coincidence rates. The blue and red curves (bottom curves) correspond to $A_V B_V$ and $A_V B_H$ coincidences, respectively. The black curve (top curve) is the single-photon rate of Alice's detector as a function of θ. The right vertical axis is the total number of counts registered by Alice's detector in 10 s. Figure from [OSC+13].

Because of noise, raw visibilities are limited to approximately 80% (vertical component) and

60% (horizontal component), while net visibilities reach 99% and 90%, respectively. We also measured the single-photon rate detected by Alice. The fact that this curve is not perfectly flat is evidence that the produced state is not maximally entangled. This is presumably due to imperfect on-chip optical components. However, the limited visibility (≈12%) shows that the produced state is not far from a maximally entangled state. We note that nonmaximally entangled states have specific applications that are not accessible to maximally entangled states, see e.g. [Har93] and [GMR+13].

In order to accurately characterize the produced state we performed a standard quantum state tomography analysis. We followed the maximum likelihood method described in [JKMW01] (being careful of errors therein) to evaluate the "most probable" density matrix given the statistics of coincident events measured in the sixteen different configurations of the analyzers given in table 1.2.

The reconstructed density matrix $\rho_{\mathrm{AB}}^{(\mathrm{out})}$ is then re-expressed as

$$\rho_{\mathrm{AB}}^{(\mathrm{out})} = \left(J_{\mathrm{A}} \otimes J_{\mathrm{B}}\right) \rho_{\mathrm{AB}}^{(\mathrm{in})} \left(J_{\mathrm{A}}^{\dagger} \otimes J_{\mathrm{B}}^{\dagger}\right). \tag{4.2}$$

We numerically optimized the parameters of the Jones matrices J_{A} and J_{B} as well as the real numbers a, b (with $a^2 + b^2 = 1$) in order to maximize the fidelity

$$F\left(\rho_{\mathrm{AB}}^{(\mathrm{in})} \cdot \rho_{\mathrm{AB}}^{(\mathrm{target})}\right) = \left(\mathrm{Tr}\left[\left(\sqrt{\rho_{\mathrm{AB}}^{(\mathrm{in})}}\rho_{\mathrm{AB}}^{(\mathrm{target})}\sqrt{\rho_{\mathrm{AB}}^{(\mathrm{in})}}\right)^{1/2}\right]\right)^2, \tag{4.3}$$

where $\rho_{\mathrm{AB}}^{(\mathrm{target})} = |\Psi(a,b)\rangle\langle\Psi(a,b)|$ is the density matrix of the pure nonmaximally entangled state (4.1). Thus, $\rho_{\mathrm{AB}}^{(\mathrm{in})}$ is our reconstruction of the state at the output of the SOI chip, and J_{A}, J_{B} our reconstruction of the polarization rotation undergone by A and B photons between the chip and the analyzers.

The results of this analysis are presented in figure 4.3. The reconstructed density matrix $\rho_{\mathrm{AB}}^{(\mathrm{in})}$ has a fidelity of 88% (which drops to 71% when noise is not subtracted) with the target state, with $a^2 \approx 0.6$ and $b^2 \approx 0.4$, consistently with our single-photon interference measurements. The fidelity to a maximally entangled state is 87%.

Finally, we measured the CHSH Bell inequality $S \leq 2$, with S given by (1.25). Estimation of the correlators (1.26) requires the evaluation of N_{ab}, the number of coincidences registered at Alice's output $a = +, -$ and Bob's output $b = +, -$, with $+, - = H, V$. The three available outputs give directly the values of N_{-+} and N_{--}. To estimate N_{++} and N_{+-}, we proceed similarly to [CH74], using the expression

$$E = \frac{(N_{+}^{B} - 2N_{-+}) - (N_{-}^{B} - 2N_{--})}{N_{+}^{B} + N_{-}^{B}}, \tag{4.4}$$

where $N_{a}^{B} = N_{+a} + N_{-a}$, with $a = +, -$, are estimated from two-photon interference measurements, see figure 4.2. After carefully selecting the analyzer parameters for which the value of S will be maximal, we measure (after subtraction of noise)

$$S_{\mathrm{expt}} = 2.37 \pm 0.19, \tag{4.5}$$

thereby violating the CHSH inequality by almost two standard deviations.

In summary, we have presented an SOI integrated source of polarization-entangled photons based on a 2D grating coupler. Our work confirms the relevance of SOI for integrated quantum optics. In future work the degree of entanglement of the source could be tuned on chip by modifying the ratio of the integrated coupler.

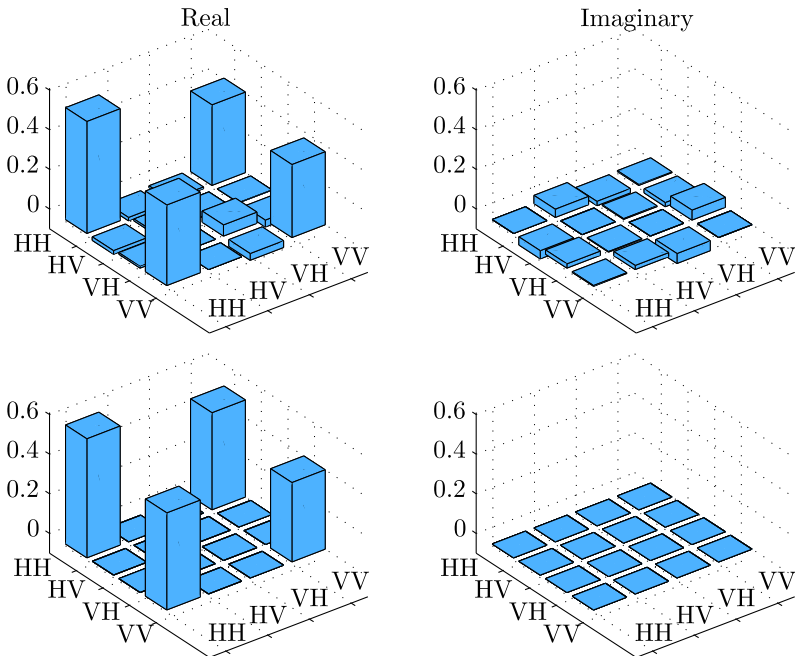

Figure 4.3: Tomography of polarization-entangled photons from an SOI chip. Estimated density matrix $\rho_{AB}^{(in)}$ of the state produced at the output of the silicon chip is shown in the upper panels. This state has 88% fidelity with the nonmaximally entangled state $\sqrt{0.6}|H\rangle_A|H\rangle_B + \sqrt{0.4}|V\rangle_A|V\rangle_B$, whose density matrix is represented in the lower panels. For each density matrix, $\mathrm{Re}(\rho)$ and $\mathrm{Im}(\rho)$ are plotted on the left and right, respectively. Figure from [OSC+13].

Finally, we mention that frequency-bin entanglement is an interesting approach for SOI integrated sources. Low brightness sources could benefit from the high collection of interleavers if dispersion compensation is implemented. SOI chips dedicated to frequency-bin entanglement could also be of interest: using ring resonators, one could directly produce a discrete frequency-comb entangled state which could be manipulated and detected efficiently with the experimental methods described in chapter 2.

Chapter 5

Experimental refutation of a class of ψ-epistemic models

Throughout this chapter, we follow very closely reference [POD+13]. We report an experimental test on physical reality.

There is still no definite answer to the question: what is the fundamental nature of the quantum state? This has been the subject of discussions since the origin of the theory. As was done in section 1.1, quantum textbooks define the quantum state ψ as a mathematical object —a ray in Hilbert space— used to determine the outcome probabilities of measurements on physical systems. But does the quantum state correspond to a real property of the physical system or does it merely represent our knowledge about the system? In other words: is it *ontic* (from Greek "ontos", real) or *epistemic* (from Greek "episteme", knowledge)?

There are indeed major reasons to doubt of the reality of the quantum state. For instance, the quantum state cannot be observed directly: it can only be reconstructed indirectly by carrying out measurements on ensembles of identically prepared systems [PR04, AV93]. In an epistemic interpretation, the quantum state would represent only an observer's knowledge of the physical system, rather than a physical reality. Such an interpretation could provide an intuitive explanation for many quantum phenomena, such as the measurement postulate and wave-function collapse, which would be nothing more than Bayesian updating [CFS02, BZ03, Spe07].

A consistent formulation of ψ-epistemic models would constitute a conceptual revolution of quantum mechanics. However, recent theoretical breakthroughs in the foundations of quantum theory, in the form of no-go theorems [PBR12, PPM13], show that ψ-epistemic models that obey natural conditions cannot reproduce the predictions of quantum theory.

Hereafter, we first describe the ontic and epistemic alternatives with precision. Then we outline the demonstration of the no-go theorem [PPM13] on which our experimental test is based. Finally, we present and analyze in detail our quantum optics experiment, which confirms the predictions of quantum theory and therefore rules out large classes of ψ-epistemic models [POD+13]. We discuss in detail the interpretation of the experiment.

5.1 ψ-ontic and ψ-epistemic models

Following the formulation of Nicholas HARRIGAN and Robert W. SPEKKENS [HS10], the starting point is the assumption that every quantum system possesses a real physical state, generally called the ontic state, denoted λ. Somewhat similarly than in the Bell theorem (see sec-

tion 1.2), we suppose that our present description of Nature could be incomplete, and that the real state λ of a physical system is not known to the present physics. There are two alternatives: either the quantum state ψ is a property of the real state, which only "complements" ψ (such a ψ-complemented theory is not very different from a ψ-complete theory); or it is not. Note that we do not consider here the possibility that there would be no (underlying) "reality".

The ontic state determines the probabilities of measurement outcomes. When an ensemble of systems is prepared, different members of the ensemble may be in different ontic states λ. A preparation procedure Q is therefore associated with a probability distribution $P(\lambda|Q)$ over the ontic states. When a measurement is carried out on a system in ontic state λ, the probability to obtain outcome r is $P(r|M,\lambda)$. Therefore if preparation Q is followed by measurement M the probability of outcome r is

$$P(r|M,Q) = \sum_{\lambda} P(r|M,\lambda)P(\lambda|Q)\,. \tag{5.1}$$

These models reproduce the predictions of quantum theory if $P(r|M,Q) = \langle\psi_Q|M_r|\psi_Q\rangle$, where M_r is the quantum operator corresponding to the outcome r and ψ_Q is the quantum state assigned by quantum theory to the preparation Q. Following [HS10], one can distinguish two classes of models.

In ψ-ontic models, there is a one-to-one correspondence between quantum states $|\psi\rangle$ and real states λ. Different quantum states $|\psi_0\rangle \neq |\psi_1\rangle$ correspond to different real states $\lambda_0 \neq \lambda_1$. That is, the preparation of distinct pure quantum states always gives rise to distinct real states. An ontological model is ψ-ontic if for any pair of preparation procedures Q and Q' associated with distinct quantum states $|\psi_Q\rangle$ and $|\psi_{Q'}\rangle$, we have $P(\lambda|Q)P(\lambda|Q') = 0$ for every λ. Every real state λ is thus compatible with a unique pure quantum state. The quantum state is "encoded" in λ and can be considered as representing a real property of the system.

In ψ-epistemic models, the quantum state is *not* a real property of the system and reflects only the incomplete knowledge of an observer, similarly to statistical distributions in classical physics. Distinct quantum states may correspond to the same underlying reality. That is, there exist preparations Q and Q' corresponding to nonidentical quantum states $|\psi_Q\rangle \neq |\psi_{Q'}\rangle$ such that $P(\lambda|Q)P(\lambda|Q') > 0$ for some λ. In this case, the quantum state is not uniquely determined by the underlying real state.

In [PBR12], Matthew F. PUSEY, Jonathan BARRETT, and Terry RUDOLPH (PBR) claimed that "the quantum state cannot be interpreted statistically", in the sense described above. They showed that ψ-epistemic models cannot reproduce the predictions of quantum theory if they satisfy the property, termed *preparation independence*, that independently prepared pure quantum states correspond to product distributions over ontic states. This no-go theorem has generated an important activity in the scientific community. Additional theoretical results presenting no-go theorems for classes of ψ-epistemic models have been reported (see publications citing PBR). It is important to note that all these theorems imply assumptions. As shown in [LJBR12], "the quantum state can be interpreted statistically" with a ψ-epistemic model satisfying all those constraints. But with "non-reasonable" properties, the epistemic view of the quantum state appears as a less elegant way to describe reality.

All these theorems suggest the possibility of novel experiments in the foundations of quantum mechanics. Here we report an experimental test based on the result obtained by Manas Kumar PATRA, Stefano PIRONIO and Serge MASSAR (PPM) in [PPM13]. They have shown that epistemic models cannot reproduce all the predictions of quantum theory if they satisfy a natural property of continuity. The advantage of this no-go theorem is that it allows an experimental test already at the level of a single system, contrary to the PBR argument. We have carried out such an experimental test, reported in [POD$^+$13], by using modulated weak coherent states of

light. We note that an experimental test of ψ-epistemic models based on the PBR theorem using two ions in the same trap was reported in [NMS+12]. Another experimental test of ψ-epistemic models has been recently exhibited in [RDB+14].

5.2 The Patra–Pironio–Massar theorem

As our experiment is based on [PPM13], we recall the relevant results. We start with the definition of what we call δ-continuous ψ-epistemic models. Let $\delta > 0$ and let B^δ_ψ be the ball of radius δ centered on $|\psi\rangle$, i.e., B^δ_ψ is the set of states $|\phi\rangle$ such that

$$\left|\langle\phi|\psi\rangle\right| \geq 1 - \delta\,. \tag{5.2}$$

We say that a model is δ continuous if for any preparation Q, there exists an ontic state λ (which can depend on Q) such that for all preparations Q' corresponding to quantum states $|\phi_{Q'}\rangle$ in the ball $B^\delta_{\psi_Q}$ centered on the state $|\psi_Q\rangle$, we have $P(\lambda|Q') > 0$. We refer to figure 5.1 for a depiction of the difference between ψ-ontic and δ-continuous ψ-epistemic models, and the relevant geometry of the Hilbert space.

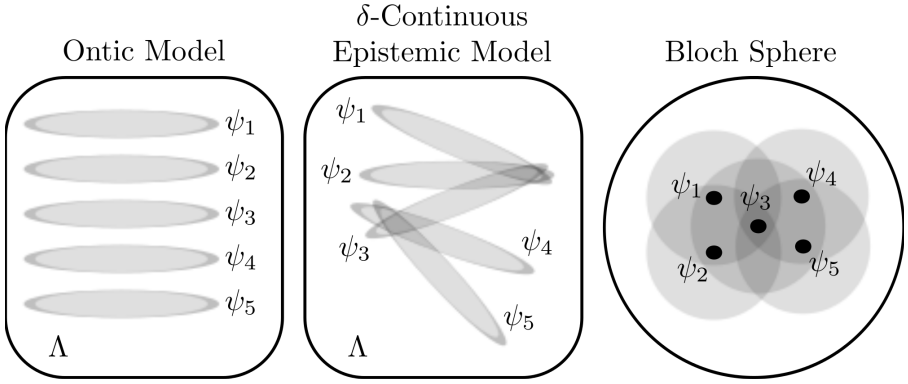

Figure 5.1: Illustration of ψ-ontic and δ-continuous ψ-epistemic models. Depicted (left and center) is the space Λ of ontic states, as well as the support of the probability distribution $P(\lambda|Q_k)$ for preparation Q_k associated to distinct pure states ψ_k, $k = 1, \ldots, 5$. In ψ-ontic models (left) distinct quantum states give rise to probability distribution $P(\lambda|Q_k)$ with no overlap. In δ-continuous ψ-epistemic models (center), states that are close to each other (such as $\{\psi_1, \psi_2, \psi_3\}$ and $\{\psi_3, \psi_4, \psi_5\}$) all share common ontic states. However states that are further from each other (such as ψ_1 and $\{\psi_4, \psi_5\}$) do not necessarily have common ontic states λ. On the right we represent the relationship between the states in Hilbert space. We have depicted by dots the positions of the states on the Bloch sphere, and in grey around each state the sphere of radius δ. For instance the sphere of radius δ around state ψ_1 includes states ψ_2 and ψ_3, but not states ψ_4 and ψ_5. In δ-continuous epistemic models all states in the ball of radius δ share at least one ontic state. Figure from [POD+13].

Why is this assumption "natural"? In order to motivate this definition, recall that according to the definition of ψ-ontic and ψ-epistemic models, we assign an ontic status to ψ if a variation of ψ necessarily implies a variation of the underlying reality λ, and we assign it an epistemic status if a variation of ψ does not necessarily imply a variation of the reality λ. It is then natural to assume a form of continuity for ψ-epistemic models: a slight change of ψ induces a slight change in the corresponding ensemble of λ's, in such a way that at least some λ's from the

initial ensemble will also belong to the perturbed ensemble. The above is a slightly stronger form of continuity which asserts that there are real states λ in the initial ensemble that will remain part of the perturbed ensemble, no matter how we perturb the initial state, provided the perturbation is small enough.

The PPM theorem states that if an epistemic model were to reproduce the predictions of quantum theory, then there is a fundamental constraint on its δ continuity. This constraint holds even at the level of a single quantum system. The no-go theorem is as follows [PPM13]: *δ-continuous ψ-epistemic models with $\delta \geq 1 - \sqrt{(d-1)/d}$ cannot reproduce all the measurement statistics of quantum states in a Hilbert space of dimension d.* We give an overview of the proof, as the construction used is the basis for the experimental test reported below.

We consider d preparations Q_k, $k = 1, \ldots, d$, corresponding to distinct quantum states $|\psi_k\rangle$ all contained in a ball of radius δ. By definition of a δ-continuous model, there is at least one λ for which $\min_k P(\lambda|Q_k) > 0$, and thus

$$\epsilon \equiv \sum_\lambda \min_k P(\lambda|Q_k) > 0\,. \tag{5.3}$$

This quantity can be viewed as a measure of the extent to which distributions over real states overlap in the neighborhood of a given quantum state. We now consider a measurement M that yields one of d possible outcomes $r = 1, \ldots, d$. If preparation Q_k is followed by measurement M, we denote by $P\big(r|M, Q_k\big)$ the probability of outcome r. By definition of a δ-continuous model, it makes the prediction

$$\sum_k P\big(k|M, Q_k\big) = \sum_k \sum_\lambda P\big(k|M, \lambda\big) P\big(\lambda|Q_k\big) \geq \sum_\lambda \min_k P\big(\lambda|Q_k\big) \equiv \epsilon > 0\,. \tag{5.4}$$

However, this is in contradiction with quantum theory. Indeed, let $\big\{|j\rangle : j = 1, \ldots, d\big\}$ be a basis of the Hilbert space. The d distinct states $|\psi_k\rangle = \frac{1}{\sqrt{d-1}} \sum_{j \neq k} |j\rangle$ are all at mutual distance $\delta = 1 - \big|\langle\psi_k|\psi\rangle\big| = 1 - \sqrt{(d-1)/d}$ from the state $|\psi\rangle = \frac{1}{\sqrt{d}} \sum_j |j\rangle$. If M is the measurement in the basis $\big\{|j\rangle\big\}$, then $P\big(k|M, Q_k\big) = 0$ for all $k = 1, \ldots, d$, and thus $\sum_k P(k|M, Q_k) = 0$, in contradiction with (5.4).

The above theorem leads us to define a class of ψ-epistemic models whose existence can be tested experimentally. They are labeled by the two parameters δ and ϵ that come up in the key equations (5.2) and (5.3). That is, a $\delta\epsilon$-ψ-epistemic model is such that for any set of preparations Q_k corresponding to distinct quantum states $|\psi_k\rangle$ all contained in a ball of radius δ,

$$\sum_\lambda \min_k P(\lambda|Q_k) \geq \epsilon\,. \tag{5.5}$$

5.3 Experimental setup

Our experiment is depicted in figure 5.2. We realize good approximations of the states $|\psi_k\rangle$ using coherent states of light traveling in an optical fiber. The basis states $|j\rangle$ correspond to a photon localized at equally spaced positions in the optical fiber. These time bins are labeled by the time $t_j = j\tau$ at which they are detected, where τ is the spacing (in time) between the time bins, taken to be much larger than the time resolution of the single-photon detectors (see section 1.3). We use up to 80 time bins, leading to a very sensitive experiment, since the bound on the continuity parameter δ decreases when the dimensionality d increases (although this conclusion must be somewhat tempered, see section 5.5). We then measure the time of arrival of the photon, which tells us in which bin k the photon is present, and thus provides us with an experimental value for the quantity $\sum_k P(k|M, Q_k)$ which appears on the left-hand side of (5.4).

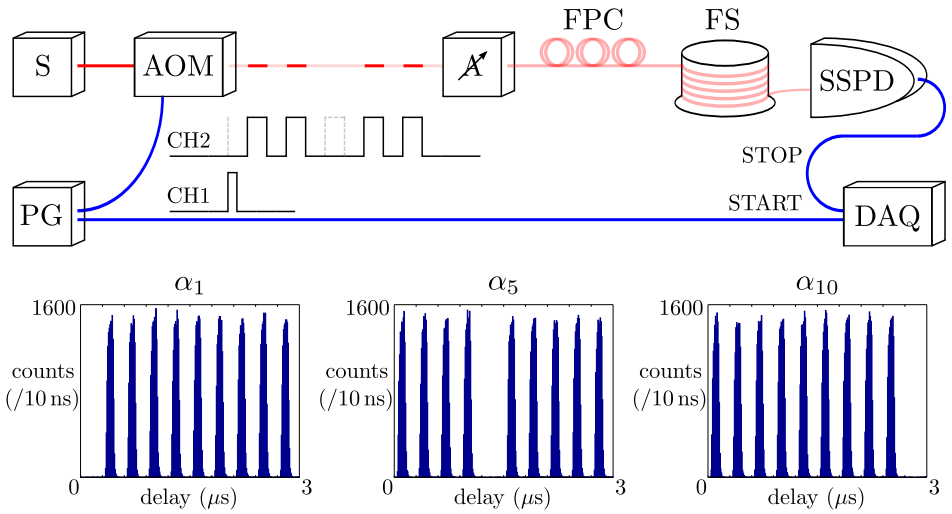

Figure 5.2: Experimental setup for testing δ-continuous ψ-epistemic models. Red links are optical fibers and blue links are radio-frequency cables. A continuous laser source (S) in the telecommunication C band emits a coherent state whose intensity is modulated by an acousto-optic modulator (AOM) driven by a pattern generator (PG), yielding a train of d pulses with one missing. The train of pulses is then attenuated to the single-photon regime by passing through an optical attenuator (A). The complete pulse train is stored in a 5 km fiber spool (FS), and then sent to a superconducting single-photon detector (SSPD). A fibre polarization controller (FPC) is used to ensure maximum sensitivity of the SSPD (which is polarization sensitive). When a photon is detected, an electric signal is sent to a data acquisition system (DAQ) which stores the time at which the detection event has taken place relative to the time at which the state preparation began. Bottom panel: Example of experimental results for $d = 10$, and states $|\alpha_1\rangle$, $|\alpha_5\rangle$, $|\alpha_{10}\rangle$. Horizontal axis: time at which a detection is registered. Vertical axis: number of detections in each 10 ns time window. Continuous ψ-epistemic models would predict a non-zero count rate in the bins which should be empty. The small number of counts which do occur due to detector dark counts and finite extinction ratio of the AOM are not visible on this scale. Figure from [POD+13].

The laser source (KOHERAS ADJUSTIK) continuously emits 1 mW of power at 1549.4 nm into an optical fiber. Its narrow spectral linewidth ($\Delta\nu \sim 1$ kHz when measured during 120 μs, as specified by the manufacturer) corresponds to a coherence time $\tau_{\text{coh}} = (2\pi\Delta\nu)^{-1} \sim 160\,\mu$s, significantly longer than all other time scales in the experiment. An upper bound on the laser linewidth was obtained in [LCK+10] which used the same laser: success of that experiment required that the linewidth of the laser be at most $\Delta\nu \leq 20$ kHz. Very small power fluctuations and very high rejection of side lobes guarantee that within the time interval used to produce the train of pulses the source emits a coherent state (1.29) of well-defined photon mean number.

We then create a pulse train from the continuous-wave laser output using an acousto-optic modulator (AOM). Trains of $d = 3, 10, 30, 50, 80$ pulses with one missing are created. The AOM (GOOCH AND HOUSEGO) has 25 ns rise and fall times. In the pulsed regime used in the experiment the extinction ratio is estimated to be $R_{\text{ext}} = 40 \pm 1.5$ dB.

A pattern generator (HEWLETT-PACKARD) drives the AOM. The AOM is turned on for 100 ns and then off for 200 ns. Optical attenuators with an absolute precision of 0.1 dB and a repeatability of 0.01 dB allow to reach a mean number of photons in the pulse train of $\langle n \rangle = \alpha^2 = 0.2$ for all dimensions d investigated.

To complete the state preparation phase, the light is sent through a fiber spool long enough to store the complete pulse train. The photons are detected with a superconducting single-photon detector (SSPD, from SCONTEL, see section 2.5) cooled to 1.7 ± 0.1 K with overall efficiency (including losses in optical components after the state preparation and data acquisition inefficiency) $\eta = (4 \pm 0.2)\%$ and dark-count rate $C_{dk} = 3 \pm 1$ Hz. The dark-count rate can be measured with high precision, but it is sensitive to environmental conditions (temperature of the detectors, ambient light) that fluctuate during the experiment, which is the reason the quoted error is large.

The data acquisition is performed by a time-to-digital converter (Agilent Acqiris, see section 2.5). The overall time resolution of the detector and data acquisition is approximately 150 ps. In order to minimize the effects of the finite rise and fall times of the AOM, we keep only the clicks that occur during an interval of width $T_p = 80$ ns centered on the middle of each time bin. For the different values of dimension $d = 3, 10, 30, 50, 80$ studied, the total number of times each state was produced was $(12, 10, 4, 3, 2) \times 128 \times 10^4$, respectively. The data were acquired over the duration of one week. An example of recorded data is depicted in figure 5.2.

5.4 Interpretation of the experiment

Our experiment suffers from nonideal state preparation (of coherent states with imperfectly known phase because of uncontrolled phase drifts of the laser) and nonideal measurements (arising from losses and inefficient detection). We now discuss the consequences of these "loopholes" for the interpretation of the experiment. The observed data could be explained by continuous epistemic models that exploit these loopholes. Hence, this experiment tests only epistemic models that satisfy "reasonable" additional constraints. In the case of the detection loophole, we have to make an assumption similar to the fair-sampling assumption often made in nonlocality experiments, see section 1.2. In the case of uncertainty in the preparation procedure, we must make the hypothesis that the ontic state does not depend on whether or not control measurements are included in the preparation procedure.

5.4.1 Detection loophole

The laser is cut into d pulses with one missing, and then attenuated, yielding the coherent state

$$|\alpha_k\rangle \simeq |0\rangle + \alpha \left(\frac{1}{\sqrt{d-1}} \sum_{j \neq k} |j\rangle \right) + O(\alpha^2) , \tag{5.6}$$

where $|0\rangle$ denotes the vacuum state and where, for simplicity of notation, we omit the contributions from two and more photons. The mean number of photons is $\langle n \rangle = \alpha^2 = 0.2$ for all dimensions d investigated.

Because the states prepared in our experiment have a significant vacuum component and because of losses and finite detector efficiency, the preparation of a quantum state $|\alpha_k\rangle$ can give rise either to a detection in one of the time bins, or to a *no-click* event if no photon is registered. Use of coherent states with $\langle n \rangle = 0.2$ and overall detection efficiency of approximately 4% yields an overall probability of registering a click of approximately $P(\text{clk}) = 8 \cdot 10^{-3}$, where "clk" is the event that the detector clicks in one of the time bins.

These no-click events affect the interpretation of the experiment. To understand why, remember that the key point of the PPM theorem was showing that if there is an ontic state that occurs with positive probability for all states $|\psi_k\rangle$, then one finds a contradiction with quantum theory.

But in the presence of no-click events this contradiction no longer holds. Indeed there exists a trivial ψ-epistemic model that explains our experimental results in which the ontic states common to all preparations $|\alpha_k\rangle$ only give rise to no-click events. Furthermore, the vacuum component of the states $|\alpha_k\rangle$ affects the interpretation of their mutual scalar product (since states that are almost orthogonal become arbitrarily close to each other when superposed with a sufficiently large vacuum component that does not contribute to the click events).

The basis for generalizing the analysis is to distinguish between two classes of ontic states: the set of ontic states denoted Λ_0 which only give rise to no-click events; and the complementary set $\Lambda_{\text{clk}} = \Lambda \setminus \Lambda_0$, see figure 5.3. All ontic states belonging to the set Λ_{clk} give rise to a click with positive probability. If for each preparation $|\alpha_k\rangle$, ontic states belonging to Λ_{clk} occur with positive probability, then we can apply an analog of the PPM theorem.

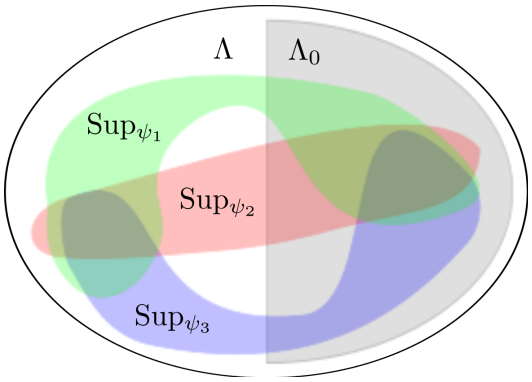

Figure 5.3: Detection loophole in the test of ψ-epistemic models. Schematic depiction of the structure of the space Λ of ontic states in the case of inefficient detectors. We have represented the supports Sup_{ψ_k} of the probability distributions $p(\lambda|\psi_k)$ for three states $|\psi_1\rangle, |\psi_2\rangle, |\psi_3\rangle$. The subset of ontic states which never give rise to a click is denoted by Λ_0. The experiment described in the main text cannot rule out the existence of a non-empty intersection of the supports Sup_{ψ_k} and of Λ_0, since all ontic states in this intersection always give rise to no-click events. The reported experiment can rule out the existence of a non-empty intersection of the supports Sup_{ψ_k} and the complementary space $\Lambda_{\text{clk}} = \Lambda \setminus \Lambda_0$. Figure from [POD+13].

To proceed quantitatively, we first redefine the notion of distance between states to take into account that the vacuum component never gives rise to a click. The new notion of distance δ_0 should have the following properties: (1) it measures the distance between states on the space orthogonal to the vacuum state; and (2) it equals the old distance $\delta_0 = \delta$ on the single-photon space. The exact way δ_0 acts on the two and more photon space is not essential for the argument (since the overlap of the states we consider with the two and more photon space is small). The reason for property (1) is that the vacuum component of the state will not give rise to a click, and hence does not give rise to any measurable quantity. The reason for property (2) is that in the case of single-photon states and perfect detectors we wish to recover the notion of δ-continuity defined above.

This leads to the following definition: A model with no-click events is δ_0-continuous if, for all preparations Q corresponding to pure state $|\psi_Q\rangle$ with $P(\text{clk}|\psi_Q) > 0$, there exists an ontic state λ (which can depend on $|\psi_Q\rangle$) such that, for all preparations Q' corresponding to state $|\phi_{Q'}\rangle$ with

$$|\langle\tilde{\phi}_{Q'}|\tilde{\psi}_Q\rangle| \geq 1 - \delta_0\,, \tag{5.7}$$

we have $P\left(\lambda|\phi_{Q'}, \text{clk}\right) > 0$, where $|\tilde{\psi}_Q\rangle = \frac{(I-|0\rangle\langle 0|)|\psi_Q\rangle}{|(I-|0\rangle\langle 0|)|\psi_Q\rangle|}$ is the projection of $|\psi_Q\rangle$ onto the space

orthogonal to the vacuum, and $|\tilde{\phi}_{Q'}\rangle$ is similarly defined.

As illustration of this new notion of distance, consider the coherent states

$$|\alpha_k\rangle = \exp\left[-\alpha^2/2\right] \exp\left[\frac{\alpha}{\sqrt{d-1}} \sum_{j\neq k} a_j^\dagger\right] |0\rangle\,, \tag{5.8}$$

and the reference state

$$|\alpha_0\rangle = \exp\left[-\alpha^2/2\right] \exp\left[\frac{\alpha}{\sqrt{d}} \sum_{j} a_j^\dagger\right] |0\rangle\,. \tag{5.9}$$

As $|\langle\tilde{\alpha}_k|\tilde{\alpha}_0\rangle| = \frac{e^{\alpha^2\sqrt{(d-1)/d}}-1}{e^{\alpha^2}-1}$, the distance δ_0 is given by

$$\delta_0(d,\alpha^2) = 1 - \frac{e^{\alpha^2\sqrt{(d-1)/d}}-1}{e^{\alpha^2}-1} = 1 - \sqrt{\frac{d-1}{d}} + O\left(\alpha^2\right)\,. \tag{5.10}$$

For the experimentally relevant case $\alpha^2 = \langle n\rangle = 0.2$, we find $\delta_0(d,\alpha^2=0.2) \simeq 0.55/d$.

We must also introduce the notion of inefficient detectors. *An inefficient detector provides a response that depends only on the photon number. If there is no photon, it does not click. If there are one or more photons, the probability of clicking is strictly positive.* We now consider the analog of the PPM theorem in the case of inefficient detectors. *δ_0-continuous ψ-epistemic models with $\delta_0 > 1 - \sqrt{(d-1)/d}$ cannot reproduce all the measurement statistics on coherent states of d modes, even in the presence of inefficient detectors.* The proof is given in [POD+13] for coherent states. We consider the experimentally accessible quantity

$$\epsilon_{\text{expt}} = \sum_k P(k|Q_k,\text{clk}) = \sum_k \frac{N(k,Q_k)}{\sum_j N(j,Q_k)}\,, \tag{5.11}$$

where $N(j,Q_k)$ is the number of clicks registered in outcome j when one prepares the coherent state $|\alpha_k\rangle$ with preparation Q_k ($k = 1,\ldots,d$), and clk is the event that the detector clicks. All the states $|\alpha_k\rangle$ are at distance $1 - |\langle\tilde{\alpha}_k|\tilde{\alpha}_0\rangle| > \delta_0$ from some reference coherent state $|\alpha_0\rangle$. A δ_0-continuous ψ-epistemic model makes the prediction that $\epsilon_{\text{expt}} > 0$, while quantum mechanics predicts $\epsilon_{\text{expt}} = 0$.

The above definitions and theorem lead us to define $\delta_0\epsilon$-ψ-epistemic models, whose existence can be tested experimentally, even in the presence of losses and inefficient detectors. Consider an arbitrary number of preparations Q_k corresponding to distinct quantum states $|\psi_k\rangle$ all contained in a ball of radius δ_0, where δ_0 is given by (5.7). A $\delta_0\epsilon$-ψ-epistemic model is such that, for all choices of Q_k,

$$\sum_\lambda \min_k P(\lambda|Q_k) \geq \epsilon\,. \tag{5.12}$$

It is this class of models that are experimentally tested in our experiment.

5.4.2 Preparation of mixed states

The expression (5.6) supposes an ideal output from the laser source. However, lasers fluctuate. For a laser operating well above threshold, the major source of fluctuation is phase drift, responsible for the finite linewidth of the laser. Even though the coherence time of the laser $\tau_{\text{coh}} \sim 160\,\mu$s is much longer than the longest pulse train (of length $80 \times 300\,\text{ns} = 24\,\mu$s), this

phase drift cannot be neglected. A more precise description of the preparation procedure is therefore that it yields the state

$$|\alpha_{k,\varphi}\rangle = \exp\left[-\alpha^2/2\right] \prod_{j\neq k} \exp\left[\frac{\alpha e^{i\varphi_j} a_j^\dagger}{\sqrt{d-1}}\right] |0\rangle \tag{5.13}$$

$$\simeq |0\rangle + \alpha\left(\frac{1}{\sqrt{d-1}} \sum_{j\neq k} e^{i\varphi_j}|j\rangle\right) + O(\alpha^2)\,. \tag{5.14}$$

Since the phase fluctuations of a laser are generally modeled as a random walk of the phase [GC08], $y_j = \varphi_j - \varphi_{j-1}$ should be modeled as independent identically distributed random variables with normal distribution

$$P(y_j) = \frac{1}{\sqrt{4\pi D t_0}} e^{-\frac{y_j^2}{4Dt_0}}\,, \tag{5.15}$$

where $D = 1/\tau_{\text{coh}}$ is the diffusion constant [Scu97] and t_0 is the time between centers of two time bins.

We take this model as basis for the analysis. Extensions, taking into account for instance phase drift within each time bin, or intensity fluctuations of the laser, are briefly discussed below. In order to understand the implications of fluctuations on the prepared state, we first discuss the interpretation of the experiment if the phases φ_j were known. We then consider the experimentally relevant case where the phases φ_j are unknown.

If the phases φ_j were known, then for each state $|\alpha_{k,\varphi}\rangle$ we could compute the δ_0-distance to the reference state $|\alpha_0\rangle$. We would then keep only the data corresponding to the case where $\delta_0(\alpha_{k,\varphi}, \alpha_0)$ is less than some threshold Δ_0. For the states $|\alpha_{k,\varphi}\rangle$, we have (for an ideal experiment) that $P(k|\alpha_{k,\varphi}) = 0$. For the subset of states with $\delta_0(\alpha_{k,\varphi}, \alpha_0) < \Delta_0$, we can estimate the value of ϵ_{expt} (which will be non-zero because of experimental imperfections) from the measurement data. The data then exclude δ_0-continuous epistemic models with $\delta_0 > \Delta_0$ and $\epsilon > \epsilon_{\text{expt}}$.

If we do not know the phases φ_j, then we must make additional assumptions. Note that if one averages over the unknown phases φ_j, the state prepared by the device is a mixed state. This is problematic as the notions of ψ-epistemic and ψ-ontic models are defined for pure states. Therefore the no-go theorems do not apply directly. We reason around this difficulty as follows. There is in principle a simple modification of the experimental procedure that could be used to determine the phase of the laser: namely part of the laser light could be diverted and then measured. This additional measurement has not been carried out. But it is natural to assume that the probability distribution of ontic states $P(\lambda|Q_k)$ does not depend on whether or not these additional measurements are carried out. (We note that in our preparation procedure, a large part of the light is in fact diverted, and then absorbed, by the attenuators).

Making this assumption, we can consider that the state preparation yields pure states of the form (5.13) with small, random, phases affecting each time bin. We do not know what are the values of the phases, but we can determine the probability distribution of $\delta_0(\alpha_{k,\varphi}, \alpha_0)$. From this probability distribution we can estimate the probability q that δ_0 is less than a specific value Δ_0: $P[\delta_0(\alpha_{k,\varphi}, \alpha_0) \leq \Delta_0] = q(\Delta_0)$. Equivalently we know what proportion q of prepared states had $\delta_0(\alpha_{k,\varphi}, \alpha_0) \leq \Delta_0(q)$. We also know the experimentally determined value of ϵ_{expt}. However this value is an average over all prepared states. For a conservative estimate we make the worst case assumption that all the contribution to ϵ_{expt} comes from the states with $\delta_0(\alpha_{k,\varphi}, \alpha_0) \leq \Delta_0$. This implies that we must make the substitution $\epsilon_{\text{expt}} \to \epsilon_{\text{expt}}(q) = \epsilon_{\text{expt}}/q$. This is the price to pay for not having experimentally measured the phases φ_j. The data then exclude δ_0-continuous

epistemic models with $\delta_0 > \Delta_0$ and $\epsilon > \epsilon_{\text{expt}}(q)$. Note that we can vary the parameters q and Δ_0 to exclude a region as large as possible in the δ_0, ϵ plane.

In practice we proceed as follows. We fix the dimension $d = 3, 10, 30, 50, 80$. We fix $k \in \{1, \ldots, d\}$. We choose at random variables y_j, $j = 1, \ldots, d$, drawn from the distribution (5.15). To these variables we associate the state $|\alpha_{k,\varphi}\rangle$ defined in (5.13). We then compute the distance $\delta_0(\alpha_{k,\varphi}, \alpha_0) = 1 - |\langle\tilde{\alpha}_{k,\varphi}|\tilde{\alpha}_0\rangle|$, where $|\alpha_0\rangle$ is given by (5.9). We repeat the procedure $10^6/d$ times for each value of k. For simplicity we then average the resulting histograms over k, yielding a probability distribution for δ_0: $P(\delta_0) = \frac{1}{d}\sum_{k=1}^{d} P[\delta_0(\alpha_{k,\varphi}, \alpha_0)]$. From this numerically (Monte-Carlo simulation) determined distribution we can compute with high precision the function $\Delta_0(q)$ given by $P((\delta_0 \leq \Delta_0) = q$.

Finally we note that the states prepared by the laser may differ from the ideal state (5.6) in more ways than are modeled in (5.13). Such effects could include intensity fluctuations of the laser, or phase drift within each time bin. We could take them into account by using a better model of the laser output. However since the linewidth of a laser well above threshold is generally modeled as being entirely due to phase drift, and since the coherence time is much longer than the duration of one time bin, we expect that the above takes into account most of the effects due to uncertainty in the state preparation. We note that our procedure of ascribing all the contribution to ϵ_{expt} from the states with $\delta_0(\alpha_{k,\varphi}, \alpha_0) \leq \Delta_0$ is very conservative, and implies that the true value of ϵ_{expt} is probably significantly smaller than the one we use.

5.5 Experimental results

Our experimental results provide constraints on ψ-epistemic models that satisfy the additional constraints described above. More precisely, we parametrize ψ-epistemic models by two parameters, δ_0 that describes how continuous the model is, and ϵ that describes how epistemic it is. Our experimental results rule out a large class of models labeled by these two parameters.

Our raw experimental results are reported in table 5.1 and figure 5.4. Specifically we give the number d of time bins, the measured fraction of clicks in the bin that should contain no photon, i.e. $\epsilon_{\text{expt}}(d) = \sum_k \frac{N(k,Q_k)}{\sum_j N(j,Q_k)}$, and its statistical error.

Table 5.1: Experimental bounds on ψ-epistemic models. Parameters d are the investigated dimensions of the quantum state space, with the corresponding values of $\delta = 1 - \sqrt{(d-1)/d}$. Measured values ϵ_{expt} are given with their statistical uncertainty $\Delta\epsilon_{\text{expt}}$. Values $\epsilon_{\text{predict}}$ correspond to quantum theory predictions when taking into account experimental imperfections, with $\Delta\epsilon_{\text{predict}}$ arising from uncertainty on instrument parameters. Data from [POD+13].

d	3	10	30	50	80
δ	0.184	0.051	0.017	0.010	0.006
$\epsilon_{\text{expt}} \times 10^3$	0.26	0.45	1.27	1.62	1.66
$\Delta\epsilon_{\text{expt}} \times 10^3$	$\pm$0.05	$\pm$0.07	$\pm$0.18	$\pm$0.23	$\pm$0.28
$\epsilon_{\text{predict}} \times 10^3$	0.24	0.41	0.99	1.58	2.46
$\Delta\epsilon_{\text{predict}} \times 10^3$	$\pm$0.09	$\pm$0.15	$\pm$0.37	$\pm$0.58	$\pm$0.88

The fact that $\epsilon_{\text{expt}}(d)$ is not strictly zero, at first glance in conflict with quantum theory prediction $\epsilon = 0$, is expected, since the optical components are imperfect. We have estimated the expected values of $\epsilon_{\text{expt}}(d)$ from the following measured experimental parameters: extinction

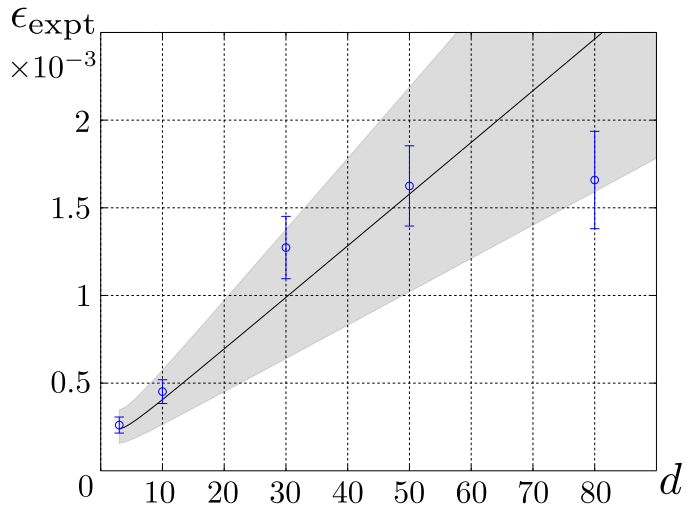

Figure 5.4: Experimental bounds on ψ-epistemic models as a function of dimension d of the quantum state space. The vertical axis gives the measured value of $\epsilon_{\text{expt}} = \sum_k \frac{N(k,Q_{\alpha_k})}{\sum_j N(j,Q_{\alpha_k})}$, where $N(j, Q_{\alpha_k})$ is the number of clicks registered in bin j when one prepares state α_k (error bars are statistical). These values are also given in table 5.1. The curve gives the dependency of ϵ_{expt} on d as predicted by quantum theory, taking into account the values of measured experimental parameters. The grey area gives the range in which this theoretical prediction could vary, given the uncertainty on dark-count rate, extinction ratio, and overall detection probability $\eta\langle n\rangle$. The main uncertainty comes from the dark-count rate which depends on the exact temperature of the detectors and the amount of ambient light, both of which can vary during the experiment. Positive deviation from the curve would signal a breakdown of quantum theory. The absence of such deviation rules out a large class of δ-continuous models. Figure from [POD+13].

ratio of the AOM, mean number of photons in each pulse, optical attenuation and detector efficiency, and detector dark counts. The probability of detecting a photon in bin k when state α_k is prepared is approximately $Dk\,T_p + Ext\,\langle n\rangle\eta/(d-1)$, and the probability of detecting a photon when state α_k is prepared is approximately $\langle n\rangle\eta$, where d is the dimension of the state, $Dk\,T_p$ is the probability of a dark count during a pulse, Ext is the extinction ratio of the AOM, $\langle n\rangle$ is the mean number of photons in the pulse train, and η is the overall detection efficiency. Note that these approximations of an exact expression are valid for our experimental parameters. The ratio of these two quantities multiplied by d yields the following estimate for the experimentally measured quantity ϵ_{expt}:

$$\text{Expected value of } \epsilon_{\text{expt}} = \frac{Dk\,T_p}{\langle n\rangle\eta} d + Ext\frac{d}{d-1}\,. \tag{5.16}$$

This expected value, including its uncertainty, is plotted in grey in figure 5.4. Deviations from this expected behavior could signal that quantum theory should be replaced by an epistemic model. The measured values of ϵ_{expt}, which are of the order 10^{-3}, do not exhibit large deviations from the expected behavior of $\epsilon_{\text{expt}}(d)$.

These experimental results can be used to rule out a class of $\delta_0\epsilon$-ψ-epistemic models. Specifically we proceed as follows. Using the procedure outlined at the end of section 5.4, we can determine for each dimension d the function $\Delta_0(q)$. Specifically we choose a series of values of

$0 < q < 1$, and compute the corresponding value of $\Delta_0(q)$. Then, for each d and for each of these values of q, the models with $\delta_0 \geq \Delta_0(q)$ and $\epsilon \geq \epsilon_{\text{expt}}(d)/q$ are ruled out. Thus for each dimension d, we rule out a region in the δ_0, ϵ plane. These results are given in figure 5.5.

In figure 5.5 (a) we plot all the couples $(\Delta_0(d,q), \epsilon_{\text{expt}}(d)/q)$ obtained by this procedure. For comparison we also plot the couples $(\delta_0, \epsilon_{\text{expt}})$ that would be obtained if we did not take into account the phase fluctuations of the laser. For small d, taking into account the phase fluctuations has a very small effect on the results because over the duration of 3 or 10 time bins, the phase fluctuations have only increased very little the value of δ_0. However when the number of time bins increases, the effect of the phase fluctuations becomes much more important, and this significantly affects the results. In figure 5.5 (b) we plot only those couples $(\Delta_0(d,q), \epsilon_{\text{expt}}(d)/q)$ which are most constraining, and give their statistical error.

5.6 Discussion

Whether the quantum wave-function is a real physical wave or a summary of our knowledge about a physical system is a question that has divided physicists since the inception of quantum theory. A precise formulation of these two alternatives, opening the way to clear-cut answers, was provided in [HS10]: if the wave-function corresponds to a real, ontic, property of physical systems, the preparation of a system in different pure quantum states should always result in different physical states. If, on the other hand, the wave-function has an epistemic status, such preparations should sometimes result in the same underlying physical state.

Following the breakthrough of PBR [PBR12], a flurry of no-go theorems for ψ-epistemic models obeying natural constraints have been proposed (see publications citing PBR). These no-go theorems inspire novel experimental tests. We reported a test of ψ-epistemic models based on the argument introduced in [PPM13]. There are two main motivations to perform such experiments. First, given that there are good reasons to support an epistemic view of the quantum state [Spe07], the no-go theorems provide new directions in which to look for potential deviations from the expected quantum predictions. Our experimental results do not exhibit any such deviations, therefore strengthening our belief in the validity of quantum theory. A second, related, motivation for performing an implementation of the no-go theorems is to rule out experimentally (certain classes of) ψ-epistemic models, in the same way that the violations of Bell inequalities rule out locally-causal models.

While such experiments have some common features with a Bell test, they also differ from it in several ways. To simplify the discussion, let us first consider the case of an ideal experiment free of experimental errors and noise. The proof of the PPM theorem tells us that if we prepare a system according to d possible procedures Q_k and subject it to a measurement M, then the observed value $\epsilon_{\text{expt}} = \sum_k P(k|M, Q_k)$ provides a constraint on the extent ϵ to which the distributions over real states associated to each preparation overlap. In particular, if $\epsilon_{\text{expt}} = 0$ then no common real state λ can be associated to all the preparations Q_k. This conclusion is obtained independently of what specific states (pure or mixed) are used, or what specific measurements are performed. It only depends on the observed measurement statistics, as does the violation of a Bell inequality.

However, contrary to Bell inequalities, the observation of a value $\epsilon_{\text{expt}} = 0$ does not *per se* imply that some "intrinsically quantum" or "non-classical" behavior has been produced in the experiment. Indeed, the quantity ϵ_{expt} has not been introduced to distinguish between a "classical" and a "quantum" worldview (as in Bell inequalities), but between ψ-ontic and ψ-epistemic models. Thus for instance the ψ-epistemic model presented in [LJBR12] perfectly reproduces all the predictions of quantum mechanics.

Furthermore, the statistics of an experimental test of ψ-ontic versus ψ-epistemic models could very easily be reproduced using purely classical states. For instance the use of d classical states of the form $\rho_k = \sum_{j\neq k} |j\rangle\langle j|/(d-1)$ instead of the states $|\psi_k\rangle$ in the PPM theorem would also yield a value of $\epsilon_{\text{expt}} = 0$. However, because these states are not pure, this experiment would not exclude ψ-epistemic models.

This shows that when carrying out an experimental test of ψ-ontic versus ψ-epistemic models, the kind of preparation procedures used in the experiment matters to its interpretation. Indeed, a ψ-epistemic model does not need to predict different results than quantum theory for all preparation procedures (for instance not for those associated to the purely-classical distributions ρ_k over orthogonal states mentioned above), but only for those corresponding to pure quantum states that are sufficiently close (within distance δ in the case of δ-continuous models). A meaningful test of δ-continuous ψ-epistemic models must therefore be based on two components: the measurement of ϵ_{expt} and a reasonable confidence that preparations corresponding to pure quantum states within distance δ have been used. This should be contrasted with Bell experiments that are "device independent": their interpretation is independent of the details of the state preparation and measurement procedures.

In this later respect, our experiment has some specific weaknesses related to the experimental system used (photonic time bins obtained by chopping and attenuating a continuous-wave laser). First, the use of coherent states that have a non-zero vacuum component and inefficient detectors resulting in no-click events require, to reach meaningful conclusions, the use of a fair-sampling assumption, a redefinition of the continuity parameter δ_0, and a redefinition of the quantity ϵ_{expt}. Second, we need an additional hypothesis on the epistemic model to ensure that the preparation used in the experiment yields (approximatively) pure coherent quantum states with a known overlap. This is due to the fact that we did not explicitly check the actual performance of the preparation procedure by, e.g., performing a direct measurement of δ_0. Such a verification would have required the use of a complex interferometer, and could have been performed only for very small dimension. Our approach was to use the very well understood physics of lasers operating well above threshold as a basis for modeling the quantum states produced by our preparation procedure. This allowed us to probe states in a much higher dimensional Hilbert space, and therefore small values of the continuity parameter δ_0, than would have been possible otherwise.

We note that the complementary approach can be followed by using frequency bins. Using a setup similar to the one presented in figure 3.4, one would be able to produce a quantum state of the form $|\psi_k\rangle$ in the frequency domain with an EOPM, though for relatively low dimensions compared to $d = 80$. However, the possibility to manipulate the state with a second EOPM would in principle allow a direct measurement of the parameter δ_0.

Taking into account all the above constraints, our experiment nevertheless excludes, with a high degree of confidence, a large class of ψ-epistemic models. These ψ-epistemic models are labeled by two parameters, δ_0 that describes how continuous the model is, and ϵ that describes how epistemic it is. Our experimental results exclude a region in the δ_0, ϵ plane, see figure 5.5.

The experimental test of ψ-epistemic models based on the original PBR no-go theorem reported in [NMS$^+$12] also excluded classes of ψ-epistemic models and also required additional hypotheses to ensure that the prepared states are pure quantum states with desired properties. Such additional hypotheses will probably be needed in any experimental test of ψ-epistemic models. The results nevertheless tend to show that ψ-epistemic models that reproduce the predictions of quantum theory must both be strongly discontinuous and assign a collective ontic state to independently prepared systems.

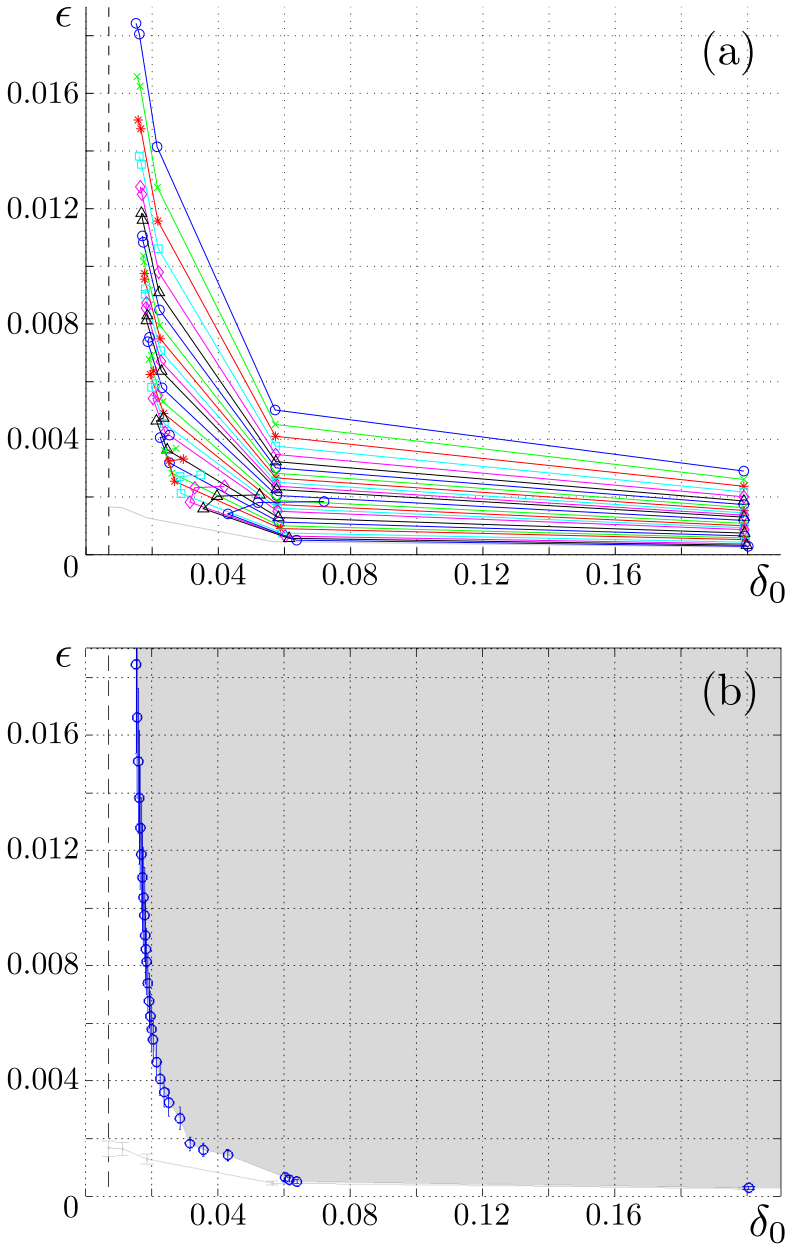

Figure 5.5: Experimentally excluded region in the δ_0, ϵ plane. (a) For each choice of the parameter q we compute the values $\Delta_0(d, q)$ and $\epsilon_{\text{expt}}(d)/q$ which are then plotted in the figure, and connected by a line. For curves from top to bottom, $q = 0.09, 0.10, 0.11, 0.12, 0.13, 0.14, 0.15, 0.16, 0.17, 0.18, 0.19, 0.20, 0.22, 0.24, 0.26, 0.28, 0.30, 0.35, 0.40, 0.45, 0.50, 0.60, 0.70, 0.80, 0.90$. The couples $(\delta_0, \epsilon_{\text{expt}}(d))$ that would be obtained if one did not take into account the phase fluctuations of the laser are plotted in light grey (lowest curve). For $d = 3, 10$, taking into account the phase fluctuations of the laser does not modify significantly the results, while for $d = 30, 50, 80$ the effect is important. In fact the excluded region for $d = 80$ is practically the same as for $d = 50$ when the phase fluctuations are taken into account. (b) Here we take only the points that are most constraining. We plot them with their error bars. The grey zone is the area in the δ_0, ϵ plane that is excluded by our experiment. Figure from [POD+13].

Conclusion and perspectives

In this thesis, we have demonstrated an original method for manipulating energy-time entangled photons at telecommunication wavelengths. We summarize our approach and results and discuss the perspectives opened by this work.

In order to implement quantum communication protocols, one needs to be able to efficiently produce, transmit, manipulate and detect photonic entangled quantum states. Optical fibers from the telecommunication industry offer a well-suited —low-loss and low-decoherence— transmission channel for photons, particularly when quantum information is encoded in their energy-time degree of freedom. In this context, the most common platform is time-bin encoding, which employs unbalanced Mach–Zehnder interferometers to encode information in the relative phase between distinct spatio-temporal paths. This phase has to be set precisely, imposing sub-wavelength stabilization of optical interferometers. To produce time-bin entanglement, one needs a nonlinear waveguide pumped by a long-coherence laser. To detect it, time-resolving single-photon detectors at telecommunication wavelengths are necessary. Both these production and detection tools are becoming commercially available, with continuously improving characteristics.

Using these off-the-shelf components does not limit one to a unique way to manipulate energy-time entangled photons. Instead of creating time bins, encoding information in their relative phase, and detecting the arrival time of the photons, one can create frequency bins, encode information in their relative phase, and detect the arrival frequency of the photons. Building on previous single-photon experiments, we have shown that electro-optic phase modulators driven by a radio-frequency system allow the implementation of such a frequency interferometer for entangled photons, while narrow-band frequency filters allow to discriminate the photons' frequencies, producing two-photon interference patterns in the frequency domain. Our setup comprises standard fiber-optic and electro-optic components, parametric down-conversion sources and single-photon detectors.

Manipulating energy-time entangled photons directly in the frequency domain with electro-optic phase modulators presents several advantages. From a technical point of view, this provides inherent precision, stability and robustness, removing the need for active stabilization of interferometers. This is highlighted by our experimental high-visibility ($> 99\%$) two-photon interference patterns, allowing the violation of Bell inequalities in an optimal way. From a conceptual point of view, while it is relatively difficult to build spatio-temporal interferometers with more than two paths, our method naturally gives rise to interference patterns corresponding to the coherent manipulation of states with dimension as high as eleven. High-dimensional states are interesting because they can provide with higher encoded information per photon.

Our approach presents however a few drawbacks. From a technical point of view, phase modulators and frequency filters imply high losses. This could be partially overcome with technical advances or by using dispersion-based techniques for resolving the photons' frequencies without frequency filters. From a conceptual point of view, the high dimensionality is not easily

exploited. Indeed, simultaneous detection of all results is resource-consuming; in practice we do not collect all the photons, leading for example to loopholes in Bell experiments. More fundamentally, the use of a sine modulating signal corresponds to Bessel-type interference patterns, whose dimensionality is limited by the power of the radio-frequency signal driving the phase modulators, and which fix all the phase relations between frequency bins once one of them is set. An important route would be to generalize accessible transformations, in order to better control the dimensionality, shape and phase relations of the frequency states.

The ability to manipulate in a specific way photonic quantum states dictates the design and implementation of quantum communication protocols. In this work, building on previous approaches, we presented the possibility to use frequency bins for quantum key distribution using the BB84 protocol. It can be expected that frequency bins created by sine or other shaped modulating signals would be suited for protocols allowing to exploit their high dimensionality. In supplement of quantum key distribution, many experiments require, can benefit from, or could be adapted to, high dimensionality, such as Hong–Ou–Mandel experiments, quantum coin-tossing, high-dimensional quantum walks, or tomography characterization techniques in frequency. It would be very interesting to demonstrate these experiments using frequency-bin entangled photons. In complement to one- and two-photon experiments, achievement of a four-photon experiment like entanglement swapping would be a huge progress towards a quantum network use of frequency-bin entanglement.

We have shown that periodic frequency filters artificially restrict the frequency states to effective quantum bits. This procedure, together with dispersion management, permits collection of a very high bandwidth and could be used to test low-brightness photon-pair sources. Sources such as ring resonators integrated on silicon-on-insulator chips could provide frequency combs specifically suited to our method. The versatility of frequency-bin entanglement thus provides general and specific applications —towards practical or fundamental research— which could be theoretically and experimentally explored in the near future.

In this thesis, we have also reported results from other quantum optics experiments at telecommunication wavelengths. One focuses on the generation of polarization-entangled photons in a silicon-on-insulator chip. This platform constitutes an important perspective for practical integrated quantum information and communication applications. We have also conducted an experimental investigation on the nature of the quantum state, using time bins. Our results agree with quantum mechanical predictions, consolidating the reality of the quantum state and potentially inspiring further research. We note that the frequency-bin approach could be of interest for these experiments.

Appendix A

Notations

Table A.1: List of notational shortcuts and scientific notations.

O	operator $\hat{O}$
ω	pulsation abusively termed frequency $\nu = \omega/2\pi$
$\|\psi\,\phi\rangle$	tensor product $\|\psi,\phi\rangle = \|\psi\rangle\|\phi\rangle = \|\psi\rangle \otimes \|\phi\rangle$
	(potentially with A and B indices in a bi-partite description)
$\chi^{(2)}$	second-order nonlinearity
$\chi^{(3)}$	third-order nonlinearity
H, V	horizontal and vertical (polarizations)
s, i	signal and idler (photons)
τ_{acc}	accidental coincidence rate
τ_{dk}	dark-count rate
τ_{net}	net coincidence rate
τ_{raw}	raw coincidence rate
V	visibility

Table A.2: List of acronyms.

A, B, E	Alice, Bob, Eve
APD	avalanche photodiode
BB84	Bennett–Brassard 1984
BBF	band-block filter
BS	beam splitter
CAR	coincidence-to-accidental ratio
CGLMP	Collins–Gisin–Linden–Massar–Popescu
CH74	Clauser–Horne 1974
CHSH	Clauser–Horne–Shimony–Holt
CMOS	complementary metal–oxyde–semiconductor
CW	continuous-wave
DAS	data acquisition system
DOF	degree of freedom
EDFA	erbium-doped fiber amplifier
EOPM	electro-optic phase modulator
EPR	Einstein–Podolsky–Rosen
FBG	fiber Bragg grating
FPC	fiber polarization controller
FWHM	full width at half maximum
HOM	Hong–Ou–Mandel
HWP	half-wave plate
LHV	local hidden variable
LSPP	localized surface plasmon polariton
MZI	Mach–Zehnder interferometer
PBR	Pusey–Barrett–Rudolph
PBS	polarizing beam splitter
PMF	polarization-maintaining optical fiber
PPLN	periodically-poled lithium niobate
PPM	Patra–Pironio–Massar
QBER	quantum bit error rate
QKD	quantum key distribution
QWP	quarter-wave plate
RF	radio-frequency
SMF	standard single-mode optical fiber
SNR	signal-to-noise ratio
SOI	silicon-on-insulator
SPD	single-photon detector
SPDC	spontaneous parametric down-conversion
SPP	surface plasmon polariton
SSPD	superconducting single-photon detector
TDC	time-to-digital converter
WDM	wavelength division multiplexer

Bibliography

[ABG+07] Antonio Acín, Nicolas Brunner, Nicolas Gisin, Serge Massar, Stefano Pironio, and Valerio Scarani. Device-independent security of quantum cryptography against collective attacks. *Physical Review Letters*, 98(23):230501, 2007. {cited on page 19}

[ADR82] Alain Aspect, Jean Dalibard, and Gérard Roger. Experimental test of Bell's inequalities using time-varying analyzers. *Physical Review Letters*, 49(25):1804, 1982. {cited on pages 2 and 10}

[Agr97] Govind P Agrawal. *Fiber-optic communication systems*. Wiley Online Library, 1997. {cited on page 2}

[Agr07] Govind P Agrawal. *Nonlinear fiber optics*. Academic Press, 2007. {cited on page 22}

[AKBH07] Irfan Ali-Khan, Curtis J Broadbent, and John C Howell. Large-alphabet quantum key distribution using energy-time entangled bipartite states. *Physical Review Letters*, 98(6):060503, 2007. {cited on page 60}

[AMY+07] A V Akimov, A Mukherjee, C L Yu, D E Chang, A S Zibrov, P R Hemmer, H Park, and M D Lukin. Generation of single optical plasmons in metallic nanowires coupled to quantum dots. *Nature*, 450(7168):402–406, 2007. {cited on page 54}

[AS72] Milton Abramowitz and Irene A Stegun. *Handbook of mathematical functions with formulas, graphs, and mathematical tables*, volume 55. Courier Dover Publications, 1972. {cited on page 25}

[AV93] Yakir Aharonov and Lev Vaidman. Measurement of the Schrödinger wave of a single particle. *Physics Letters A*, 178(1):38–42, 1993. {cited on page 67}

[AVEW02] E Altewischer, M P Van Exter, and J P Woerdman. Plasmon-assisted transmission of entangled photons. *Nature*, 418(6895):304–306, 2002. {cited on page 54}

[AWB+09] Markus Ansmann, H Wang, Radoslaw C Bialczak, Max Hofheinz, Erik Lucero, M Neeley, A D O'Connell, D Sank, M Weides, J Wenner, A N Cleland, and John M Martinis. Violation of Bell's inequality in Josephson phase qubits. *Nature*, 461(7263):504–506, 2009. {cited on page 10}

[BA57] David Bohm and Yakir Aharonov. Discussion of experimental proof for the paradox of Einstein, Rosen, and Podolsky. *Physical Review*, 108(4):1070, 1957. {cited on page 6}

[BB84] Charles H Bennett and Gilles Brassard. Quantum cryptography: Public key distribution and coin tossing. In *Proceedings of IEEE International Conference on Computers, Systems and Signal Processing*, volume 175. New York, 1984. {cited on page 17}

[BBC+93] Charles H Bennett, Gilles Brassard, Claude Crépeau, Richard Jozsa, Asher Peres, and William K Wootters. Teleporting an unknown quantum state via dual classical and Einstein-Podolsky-Rosen channels. *Physical Review Letters*, 70(13):1895, 1993. {cited on page 19}

[BBM92] Charles H Bennett, Gilles Brassard, and N David Mermin. Quantum cryptography without Bell's theorem. *Physical Review Letters*, 68(5):557, 1992. {cited on page 19}

[BDCZ98] Hans Jürgen Briegel, Wolfgang Dür, Juan Ignacio Cirac, and Peter Zoller. Quantum repeaters: The role of imperfect local operations in quantum communication. *Physical Review Letters*, 81(26):5932, 1998. {cited on page 1}

[BDE03] William L Barnes, Alain Dereux, and Thomas W Ebbesen. Surface plasmon subwavelength optics. *Nature*, 424(6950):824–830, 2003. {cited on page 54}

[BDSW96] Charles H Bennett, David P DiVincenzo, John A Smolin, and William K Wootters. Mixed-state entanglement and quantum error correction. *Physical Review A*, 54(5):3824, 1996. {cited on page 1}

[Bel64] John S Bell. On the Einstein-Podolsky-Rosen paradox. *Physics*, 1(3):195–200, 1964. {cited on page 7}

[BGTZ99] Jürgen Brendel, Nicolas Gisin, Wolfgang Tittel, and Hugo Zbinden. Pulsed energy-time entangled twin-photon source for quantum communication. *Physical Review Letters*, 82(12):2594, 1999. {cited on page 21}

[BHK+10] Thomas M Babinec, Birgit J M Hausmann, Mughees Khan, Yinan Zhang, Jeronimo R Maze, Philip R Hemmer, and Marko Lončar. A diamond nanowire single-photon source. *Nature Nanotechnology*, 5(3):195–199, 2010. {cited on page 11}

[BLC+11] Edouard Brainis, Karel Lambert, Klara Cielen, Adrien Licari, Philippe Emplit, and Zeger Hens. Towards parallel control of multiple single-photon emitters. In *European Quantum Electronics Conference*, page EA7_4. Optical Society of America, 2011. {cited on page 11}

[Blo06] Matthieu Bloch. *Algorithme de réconciliation et méthodes de distribution quantique de clés adaptées au domaine fréquentiel*. PhD thesis, Université de Franche-Comté, 2006. {cited on pages 25 and 28}

[BLPK05] Julio T Barreiro, Nathan K Langford, Nicholas A Peters, and Paul G Kwiat. Generation of hyperentangled photon pairs. *Physical Review Letters*, 95(26):260501, 2005. {cited on pages 21 and 60}

[BLS+13] Angelo Bassi, Kinjalk Lochan, Seema Satin, Tejinder P Singh, and Hendrik Ulbricht. Models of wave-function collapse, underlying theories, and experimental tests. *Reviews of Modern Physics*, 85(2):471, 2013. {cited on page 1}

[BMM92] Jürgen Brendel, E Mohler, and W Martienssen. Experimental test of Bell's inequality for energy and time. *Europhysics Letters*, 20(7):575, 1992. {cited on page 21}

[BMMP07] Matthieu Bloch, Steven W McLaughlin, Jean-Marc Merolla, and Frédéric Patois. Frequency-coded quantum key distribution. *Optics Letters*, 32(3):301–303, 2007. {cited on pages 2, 22, 50, 56, and 57}

[Boy03] Robert W Boyd. *Nonlinear optics*. Academic Press, 2003. {cited on page 22}

[BPM+97] Dik Bouwmeester, Jian-Wei Pan, Klaus Mattle, Manfred Eibl, Harald Weinfurter, and Anton Zeilinger. Experimental quantum teleportation. *Nature*, 390(6660):575–579, 1997. {cited on page 20}

[BPT00] H Bechmann-Pasquinucci and Wolfgang Tittel. Quantum cryptography using larger alphabets. *Physical Review A*, 61(6):062308, 2000. {cited on page 60}

[BSD+10] Wim Bogaerts, Shankar Kumar Selvaraja, Pieter Dumon, Joost Brouckaert, Katrien De Vos, Dries Van Thourhout, and Roel Baets. Silicon-on-insulator spectral filters fabricated with CMOS technology. *IEEE Journal of Selected Topics in Quantum Electronics*, 16(1):33–44, 2010. {cited on page 62}

[BZ03] Časlav Brukner and Anton Zeilinger. *Information and fundamental elements of the structure of quantum theory*. Springer, 2003. {cited on page 67}

[CCR02] A Bruce Carlson, P B Crilly, and J C Rutledge. Communication systems. Technical report, ISBN 0-07-112175-7, 2002. {cited on page 31}

[CFP10] José Capmany and Carlos R Fernández-Pousa. Quantum model for electro-optical phase modulation. *JOSA B*, 27(6):A119–A129, 2010. {cited on pages 21 and 25}

[CFP11] José Capmany and Carlos R Fernández-Pousa. Quantum modelling of electro-optic modulators. *Laser & Photonics Reviews*, 5(6):750–772, 2011. {cited on page 25}

[CFS02] Carlton M Caves, Christopher A Fuchs, and Rüdiger Schack. Quantum probabilities as Bayesian probabilities. *Physical Review A*, 65(2):022305, 2002. {cited on page 67}

[CGL+02] Daniel Collins, Nicolas Gisin, Noah Linden, Serge Massar, and Sandu Popescu. Bell inequalities for arbitrarily high-dimensional systems. *Physical Review Letters*, 88(4):040404, 2002. {cited on page 60}

[CH74] John F Clauser and Michael A Horne. Experimental consequences of objective local theories. *Physical Review D*, 10(2):526, 1974. {cited on pages 9, 51, and 65}

[CHSH69] John F Clauser, Michael A Horne, Abner Shimony, and Richard A Holt. Proposed experiment to test local hidden-variable theories. *Physical Review Letters*, 23(15):880, 1969. {cited on page 7}

[Cir80] Boris S Cirel'son. Quantum generalizations of Bell's inequality. *Letters in Mathematical Physics*, 4(2):93–100, 1980. {cited on page 9}

[CLR+14] Yong-Jing Cai, Ming Li, Xi-Feng Ren, Chang-Ling Zou, Xiao Xiong, Hua-Lin Lei, Bi-Heng Liu, Guo-Ping Guo, and Guang-Can Guo. High visibility on-chip quantum interference of single surface plasmons. *arXiv preprint arXiv:1402.0955*, 2014. {cited on page 54}

[CME10] Stéphane Clemmen, Serge Massar, and Philippe Emplit. *Optique quantique dans des structures guidantes en silicium: Caractérisation non linéaire, génération et manipulation de paires de photons*. PhD thesis, Université libre de Bruxelles, 2010. {cited on pages 61, 62, and 63}

[CPHB+09] Stéphane Clemmen, Kien Phan Huy, Wim Bogaerts, Roel G Baets, Philippe Emplit, and Serge Massar. Continuous wave photon pair generation in silicon-on-insulator waveguides and ring resonators. *Optics Express*, 17(19):16558–16570, 2009. {cited on page 61}

[CPPM08] Johann Cussey, Frédéric Patois, Nicolas Pelloquin, and Jean-Marc Merolla. High frequency spectral domain QKD architecture with dispersion management for WDM network. In *Optical Fiber Communication Conference*, page OWJ3. Optical Society of America, 2008. {cited on pages 2 and 22}

[CPS+12] Stéphane Clemmen, Antony Perret, Jassem Safioui, Wim Bogaerts, Roel Baets, Simon-Pierre Gorza, Philippe Emplit, and Serge Massar. Low-power inelastic light scattering at small detunings in silicon wire waveguides at telecom wavelengths. *JOSA B*, 29(8):1977–1982, 2012. {cited on page 64}

[CPV+08] Annie Cuyt, Vigdis Brevik Petersen, Brigitte Verdonk, Haakon Waadeland, and William B Jones. *Handbook of continued fractions for special functions*. Springer, 2008. {cited on page 23}

[CZKM97] Juan Ignacio Cirac, Peter Zoller, H Jeff Kimble, and Hideo Mabuchi. Quantum state transfer and entanglement distribution among distant nodes in a quantum network. *Physical Review Letters*, 78(16):3221, 1997. {cited on page 1}

[DGA14] S Dutta Gupta and G S Agarwal. Two-photon quantum interference in plasmonics: Theory and applications. *Optics Letters*, 39(2):390–393, 2014. {cited on page 54}

[Die82] Dennis G B J Dieks. Communication by EPR devices. *Physics Letters A*, 92(6):271–272, 1982. {cited on page 5}

[DLB+11] Adetunmise C Dada, Jonathan Leach, Gerald S Buller, Miles J Padgett, and Erika Andersson. Experimental high-dimensional two-photon entanglement and violations of generalized bell inequalities. *Nature Physics*, 7(9):677–680, 2011. {cited on page 60}

[DMG+01] Laurent Duraffourg, Jean-Marc Merolla, Jean-Pierre Goedgebuer, Yuri Mazurenko, and William T Rhodes. Compact transmission system using single-sideband modulation of light for quantum cryptography. *Optics Letters*, 26(18):1427–1429, 2001. {cited on page 2}

[DMSKC+12] Giuliana Di Martino, Yannick Sonnefraud, Stéphane Kéna-Cohen, Mark S Tame, Ş K Özdemir, M S Kim, and Stefan A Maier. Quantum statistics of surface plasmon polaritons in metallic stripe waveguides. *Nano Letters*, 12(5):2504–2508, 2012. {cited on page 54}

[DMST+14] Giuliana Di Martino, Yannick Sonnefraud, Mark S Tame, Stéphane Kéna-Cohen, F Dieleman, Ş K Özdemir, M S Kim, and Stefan A Maier. Observation of quantum interference in the plasmonic Hong-Ou-Mandel effect. *Physical Review Applied*, 1(3):034004, 2014. {cited on page 54}

[DRMS+04] Hugues De Riedmatten, Ivan Marcikic, Valerio Scarani, Wolfgang Tittel, Hugo Zbinden, and Nicolas Gisin. Tailoring photonic entanglement in high-dimensional hilbert spaces. *Physical Review A*, 69(5):050304, 2004. {cited on page 60}

[DRMT+04] Hugues De Riedmatten, Ivan Marcikic, Wolfgang Tittel, Hugo Zbinden, Daniel Collins, and Nicolas Gisin. Long distance quantum teleportation in a quantum relay configuration. *Physical Review Letters*, 92(4):047904, 2004. {cited on page 2}

[EFMP11] M D Eisaman, J Fan, A Migdall, and S V Polyakov. Invited review article: Single-photon sources and detectors. *Review of Scientific Instruments*, 82(7):071101, 2011. {cited on page 11}

[Eke91] Artur K Ekert. Quantum cryptography based on Bell's theorem. *Physical Review Letters*, 67(6):661, 1991. {cited on page 19}

[ELG+98] Thomas W Ebbesen, H J Lezec, H F Ghaemi, Tineke Thio, and P A Wolff. Extraordinary optical transmission through sub-wavelength hole arrays. *Nature*, 391(6668):667–669, 1998. {cited on page 54}

[EPR35] Albert Einstein, Boris Podolsky, and Nathan Rosen. Can quantum-mechanical description of physical reality be considered complete? *Physical Review*, 47(10):777, 1935. {cited on page 6}

[ERTP92] Artur K Ekert, John G Rarity, Paul R Tapster, and G Massimo Palma. Practical quantum cryptography based on two-photon interferometry. *Physical Review Letters*, 69(9):1293, 1992. {cited on page 19}

[FAO+07] Jérémie Fulconis, Olivier Alibart, Jeremy L O'Brien, William J Wadsworth, and John G Rarity. Nonclassical interference and entanglement generation using a photonic crystal fiber pair photon source. *Physical Review Letters*, 99(12):120501, 2007. {cited on page 62}

[FC72] Stuart J Freedman and John F Clauser. Experimental test of local hidden-variable theories. *Physical Review Letters*, 28(14):938, 1972. {cited on page 10}

[FHA+09] Alessandro Fedrizzi, Thomas Herbst, Markus Aspelmeyer, Marco Barbieri, Thomas Jennewein, and Anton Zeilinger. Anti-symmetrization reveals hidden entanglement. *New Journal of Physics*, 11(10):103052, 2009. {cited on page 21}

[FHGZ06] Sylvain Fasel, Matthäus Halder, Nicolas Gisin, and Hugo Zbinden. Quantum superposition and entanglement of mesoscopic plasmons. *New Journal of Physics*, 8(1):13, 2006. {cited on page 54}

[FLKA14] James S Fakonas, Hyunseok Lee, Yousif A Kelaita, and Harry A Atwater. Two-plasmon quantum interference. *Nature Photonics*, 8(4):317–320, 2014. {cited on page 54}

[FNM+07] Go Fujii, Naoto Namekata, Masayuki Motoya, Sunao Kurimura, and Shuichiro Inoue. Bright narrowband source of photon pairs at optical telecommunication wavelengths using a type-II periodically poled lithium niobate waveguide. *Optics Express*, 15(20):12769–12776, 2007. {cited on page 61}

[Fra89] James D Franson. Bell inequality for position and time. *Physical Review Letters*, 62(19):2205, 1989. {cited on pages 2, 14, and 21}

[FRM+05] Sylvain Fasel, Franck Robin, Esteban Moreno, Daniel Erni, Nicolas Gisin, and Hugo Zbinden. Energy-time entanglement preservation in plasmon-assisted light transmission. *Physical Review Letters*, 94(11):110501, 2005. {cited on page 54}

[FTK06] Shigenori Fujikawa, Rie Takaki, and Toyoki Kunitake. Fabrication of arrays of sub-20-nm silica walls via photolithography and solution-based molecular coating. *Langmuir*, 22(21):9057–9061, 2006. {cited on page 54}

[FUH+09] Alessandro Fedrizzi, Rupert Ursin, Thomas Herbst, Matteo Nespoli, Robert Prevedel, Thomas Scheidl, Felix Tiefenbacher, Thomas Jennewein, and Anton Zeilinger. High-fidelity transmission of entanglement over a high-loss free-space channel. *Nature Physics*, 5(6):389–392, 2009. {cited on page 19}

[GC08] John C Garrison and Raymond Y Chiao. *Quantum optics*. Oxford University Press, 2008. {cited on pages 11 and 75}

[Gis14] Nicolas Gisin. *Quantum chance: Nonlocality, teleportation and other quantum marvels*. Springer, 2014. {cited on pages 1 and 10}

[GLM06] Vittorio Giovannetti, Seth Lloyd, and Lorenzo Maccone. Quantum metrology. *Physical Review Letters*, 96(1):010401, 2006. {cited on page 1}

[GM87] Anupam Garg and N David Mermin. Detector inefficiencies in the Einstein-Podolsky-Rosen experiment. *Physical Review D*, 35(12):3831, 1987. {cited on page 10}

[GMR+13] Marissa Giustina, Alexandra Mech, Sven Ramelow, Bernhard Wittmann, Johannes Kofler, Jörn Beyer, Adriana Lita, Brice Calkins, Thomas Gerrits, Sae Woo Nam, Rupert Ursin, and Anton Zeilinger. Bell violation using entangled photons without the fair-sampling assumption. *Nature*, 497(7448):227–230, 2013. {cited on pages 10 and 65}

[GMS+03] Olivier L Guerreau, Jean-Marc Merolla, Alexandre Soujaeff, Frédéric Patois, J-P Goedgebuer, and François J Malassenet. Long-distance QKD transmission using single-sideband detection scheme with WDM synchronization. *IEEE Journal of Selected Topics in Quantum Electronics*, 9(6):1533–1540, 2003. {cited on page 2}

[GOC+01] G N Gol'Tsman, O Okunev, G Chulkova, A Lipatov, A Semenov, K Smirnov, B Voronov, A Dzardanov, C Williams, and Roman Sobolewski. Picosecond superconducting single-photon optical detector. *Applied Physics Letters*, 79(6):705–707, 2001. {cited on page 2}

[GRTZ02] Nicolas Gisin, Grégoire Ribordy, Wolfgang Tittel, and Hugo Zbinden. Quantum cryptography. *Reviews of Modern Physics*, 74(1):145, 2002. {cited on page 17}

[GT07] Nicolas Gisin and Rob Thew. Quantum communication. *Nature Photonics*, 1(3):165–171, 2007. {cited on page 1}

[GTMCM+11] A Gonzalez-Tudela, Diego Martin-Cano, Esteban Moreno, Luis Martin-Moreno, C Tejedor, and Francisco J Garcia-Vidal. Entanglement of two qubits mediated by one-dimensional plasmonic waveguides. *Physical Review Letters*, 106(2):020501, 2011. {cited on page 54}

[Har93] Lucien Hardy. Nonlocality for two particles without inequalities for almost all entangled states. *Physical Review Letters*, 71(11):1665, 1993. {cited on page 65}

[Har08] S E Harris. Nonlocal modulation of entangled photons. *Physical Review A*, 78(2):021807, 2008. {cited on page 21}

[HBG+07] Matthäus Halder, Alexios Beveratos, Nicolas Gisin, Valerio Scarani, Christoph Simon, and Hugo Zbinden. Entangling independent photons by time measurement. *Nature Physics*, 3(10):692–695, 2007. {cited on pages 20 and 21}

[HBT+08] Matthäus Halder, Alexios Beveratos, Robert T Thew, Corentin Jorel, Hugo Zbinden, and Nicolas Gisin. High coherence photon pair source for quantum communication. *New Journal of Physics*, 10(2):023027, 2008. {cited on pages 21 and 36}

[HHHH09] Ryszard Horodecki, Paweł Horodecki, Michał Horodecki, and Karol Horodecki. Quantum entanglement. *Reviews of Modern Physics*, 81(2):865, 2009. {cited on page 1}

[HKZ13] Reinier W Heeres, Leo P Kouwenhoven, and Valery Zwiller. Quantum interference in plasmonic circuits. *Nature Nanotechnology*, 8(10):719–722, 2013. {cited on page 54}

[HMR+05] E H Huntington, G N Milford, C Robilliard, T C Ralph, O Glöckl, Ulrik L Andersen, S Lorenz, and G Leuchs. Demonstration of the spatial separation of the entangled quantum sidebands of an optical field. *Physical Review A*, 71(4):041802, 2005. {cited on page 22}

[HOM87] C K Hong, Z Y Ou, and Leonard Mandel. Measurement of subpicosecond time intervals between two photons by interference. *Physical Review Letters*, 59(18):2044, 1987. {cited on pages 12 and 21}

[HR04] E H Huntington and T C Ralph. Components for optical qubits encoded in sideband modes. *Physical Review A*, 69(4):042318, 2004. {cited on page 22}

[HS10] Nicholas Harrigan and Robert W Spekkens. Einstein, incompleteness, and the epistemic view of quantum states. *Foundations of Physics*, 40(2):125–157, 2010. {cited on pages 67, 68, and 78}

[HSL+09] Alexander Huck, Stephan Smolka, Peter Lodahl, Anders S Sørensen, Alexandra Boltasseva, Jiri Janousek, and Ulrik L Andersen. Demonstration of quadrature-squeezed surface plasmons in a gold waveguide. *Physical Review Letters*, 102(24):246802, 2009. {cited on page 54}

[HTF+08] Ken-Ichi Harada, Hiroki Takesue, Hiroshi Fukuda, Tai Tsuchizawa, Toshifumi Watanabe, Koji Yamada, Yasuhiro Tokura, and Sei-Ichi Itabashi. Generation of high-purity entangled photon pairs using silicon wire waveguide. *Optics Express*, 16(25):20368–20373, 2008. {cited on page 61}

[Jac12] Zubin Jacob. Quantum plasmonics. *Mrs Bulletin*, 37(08):761–767, 2012. {cited on page 54}

[JKMW01] Daniel F V James, Paul G Kwiat, William J Munro, and Andrew G White. Measurement of qubits. *Physical Review A*, 64(5):052312, 2001. {cited on pages 17 and 65}

[Jot14] Igor Jottrand. Manipulation de photons enchevêtrés en fréquence avec des signaux de modulation variés. Master's thesis, Université libre de Bruxelles, 2014. {cited on page 58}

[JS11] Zubin Jacob and Vladimir Shalaev. Plasmonics goes quantum. *Science*, 334:463–464, 2011. {cited on page 54}

[JSW+00] Thomas Jennewein, Christoph Simon, Gregor Weihs, Harald Weinfurter, and Anton Zeilinger. Quantum cryptography with entangled photons. *Physical Review Letters*, 84(20):4729, 2000. {cited on page 19}

[KF09] Wakana Kubo and Shigenori Fujikawa. Embedding of a gold nanofin array in a polymer film to create transparent, flexible and anisotropic electrodes. *Journal of Materials Chemistry*, 19(15):2154–2158, 2009. {cited on page 54}

[KF10] Wakana Kubo and Shigenori Fujikawa. Au double nanopillars with nanogap for plasmonic sensor. *Nano Letters*, 11(1):8–15, 2010. {cited on page 54}

[KGB+09] Roman Kolesov, Bernhard Grotz, Gopalakrishnan Balasubramanian, Rainer J Stöhr, Aurélien A L Nicolet, Philip R Hemmer, Fedor Jelezko, and Jörg Wrachtrup. Wave–particle duality of single surface plasmon polaritons. *Nature Physics*, 5(7):470–474, 2009. {cited on page 54}

[Kim08] H Jeff Kimble. The quantum internet. *Nature*, 453(7198):1023–1030, 2008. {cited on page 1}

[KKK03] Heonoh Kim, Jeonghoon Ko, and Taesoo Kim. Two-particle interference experiment with frequency-entangled photon pairs. *JOSA B*, 20(4):760–763, 2003. {cited on page 21}

[KMW+95] Paul G Kwiat, Klaus Mattle, Harald Weinfurter, Anton Zeilinger, Alexander V Sergienko, and Yanhua Shih. New high-intensity source of polarization-entangled photon pairs. *Physical Review Letters*, 75(24):4337, 1995. {cited on pages 2, 11, and 61}

[KMZW00] Christian Kurtsiefer, Sonja Mayer, Patrick Zarda, and Harald Weinfurter. Stable solid-state source of single photons. *Physical Review Letters*, 85(2):290, 2000. {cited on page 11}

[KR97] Timothy E Keller and Morton H Rubin. Theory of two-photon entanglement for spontaneous parametric down-conversion driven by a narrow pump pulse. *Physical Review A*, 56(2):1534, 1997. {cited on page 2}

[KSC93] Paul G Kwiat, Aephraim M Steinberg, and Raymond Y Chiao. High-visibility interference in a Bell-inequality experiment for energy and time. *Physical Review A*, 47(4):R2472, 1993. {cited on page 21}

[Lan96] Rolf Landauer. The physical nature of information. *Physics Letters A*, 217(4):188–193, 1996. {cited on page 4}

[LCK+10] François Leo, Stéphane Coen, Pascal Kockaert, Simon-Pierre Gorza, Philippe Emplit, and Marc Haelterman. Temporal cavity solitons in one-dimensional Kerr media as bits in an all-optical buffer. *Nature Photonics*, 4(7):471–476, 2010. {cited on page 71}

[LJBR12] Peter G Lewis, David Jennings, Jonathan Barrett, and Terry Rudolph. Distinct quantum states can be compatible with a single state of reality. *Physical Review Letters*, 109(15):150404, 2012. {cited on pages 68 and 78}

[LVSK05] Xiaoying Li, Paul L Voss, Jay E Sharping, and Prem Kumar. Optical-fiber source of polarization-entangled photons in the 1550 nm telecom band. *Physical Review Letters*, 94(5):053601, 2005. {cited on page 61}

[LYM+09] Xiaoying Li, Lei Yang, Xiaoxin Ma, Liang Cui, Zhe Yu Ou, and Daoyin Yu. All-fiber source of frequency-entangled photon pairs. *Physical Review A*, 79(3):033817, 2009. {cited on page 21}

[MDRT+02] Ivan Marcikic, Hugues De Riedmatten, W Tittel, V Scarani, H Zbinden, and N Gisin. Time-bin entangled qubits for quantum communication created by femtosecond pulses. *Physical Review A*, 66(6):062308, 2002. {cited on page 21}

[MDRT+04] Ivan Marcikic, Hugues De Riedmatten, Wolfgang Tittel, Hugo Zbinden, Matthieu Legré, and Nicolas Gisin. Distribution of time-bin entangled qubits over 50 km of optical fiber. *Physical Review Letters*, 93(18):180502, 2004. {cited on pages 2 and 21}

[MFL07] Xiongfeng Ma, Chi-Hang Fred Fung, and Hoi-Kwong Lo. Quantum key distribution with entangled photon sources. *Physical Review A*, 76(1):012307, 2007. {cited on page 19}

[MGVE+04] Esteban Moreno, F J Garcia-Vidal, Daniel Erni, J Ignacio Cirac, and L Martín-Moreno. Theory of plasmon-assisted transmission of entangled photons. *Physical Review Letters*, 92(23):236801, 2004. {cited on page 54}

[MIH+10] Anthony Martin, Amandine Issautier, Harrald Herrmann, Wolfgang Sohler, Daniel Barry Ostrowsky, Olivier Alibart, and Sébastien Tanzilli. A polarization entangled photon-pair source based on a type-II PPLN waveguide emitting at a telecom wavelength. *New Journal of Physics*, 12(10):103005, 2010. {cited on pages 11, 44, and 61}

[MK04] Dzmitry N Matsukevich and A Kuzmich. Quantum state transfer between matter and light. *Science*, 306(5696):663–666, 2004. {cited on page 1}

[MKB+00] P Michler, A Kiraz, C Becher, W V Schoenfeld, P M Petroff, Lidong Zhang, E Hu, and A Imamoglu. A quantum dot single-photon turnstile device. *Science*, 290(5500):2282–2285, 2000. {cited on page 11}

[MLJF+12] Nobuyuki Matsuda, Hanna Le Jeannic, Hiroshi Fukuda, Tai Tsuchizawa, William John Munro, Kaoru Shimizu, Koji Yamada, Yasuhiro Tokura, and Hiroki Takesue. A monolithically integrated polarization entangled photon pair source on a silicon chip. *Scientific Reports*, 2, 2012. {cited on page 61}

[MMG+99a] Jean-Marc Merolla, Yuri Mazurenko, Jean-Pierre Goedgebuer, Laurent Duraffourg, Henri Porte, and William T Rhodes. Quantum cryptographic device using single-photon phase modulation. *Physical Review A*, 60(3):1899, 1999. {cited on pages 2 and 22}

[MMG+99b] Jean-Marc Merolla, Yuri Mazurenko, Jean-Pierre Goedgebuer, Henri Porte, and William T Rhodes. Phase-modulation transmission system for quantum cryptography. *Optics Letters*, 24(2):104–106, 1999. {cited on pages 2 and 22}

[MMGR99] Jean-Marc Merolla, Yuri Mazurenko, Jean-Pierre Goedgebuer, and William T Rhodes. Single-photon interference in sidebands of phase-modulated light for quantum cryptography. *Physical Review Letters*, 82(8):1656, 1999. {cited on pages 2 and 22}

[MMGVL+01] L Martin-Moreno, F J Garcia-Vidal, H J Lezec, K M Pellerin, T Thio, J B Pendry, and T W Ebbesen. Theory of extraordinary optical transmission through subwavelength hole arrays. *Physical Review Letters*, 86(6):1114, 2001. {cited on page 54}

[MSM+02] Jean-Marc Merolla, Alexandre Soujaeff, Maxime Marc, Fréderic Patois, William T Rhodes, and J-P Goedgebuer. Integrated quantum key distribution system using single sideband detection. In *Quantum Electronics and Laser Science Conference, 2002. QELS'02. Technical Digest*, page 29. IEEE, 2002. {cited on page 2}

[MVWZ01] Alois Mair, Alipasha Vaziri, Gregor Weihs, and Anton Zeilinger. Entanglement of the orbital angular momentum states of photons. *Nature*, 412(6844):313–316, 2001. {cited on page 2}

[MW95] Leonard Mandel and Emil Wolf. *Optical coherence and quantum optics*. Cambridge University Press, 1995. {cited on pages 1 and 11}

[NC10] Michael A Nielsen and Isaac L Chuang. *Quantum computation and quantum information*. Cambridge University Press, 2010. {cited on pages 1 and 11}

[NME08] Anh Tuan Nguyen, Serge Massar, and Philippe Emplit. *Utilisation de l'optique fibrée pour la manipulation et la génération d'états quantiques: Pile ou face quantique et paires de photons*. PhD thesis, Université libre de Bruxelles, 2008. {cited on page 36}

[NMS+12] Daniel Nigg, Thomas Monz, Philipp Schindler, Esteban A Martinez, Michael Chwalla, Markus Hennrich, Rainer Blatt, Matthew F Pusey, Terry Rudolph, and Jonathan Barrett. Can different quantum state vectors correspond to the same physical state? an experimental test. *arXiv preprint arXiv:1211.0942*, 2012. {cited on pages 69 and 79}

[NPW+00] D S Naik, C G Peterson, A G White, A J Berglund, and P G Kwiat. Entangled state quantum cryptography: Eavesdropping on the Ekert protocol. *Physical Review Letters*, 84(20):4733, 2000. {cited on page 19}

[OCN+10] Laurent Olislager, Johann Cussey, Anh Tuan Nguyen, Philippe Emplit, Serge Massar, Jean-Marc Merolla, and Kien Phan Huy. Frequency-bin entangled photons. *Physical Review A*, 82(1):013804, 2010. {cited on pages 2, 28, 34, 37, 38, 39, 40, 42, 45, 46, 50, 52, and 53}

[OM88] Z Y Ou and L Mandel. Observation of spatial quantum beating with separated photodetectors. *Physical Review Letters*, 61(1):54, 1988. {cited on page 21}

[OMV+05] S S R Oemrawsingh, X Ma, D Voigt, A Aiello, E R Eliel, G W 't Hooft, and J P Woerdman. Experimental demonstration of fractional orbital angular momentum entanglement of two photons. *Physical Review Letters*, 95(24):240501, 2005. {cited on page 60}

[OMW+12] Laurent Olislager, Ismaël Mbodji, Erik Woodhead, Johann Cussey, Luca Furfaro, Philippe Emplit, Serge Massar, Kien Phan Huy, and Jean-Marc Merolla. Implementing two-photon interference in the frequency domain with electro-optic phase modulators. *New Journal of Physics*, 14(4):043015, 2012. {cited on pages 2, 24, 28, 37, 38, 40, 42, 43, 45, 47, 51, and 52}

[OSC+13] Laurent Olislager, Jassem Safioui, Stéphane Clemmen, Kien Phan Huy, Wim Bogaerts, Roel Baets, Philippe Emplit, and Serge Massar. Silicon-on-insulator

integrated source of polarization-entangled photons. *Optics Letters*, 38(11):1960–1962, 2013. {cited on pages 40, 61, 62, 64, and 66}

[OWPH+14] Laurent Olislager, Erik Woodhead, Kien Phan Huy, Jean-Marc Merolla, Philippe Emplit, and Serge Massar. Creating and manipulating entangled optical qubits in the frequency domain. *Physical Review A*, 89(5):052323, 2014. {cited on pages 2, 28, 33, 34, 38, 39, 40, 42, 44, 45, 48, 49, and 53}

[PAM+10] Stefano Pironio, Antonio Acín, Serge Massar, Antoine Boyer de La Giroday, Dzimitry N Matsukevich, Peter Maunz, Steven Olmschenk, David Hayes, Le Luo, T Andrew Manning, and Christopher Monroe. Random numbers certified by Bell's theorem. *Nature*, 464(7291):1021–1024, 2010. {cited on page 19}

[PBR12] Matthew F Pusey, Jonathan Barrett, and Terry Rudolph. On the reality of the quantum state. *Nature Physics*, 8(6):475–478, 2012. {cited on pages 67, 68, and 78}

[PHNB+07] Kien Phan Huy, Anh Tuan Nguyen, Edouard Brainis, Marc Haelterman, Philippe Emplit, Costantino Corbari, Albert Canagasabey, Peter G Kazansky, Olivier Deparis, Andrei A Fotiadi, Patrice Mégret, and Serge Massar. Photon pair source based on parametric fluorescence in periodically poled twin-hole silica fiber. *Optics Express*, 15(8):4419–4426, 2007. {cited on page 36}

[POD+13] Manas Kumar Patra, Laurent Olislager, Francois Duport, Jassem Safioui, Stefano Pironio, and Serge Massar. Experimental refutation of a class of ψ-epistemic models. *Physical Review A*, 88(3):032112, 2013. {cited on pages 40, 67, 68, 69, 71, 73, 74, 76, 77, and 80}

[PPM13] Manas Kumar Patra, Stefano Pironio, and Serge Massar. No-go theorems for ψ-epistemic models based on a continuity assumption. *Physical Review Letters*, 111(9):090402, 2013. {cited on pages 67, 68, 69, 70, and 78}

[PR04] Matteo Paris and Jaroslav Rehacek. *Quantum state estimation*, volume 649. Springer, 2004. {cited on page 67}

[PSBZ01] Jian-Wei Pan, Christoph Simon, Časlav Brukner, and Anton Zeilinger. Entanglement purification for quantum communication. *Nature*, 410(6832):1067–1070, 2001. {cited on page 1}

[RBG+00] Grégoire Ribordy, Jürgen Brendel, Jean-Daniel Gautier, Nicolas Gisin, and Hugo Zbinden. Long-distance entanglement-based quantum key distribution. *Physical Review A*, 63(1):012309, 2000. {cited on page 2}

[RDB+14] Martin Ringbauer, Benjamin Duffus, Cyril Branciard, Eric Cavalcanti, Andrew White, and Alessandro Fedrizzi. Measurements on the reality of the wavefunction. In *Frontiers in Optics*, pages FW5C–1. Optical Society of America, 2014. {cited on page 69}

[RGG+98] Grégoire Ribordy, Jean-Daniel Gautier, Nicolas Gisin, Olivier Guinnard, and Hugo Zbinden. Automated 'plug & play' quantum key distribution. *Electronics Letters*, 34(22):2116–2117, 1998. {cited on page 13}

[RGH+06] Xi-Feng Ren, Guo-Ping Guo, Yun-Feng Huang, Chuan-Feng Li, and Guang-Can Guo. Plasmon-assisted transmission of high-dimensional orbital angular-momentum entangled state. *Europhysics Letters*, 76(5):753, 2006. {cited on page 54}

[RGZG98] Grégoire Ribordy, Jean-Daniel Gautier, Hugo Zbinden, and Nicolas Gisin. Performance of InGaAs/InP avalanche photodiodes as gated-mode photon counters. *Applied Optics*, 37(12):2272–2277, 1998. {cited on page 2}

[RKM+01] Mary A Rowe, David Kielpinski, Volker Meyer, Charles A Sackett, Wayne M Itano, Christopher Monroe, and David J Wineland. Experimental violation of a

Bell's inequality with efficient detection. *Nature*, 409(6822):791–794, 2001. {cited on page 10}

[RRF+09] S Ramelow, L Ratschbacher, A Fedrizzi, N K Langford, and A Zeilinger. Discrete tunable color entanglement. *Physical Review Letters*, 103(25):253601, 2009. {cited on page 21}

[RT90a] John G Rarity and Paul R Tapster. Experimental violation of Bell's inequality based on phase and momentum. *Physical Review Letters*, 64(21):2495, 1990. {cited on page 2}

[RT90b] John G Rarity and Paul R Tapster. Two-color photons and nonlocality in fourth-order interference. *Physical Review A*, 41(9):5139, 1990. {cited on page 21}

[SBG+05] Damien Stucki, Nicolas Brunner, Nicolas Gisin, Valerio Scarani, and Hugo Zbinden. Fast and simple one-way quantum key distribution. *Applied Physics Letters*, 87(19):194108, 2005. {cited on page 19}

[Scu97] Marlan O Scully. *Quantum optics*. Cambridge University Press, 1997. {cited on page 75}

[SKD+05] H F Schouten, N Kuzmin, G Dubois, T D Visser, G Gbur, P F A Alkemade, H Blok, G W 't Hooft, D Lenstra, and E R Eliel. Plasmon-assisted two-slit transmission: Young's experiment revisited. *Physical Review Letters*, 94(5):053901, 2005. {cited on page 54}

[SLF+06] Jay E Sharping, Kim F Lee, Mark A Foster, Amy C Turner, Bradley S Schmidt, Michal Lipson, Alexander L Gaeta, and Prem Kumar. Generation of correlated photons in nanoscale silicon waveguides. *Optics Express*, 14(25):12388–12393, 2006. {cited on page 61}

[SP00] Peter W Shor and John Preskill. Simple proof of security of the BB84 quantum key distribution protocol. *Physical Review Letters*, 85(2):441, 2000. {cited on page 19}

[Spe07] Robert W Spekkens. Evidence for the epistemic view of quantum states: A toy theory. *Physical Review A*, 75(3):032110, 2007. {cited on pages 67 and 78}

[SS94] Y H Shih and A V Sergienko. Observation of quantum beating in a simple beam-splitting experiment: Two-particle entanglement in spin and space-time. *Physical Review A*, 50(3):2564, 1994. {cited on pages 21 and 60}

[SST11] Artur Scherer, Barry C Sanders, and Wolfgang Tittel. Long-distance practical quantum key distribution by entanglement swapping. *Optics Express*, 19(4):3004–3018, 2011. {cited on page 19}

[Ste14] Michael Steel. Quantum plasmonics: Two-plasmon interference. *Nature Photonics*, 8(4):273–275, 2014. {cited on page 54}

[SUF+09] Thomas Scheidl, Rupert Ursin, Alessandro Fedrizzi, Sven Ramelow, Xiao-Song Ma, Thomas Herbst, Robert Prevedel, Lothar Ratschbacher, Johannes Kofler, Thomas Jennewein, and Anton Zeilinger. Feasibility of 300 km quantum key distribution with entangled states. *New Journal of Physics*, 11(8):085002, 2009. {cited on page 19}

[SYH09] S Sensarn, G Y Yin, and S E Harris. Observation of nonlocal modulation with entangled photons. *Physical Review Letters*, 103(16):163601, 2009. {cited on page 21}

[SZGS02] André Stefanov, Hugo Zbinden, Nicolas Gisin, and Antoine Suarez. Quantum correlations with spacelike separated beam splitters in motion: Experimental test of multisimultaneity. *Physical Review Letters*, 88(12):120404, 2002. {cited on page 10}

[SZGS03] André Stefanov, Hugo Zbinden, Nicolas Gisin, and Antoine Suarez. Quantum entanglement with acousto-optic modulators: Two-photon beats and Bell experiments with moving beam splitters. *Physical Review A*, 67(4):042115, 2003. {cited on pages 10 and 22}

[Tak12] Hiroki Takesue. Entangled photon pair generation using silicon wire waveguides. *IEEE Journal of Selected Topics in Quantum Electronics*, 18(6):1722–1732, 2012. {cited on page 61}

[TAZG04] Robert Thomas Thew, Antonio Acin, Hugo Zbinden, and Nicolas Gisin. Bell-type test of energy-time entangled qutrits. *Physical Review Letters*, 93(1):010503, 2004. {cited on page 60}

[TBG+98] Wolfgang Tittel, Jürgen Brendel, Bernard Gisin, Thomas Herzog, Hugo Zbinden, and Nicolas Gisin. Experimental demonstration of quantum correlations over more than 10 km. *Physical Review A*, 57(5):3229, 1998. {cited on page 21}

[TBGZ99] Wolfgang Tittel, Jürgen Brendel, Nicolas Gisin, and Hugo Zbinden. Long-distance Bell-type tests using energy-time entangled photons. *Physical Review A*, 59(6):4150, 1999. {cited on page 21}

[TBZG98] Wolfgang Tittel, Jürgen Brendel, Hugo Zbinden, and Nicolas Gisin. Violation of Bell inequalities by photons more than 10 km apart. *Physical Review Letters*, 81(17):3563, 1998. {cited on pages 2 and 21}

[TBZG00] Wolfgang Tittel, Jürgen Brendel, Hugo Zbinden, and Nicolas Gisin. Quantum cryptography using entangled photons in energy-time Bell states. *Physical Review Letters*, 84(20):4737, 2000. {cited on pages 19 and 21}

[TCB+03] Dirk Taillaert, Harold Chong, Peter I Borel, Lars H Frandsen, Richard M De La Rue, and Roel Baets. A compact two-dimensional grating coupler used as a polarization splitter. *Photonics Technology Letters*, 15(9):1249–1251, 2003. {cited on pages 62 and 63}

[TDRZ+01] Sébastien Tanzilli, Hugues De Riedmatten, Hugo Zbinden, Paolo Baldi, M De Micheli, DB Ostrowsky, Nicolas Gisin, et al. Highly efficient photon-pair source using periodically poled lithium niobate waveguide. *Electronics Letters*, 37(1):26–28, 2001. {cited on page 36}

[TFT+08] Hiroki Takesue, Hiroshi Fukuda, Tai Tsuchizawa, Toshifumi Watanabe, Koji Yamada, Yasuhiro Tokura, and Sei-ichi Itabashi. Generation of polarization entangled photon pairs using silicon wire waveguide. *Optics Express*, 16(8):5721–5727, 2008. {cited on page 61}

[TI04] Hiroki Takesue and Kyo Inoue. Generation of polarization-entangled photon pairs and violation of Bell's inequality using spontaneous four-wave mixing in a fiber loop. *Physical Review A*, 70(3):031802, 2004. {cited on page 61}

[TMÖ+13] M S Tame, K R McEnery, Ş K Özdemir, J Lee, S A Maier, and M S Kim. Quantum plasmonics. *Nature Physics*, 9(6):329–340, 2013. {cited on page 54}

[TNZ+07] Hiroki Takesue, Sae Woo Nam, Qiang Zhang, Robert H Hadfield, Toshimori Honjo, Kiyoshi Tamaki, and Yoshihisa Yamamoto. Quantum key distribution over a 40-dB channel loss using superconducting single-photon detectors. *Nature Photonics*, 1(6):343–348, 2007. {cited on page 19}

[TRO94] Paul R Tapster, John G Rarity, and P C M Owens. Violation of Bell's inequality over 4 km of optical fiber. *Physical Review Letters*, 73(14):1923, 1994. {cited on page 21}

[TRT93] Paul D Townsend, John G Rarity, and Paul R Tapster. Single photon interference in 10 km long optical fibre interferometer. *Electronics Letters*, 29(7):634–635, 1993. {cited on page 21}

[TTDR+02] S Tanzilli, W Tittel, H De Riedmatten, H Zbinden, P Baldi, M DeMicheli, Da B Ostrowsky, and N Gisin. PPLN waveguide for quantum communication. *The European Physical Journal D-Atomic, Molecular, Optical and Plasma Physics*, 18(2):155–160, 2002. {cited on page 36}

[TTF+07] Hiroki Takesue, Yasuhiro Tokura, Hiroshi Fukuda, Tai Tsuchizawa, Toshifumi Watanabe, Koji Yamada, and Sei-ichi Itabashi. Entanglement generation using silicon wire waveguide. *Applied Physics Letters*, 91(20):201108, 2007. {cited on page 61}

[TTH+05] Sébastien Tanzilli, Wolfgang Tittel, Matthaeus Halder, Olivier Alibart, Pascal Baldi, Nicolas Gisin, and Hugo Zbinden. A photonic quantum information interface. *Nature*, 437(7055):116–120, 2005. {cited on page 1}

[TTT+02] Robert Thomas Thew, Sébastien Tanzilli, Wolfgang Tittel, Hugo Zbinden, and Nicolas Gisin. Experimental investigation of the robustness of partially entangled qubits over 11 km. *Physical Review A*, 66(6):062304, 2002. {cited on page 21}

[UKC+13] Simona Ungureanu, Branko Kolaric, Jianing Chen, Rainer Hillenbrand, and Renaud AL Vallée. Far-field disentanglement of modes in hybrid plasmonic-photonic crystals by fluorescence nano-reporters. *Nanophotonics*, 2(3):173–185, 2013. {cited on page 54}

[vELDW07] Martin P van Exter, P S K Lee, S Doesburg, and J P Woerdman. Mode counting in high-dimensional orbital angular momentum entanglement. *Optics Express*, 15(10):6431–6438, 2007. {cited on page 60}

[VWZ02] Alipasha Vaziri, Gregor Weihs, and Anton Zeilinger. Experimental two-photon, three-dimensional entanglement for quantum communication. *Physical Review Letters*, 89(24):240401, 2002. {cited on page 60}

[WJS+98] Gregor Weihs, Thomas Jennewein, Christoph Simon, Harald Weinfurter, and Anton Zeilinger. Violation of Bell's inequality under strict Einstein locality conditions. *Physical Review Letters*, 81(23):5039, 1998. {cited on page 10}

[Woo10] Erik Woodhead. Frequency entangled photons and Bell inequality violation. Master's thesis, Université libre de Bruxelles, 2010. {cited on pages 24, 34, 51, and 53}

[Woo13] Erik Woodhead. Quantum cloning bound and application to quantum key distribution. *Physical Review A*, 88(1):012331, 2013. {cited on page 57}

[WZ82] William K Wootters and Wojciech H Zurek. A single quantum cannot be cloned. *Nature*, 299(5886):802–803, 1982. {cited on page 5}

[WZY02] Edo Waks, Assaf Zeevi, and Yoshihisa Yamamoto. Security of quantum key distribution with entangled photons against individual attacks. *Physical Review A*, 65(5):052310, 2002. {cited on page 19}

[YKS+02] Zhiliang Yuan, Beata E Kardynal, R Mark Stevenson, Andrew J Shields, Charlene J Lobo, Ken Cooper, Neil S Beattie, David A Ritchie, and Michael Pepper. Electrically driven single-photon source. *Science*, 295(5552):102–105, 2002. {cited on page 11}

[YY84] Amnon Yariv and Pochi Yeh. *Optical waves in crystals*, volume 10. Wiley, New York, 1984. {cited on page 25}

[Zei99] Anton Zeilinger. Experiment and the foundations of quantum physics. *Reviews of Modern Physics*, 71(2):S288, 1999. {cited on page 1}

[ZZHE93] M Zukowski, A Zeilinger, M A Horne, and A K Ekert. "Event-ready-detectors" Bell experiment via entanglement swapping. *Physical Review Letters*, 71(26):4287–4290, 1993. {cited on page 20}